Fractography and Crack Propagation in Functional Crystals

by

Anthony MOULINS

THESIS PRESENTED TO ÉCOLE DE TECHNOLOGIE SUPÉRIEURE
IN PARTIAL FULFILLMENT FOR THE DEGREE OF
DOCTOR OF PHILOSOPHY
Ph.D.

MONTRÉAL, AUGUST 16TH, 2021

ÉCOLE DE TECHNOLOGIE SUPÉRIEURE
UNIVERSITÉ DU QUÉBEC

BOARD OF EXAMINERS

THIS THESIS BY PUBLICATIONS HAS BEEN EVALUATED

BY THE FOLLOWING BOARD OF EXAMINERS

Professor Ricardo J. Zednik, Thesis Supervisor
Department of Mechanical Engineering, École de technologie supérieure

Professor Roberto Dugnani, Thesis Co-Supervisor
Department of Mechanical Engineering
College of Science and Engineering, University of Houston – Clear Lake

Professor Philippe Bocher, Board of Examiners
Department of Mechanical Engineering, École de technologie supérieure

Professor Frédéric Nabki, Chair, Board of Examiners
Department of Electrical Engineering, École de technologie supérieure

Dr. Luke Boyer, Manager
Carpenter Technology

THIS THESIS WAS PRESENTED AND DEFENDED

IN THE PRESENCE OF A BOARD OF EXAMINERS AND THE PUBLIC

ON AUGUST 4TH, 2021

AT ÉCOLE DE TECHNOLOGIE SUPÉRIEURE

« *Failure is success in progress* »

– A. Einstein –

ACKNOWLEDGMENTS

I would like to thank my supervisors who believed in me and particularly Prof Zednik who gave me the chance to live this great experience gaining scientific maturity, autonomy and pushing me beyond expectations. Ich werde immer dankbar sein, dass das Leben Sie auf meinen Weg gebracht hat und dass Sie mein Potenzial erkennen konnten. Vielen Dank für Ihren wertvollen Rat in den letzten 6 Jahren, Ihre Geduld und Ihr Vertrauen haben mich wachsen lassen. My deepest gratitude goes to Prof. Dugnani who despite the distance to Shanghai, has always supported me and encouraged me with kindness. Sei stata una così grande ispirazione in questo progetto. Both of you have shared your time, expertise, and advice with constructive criticism. I thank my friend and colleague Lingyue for his exceptional kindness, who welcomed me at the Joint Institute and who taught me rudimentary mandarin speaking.

I also wish to acknowledge the PULÉTS lab members as well as Prof. Bélanger, Prof. Demarquette, and Prof. Calas-Étienne for their kindness towards me and whose academic and professional careers are so very inspiring. Also thank you to the very talented students that I had the chance to co-supervise with Prof. Zednik such as Guillaume Grosse, Alexandre Esteves, François Andrusyszyn, and Robert Duma. Thank you to all the students and postdoctoral researchers that I had the chance to collaborate with and the exceptional technicians at school who helped me in labs particularly Olivier, Serge, Nabil, and Radu. You all gave me the chance to gain real scientific experiences and good scientific results.

I would like to thank the Natural Sciences and Engineering Research Council of Canada, MITACS Globalink, and the École de Technologie Supérieure - Fonds pour la collaboration international de recherche for the funding provided. It made my Ph. D. possible giving to the project an international dimension and I will be forever grateful for this.

Thank you to the jury for sharing your expertise and giving me your precious time to evaluate my work.

I would not have been able to succeed without the love of my family here all these years and to the other side of the Pacific Ocean. A huge thank you to my devoted friends. You followed all my adventures and always stood strong and faithful by my side. Finally, to my other half, your love, kindness, our laughs, cries, and peaceful nature moments were my biggest strength during this Ph.D. You always pushed me to be the better version of myself and I thank you for this.

Fractographie et propagation de fissure dans les cristaux fonctionnels

Anthony MOULINS

RÉSUMÉ

La rupture dans les matériaux de structure est assez bien connue et documentés avec des standards bien établis. Malheureusement, celle des cristaux fonctionnels qui se retrouvent dans tous nos appareils intelligents, fait partie de notre quotidien et reste encore mal comprise et peu voire pas étudiée. Une rupture conventionnelle se produit de manière catastrophique. La propagation des fissures est brutale et peut être perturbée par des instabilités de nature physique, par l'orientation du cristal et/ou des contraintes mécaniques. L'intensité locale des champs de contraintes (SIF) est un élément prééminent dans l'étude des cristaux fonctionnels fragiles. Le SIF change dès lors que les caractéristiques topographiques de la surface de rupture sont modifiées au cours de la propagation par exemple lors de la formation de facettes cristallographiques. Au moment de la fissuration, ces singularités, restent inscrites sur les surfaces crées et sont souvent les seuls indices encore visibles et exploitable pour connaitre l'histoire mécanique du cristal. Par conséquent, l'étude du SIF en corrélation avec les traces fractographiques est un indicateur puissant pour comprendre la mécanique de la rupture dans les processus de la propagation rapide des fissures. En revanche aucun standards n'existe pour l'évaluation de la défaillance mécanique des cristaux fonctionnels où leur étude se complexifie au regard de leur comportement fortement anisotrope. Il n'existe à ce jour que très peu d'études pour comprendre et évaluer le niveau de contraintes dans ces matériaux au moment de la rupture avec une résolution suffisante et sans homogénéiser les propriétés élastiques de ces matériaux. Le projet se concentre sur la compréhension analytique et expérimentale de la propagation des fissures dans les monocristaux de silicium (Si) et d'arséniure de gallium (GaAs) en tant que matériaux modèles. Le but est l'acquisition de connaissances fondamentales en fractographie pour comprendre la morphologie des surfaces de rupture en lien avec les contraintes mécaniques appliquées. Le projet intègre le développement de méthodes et de procédures innovantes d'estimation des propriétés mécaniques de GaAs et de Si prenant en compte l'anisotropie intrinsèque des monocristaux. Ce travail inclut l'analyse avancée de la surface de rupture des monocristaux, que l'on trouve généralement dans les systèmes micro-électromécaniques (MEMS) et la généralisation des méthodes d'analyse développées pour les systèmes isotropes vers les systèmes anisotropes. Les fissures générant des surfaces sont analysées pour identifier et caractériser les singularités topographiques des échantillons surchargés expérimentalement. Les travaux préliminaires de préparation des échantillons, ainsi que les essais mécaniques à différentes longueurs d'échelles font parties de cette étude. Les aspects de la propagation instable de la fissure sont étudiés avec une modélisation analytique qui comprend l'instabilité dynamique, l'anisotropie, l'étude des

contraintes au voisinage d'une fissure et l'évaluation des propriétés physiques directement reliées à la libération d'énergie de déformation dans le cristal. La modélisation analytique est validée par les résultats expérimentaux pour prédire le comportement des cristaux fonctionnels.

Mots-clés : propagation des fissures, fractographie, monocristaux, anisotropie, résistance mécanique, caractéristiques de rupture, semi-conducteurs, modélisation analytique

Fractography and crack propagation in functional crystals

Anthony MOULINS

ABSTRACT

Failure in structural materials is generally well-known and documented with established standards. Unfortunately, for the case of functional crystals that are found in all our smart devices, failure remains poorly understood and studied although being a very common part of our daily lives. Conventional rupture often occurs catastrophically. The propagation of cracks is sudden and can often be disturbed by instabilities of physical nature, by the orientation of the crystal and/or mechanical stresses. The local stress intensity factor (SIF) is a preeminent element in the study of brittle functional crystals. The SIF changes when the topographic characteristics of the fracture surface are modified during propagation, for example when crystallographic facets are formed. At the time of failure, these singularities remain inscribed on the surfaces newly created and are often the only clues still visible and available to investigate the mechanical history of the crystal. Therefore, the study of SIF in correlation with fractographic traces is the most powerful indicator for understanding the fracture mechanics in the processes of rapid crack propagation. On the other hand, no standards exist for the evaluation of the mechanical failure of functional crystals where their study becomes more complex regarding their strongly anisotropic mechanical behavior. To date, there are very few studies to understand and assess the level of stresses in these materials when a failure occurs with a sufficient resolution, without homogenizing the anisotropic elastic properties. The project focuses on the analytical and experimental understanding of crack propagation in silicon (Si) and gallium arsenide (GaAs) single crystals as model semiconductor materials. The goal is the acquisition of fundamental knowledge in fractography to understand the morphology of fracture surfaces and relate them to the applied mechanical stresses. The project integrates the development of innovative methods and procedures for estimating the mechanical properties of GaAs and Si considering the intrinsic anisotropy of single crystals. This work includes the advanced analysis of the fracture surface of single crystals, which is generally found in micro-electromechanical systems (MEMS) whose properties and behaviors are often subject of debate as no established standard reference exists. The crack surfaces are analyzed to identify and characterize the topographic singularities of the experimentally overloaded samples. Preliminary sample preparation work, as well as mechanical testing at different scale lengths, is part of this study. Along with the experimental work, aspects of unstable crack propagation are studied with analytical modeling that includes dynamic instability, anisotropy, the study of stresses in the vicinity of a crack, and the evaluation of physical properties directly related to the release of strain energy in the crystal. The analytical modeling is validated by the experimental results to predict the behavior of functional crystals.

Keywords : crack propagation, fractography, single crystals, anisotropy, mechanical strength, fracture features, semiconductors, analytical modeling

TABLE OF CONTENTS

LIST OF TABLES

Page

LIST OF FIGURES

Page

LIST OF THE MAIN SYMBOLS AND UNITS

σ_f	Fracture strength, MPa (Mega Pascal)
A_m	Isotropic mirror constant, MPa·m$^{0.5}$ (Mega Pascal square root of meter)
R_m	Isotropic mirror radius, μm (Micrometer)
ρ	Density, kg·m^{-3} (Kilogram per cubic meter)
v	Crack-tip speed, m·s^{-1} (Meter per second)
σ_{ij}	Stress tensor components
u_i	Components of particle displacement vector
S_{ij}	Components of compliance tensor, Pa^{-1} (1/Pascal)
$z_j, \zeta_{x,y,z}$	Complex variables
m_j	Complex non-conjugated roots
k	Stress constant
ς_i	Mapping function of the complex z_j
$K_{Ic,I}$	Mode 1 fracture toughness, stress intensity factor, MPa·m$^{0.5}$(Mega Pascal square root of meter)
a_i	Crack radius at time i, μm (Micrometer)
Y	Crack shape factor
V	Instantaneous crack-tip velocity, m·s^{-1} (Meter per second)
V_B	Crack-tip velocity at branching, m·s^{-1} (Meter per second)
c_R	Rayleigh speed, m·s^{-1} (Meter per second)

R_{XH}	Crystal hackle radius, μm (Micrometer)
$R_{XH\{110\}}$	{110} Crystal hackle radius, μm (Micrometer)
$\theta_{XH\{110\}}$	Angle between the free surface and branching, ° (Degrees)
β	Crack direction, ° (Degrees)
δ	Local angle between main (110) and surface features, ° (Degrees)
n_i	Components of a normal vector to (hkl) plane
$\overrightarrow{X_{[hkl]}}$	Directional vector along [hkl] in $\vec{x}$
$\overrightarrow{Y_{[hkl]}}$	Directional vector along [hkl] in $\vec{y}$
A_{XH}	Predicted crystal hackle constant, MPa·m$^{0.5}$(Mega Pascal square root of meter)
$A_{XH\{hkl\}}^{\langle hkl\rangle}$	Crystal hackle constant, MPa·m$^{0.5}$(Mega Pascal square root of meter)
H, h	Sample thickness, mm (Millimeter)
b	Sample width, mm (Millimeter)
F	Loading force, N (Newton)
L, l	Distance between adjacent loading and supporting roller, mm (Millimeter)
φ_i	Crystallographic hackle directions, ° (Degrees)
θ_B	Crack-tip deflection angle with respect to the mirror's plane, ° (Degrees)
ζ_i	Lateral hackle angle, ° (Degrees)
$\overline{\Delta_{PEAK}}(P_i)$	Averaged distance between hackle maxima from profile P_i, nm (Nanometer)
δ_i	Hackle height, nm (Nanometer)

$\xi_{\{hkl\}}$	Normalized radial distance-to-crystal hackle radius of (110) cleavage
P_{max}	Maximum contact pressure of the Vicker indenters, gf (Gram-force)
E	Isotropic Young's modulus, GPa (Giga Pascal)
ν	Isotropic Poisson's ratio
H_V	Vickers hardness, GPa (Giga Pascal)
$E_{\{hkl\}}^{\langle hkl\rangle}$	Anisotropic Young's modulus, GPa (Giga Pascal)
$\nu_{\{hkl\}}^{\alpha\beta}$	Anisotropic Poisson's ratio
$\mathrm{G}_1, \mathrm{G}_{1c}$	Energy release rate mode 1; critical dynamic energy release rate mode 1, $J{\cdot}m^{-2}$ (Joule per unit crack area)
μ_1, μ_2	Non-conjugated roots pair solution of the bi-harmonic equation
$\xi_{\{hkl\}}^{\langle hkl\rangle}$	Equivalent anisotropic Young's modulus, GPa (Giga Pascal)
$\Gamma_{\{hkl\}}^{\langle hkl\rangle}$	Theoretical fracture surface energy, $J{\cdot}m^{-2}$(Joule per square meter)
$\left\|E_b^{GaAs}\right\|$	Gallium arsenide bonding energy modulus, J (Joule)

CONTEXT AND MOTIVATION

Telecommunications, aerospace, and medicine involve complex devices composed of sensors and actuators. For instance, televisions, laptops, home appliances, and cars use semiconductor crystals. The functional crystals are commonly based on raw materials that are processed into pure or doped single crystals. They typically are converted into thin monolithic materials to increase cost efficiency whose general physical properties are complex. They are available as wafers with at least one side electrochemically mirror polished. Manufacturing steps allow components to be assembled on top of these wafers. Smartphones, industrial equipment, airplanes generally include silicon (Si) and gallium arsenide (GaAs) components to enable high-frequency communication with high performances. Solar cells made from GaAs have superior performance compared to silicon. Although GaAs has technical advantages over silicon, including higher electronic mobility, Si-based wafers are often the economical first choice, roughly a thousand times cheaper to produce than GaAs. Moreover, Si and GaAs are key materials for the development of the next generation of micro-electromechanical systems that will eventually include photonics.

Inevitably, the increasing demand to improve design and efficiency imposes new challenges. Therefore, a transition period systematically occurs during which new processes are developing to make the information traveling safer and faster with robustness and cost-effectiveness. Unfortunately, miniaturization and new packaging create challenging environments, such as unique interfaces, large surface-volume ratios, or abnormally high pressures, heat, generating unexpected material behavior. Single crystals are expensive, and their fracture is an increasing problem for the semiconductor industry as almost all of them have anisotropic physical properties and still unknown failure mechanisms. The manufacture and operation of a single crystal-based sensor or actuator typically involve intrinsic and extrinsic stressors. For the extrinsic stimuli, there are usually thermal cycling, mechanical stresses, handling, humidity. For instance, thermal cycling can simply happen when devices are systematically turned on and off thus introducing heat cycles. Moreover, the critical environment of miniaturized devices allows levels of heat power density that can easily reach

those of a frying pan. The main underlying issue rising is the thermal gradient can be that wide that it can produce either direct damage or introduces residual stresses that lead to mechanical failure. The devices are increasingly designed to be easily wearable, handled, and transported. Therefore, accidental drops leading to catastrophic failure are made very common in different environments. The intrinsic stimuli are more related to misfits between lattice parameters or thermal expansion coefficients mismatch. These extrinsic and intrinsic stressors could lead to high detrimental stress in the range of Giga-Pascal and damage from scratching, delamination, with possible other unknown combined failure modes. Unfortunately, there are neither existing standards to evaluate them nor relevant understanding addressing the anisotropy to satisfactorily evaluate them.

Although the existing techniques to measure mechanical properties are quite reliable in structural materials, their millimeter-scale resolution becomes unsuitable for microsystems with a dimension of a few microns and less. Unfortunately, knowledge from isotropic materials is not directly transferable to anisotropic single crystals. The stress field is distributed depending on the crystal orientation and flaws in the material leading to failure and leaving complex fractographic morphologies. All over the world, specimens that are broken daily (thereby causing electronic device failures) are routinely replaced without considering mechanical issues and without addressing the problem for the next generations of devices because of the market pressure. It is valuable to mention that such type of technical materials does not constitute an infinite resource on Earth. Furthermore, the semiconductor industry can easily be affected by any disruption either in the demand patterns or in supply chains (for example production shut down indirectly caused by tsunami, earthquake, pandemic...) and lead to a drastic semiconductor shortage as now in 2021, it is observed as it was in 2011. Therefore, it has become crucial to save resources by limiting useless waste. It is at this point that the present project of investigating the failure in functional crystals to fundamentally understand failure and eventually help produce more responsibly takes all its sense.

CHAPTER 1

STATE OF THE ART

This chapter introduces the general principles and concepts of fractography which deals with how to use newly created material's fracture surface from broken fragments to understand the fast crack propagation and retrieve the material's history. This work is focused on the mechanical history of the materials and is oriented more specifically in the fracture strength prediction based on the "semiconductor waste" or available fragments. A review of fracture surface features is presented along with the mirror's evaluation in brittle solids. It distinguishes the isotropic case from the anisotropic one and gives an overview of how the fracture strength prediction is done using quantitative fractography. In the second sub-section, the dynamic stress fields models are introduced and compared at the crack-tip with given factors that describe the crack propagation.

1.1 Fractography

1.1.1 Isotropic Fracture in Brittle Materials

Fracture morphologies are usually observed when brittle solids fail. Features are induced on the surfaces after the dynamic crack propagates depending on the structure of the material and the loading type. The fracture origin, relatively flat "mirror" region, "mist" region, and "hackles" are schematically represented in Figure 1.1.

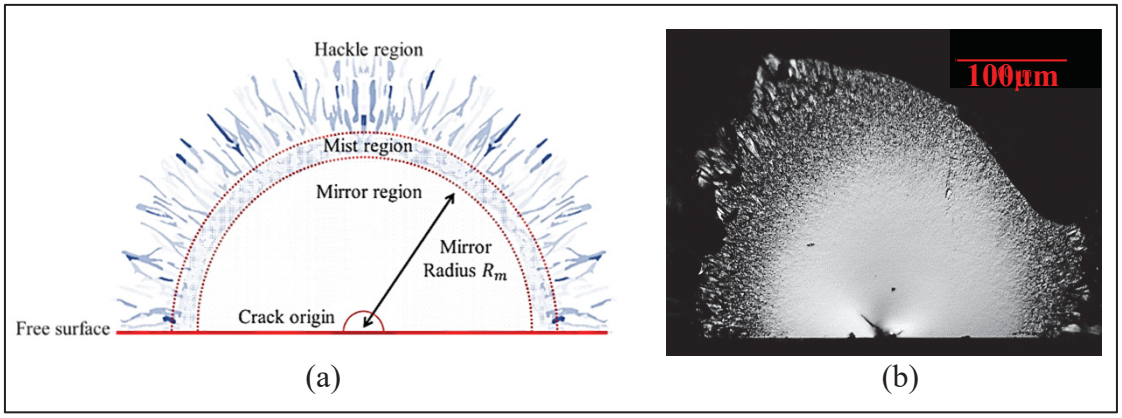

Figure 1.1 (a) Fracture surface scheme of isotropic material adapted from ASTM (2010, p. 2) and (b) fracture surface of a borosilicate glass after bending test

In brittle solids, such as ceramics or glasses, the length between the origin and the mirror-mist boundary, R_m, is commonly correlated to the strength of the material given by an empirical equation initially tested in 1940 and officially postulated in 1972:

$$\sigma_f = A_m / \sqrt{R_m} \tag{1.1}$$

taken from (Orr, 1972) where σ_f is the strength at failure, R_m is the mirror radius; A_m is the empirically obtained material-dependent mirror constant. Orr's equation is often employed in fractography to estimate the fracture stress level for a broad range of isotropic materials. Moreover, Wallner gave his name to specific markings created during crack propagation. "Wallner lines" have been found when the crack front interacted with reflected stress waves (Wallner, 1939) and was essential in understanding the surface markings although no study existed to investigate its relevance to the mirror's definition. Mirror constants of glasses and small grain ceramics are well established and have led to the creation of a standard (ASTM, 2010a) which recommended measuring the mirror radius on the free surface. However although isotropic bulk materials propose a relatively invariable mirror, it has been shown that there was a scaling effect particularly with thin modern components where Orr's equation linearity was questionable (Ma, Dugnani, & Moulins, 2018). Moreover, a positive intercept, attributed to forming residual stress, was systematically obtained when applying Orr's equation

although inconsistent with a forming process that should generate compressive stress (i.e., negative stress). This underlines the many inconsistencies between the quantitative methods used to characterize the properties of isotropic materials and their behavior ultimately rising questionable practices and standards. Figure 1.2 shows the history of fractography as a rich and exciting blend of material science, mechanical engineering, fracture mechanics, powerful imaging analysis tools that evolve for more than half a century.

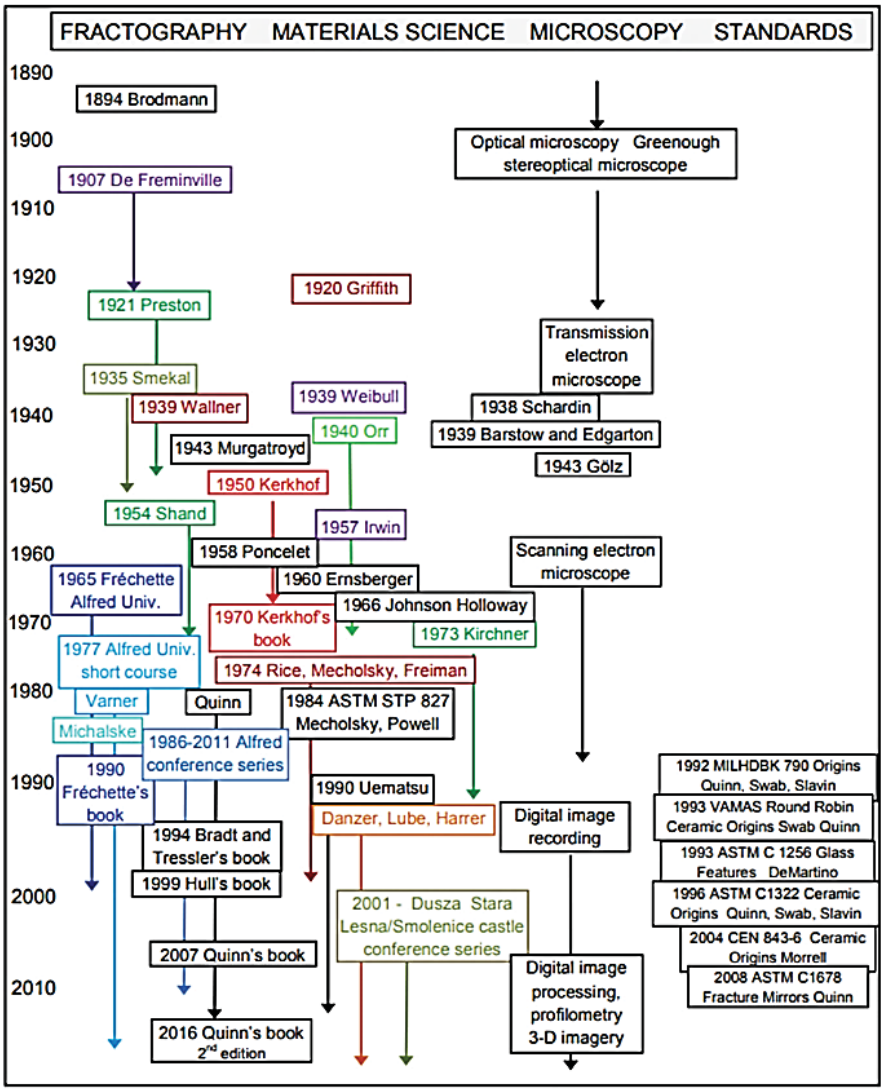

Figure 1.2 The history of standards and fractography of isotropic brittle materials taken from Quinn (2016, p. 1-9)

Mirror constants have been measured by some authors but without a consistent measurement method, experimental protocol, or loading direction reference to the crack origin. Unfortunately, this understanding cannot be directly transferable to single crystals and could not be generalized to other oriented materials. Unfortunately, in Figure 1.2, no standards have been established for the case of single crystals such as for GaAs or Si, as cubic crystals, and yet, anisotropic fractographic procedures should look alike with some subtleties. In single crystals, a fracture surface is considered flat as a mirror for low speeds. When the crack speed increases up to a critical velocity, the crack branches and the fracture surfaces display common features with the case of isotropic material up to the branching. However, fracture beyond branching does not always display the same characteristic features on the free surface (Dugnani & Verghese, 2014; Quinn, 2016). Therefore, the mirror radius and branching typically measured on the isotropic specimen, remain unclear in anisotropic functional crystals.

1.1.2 Anisotropic Surface Features in Single crystals

Although fractographic methods were primarily developed for isotropic materials, direct measurements of characteristic single crystal fracture still have been performed since the 1940s. However, they were rather used to study the nucleation and growth of crystals (Harkins, 1942; Zapffe & Worden, 1949a, 1949c, 1949b). One of the first observations to understand the fracture surface features were done to explain the origin of tear marks. They have been done on diamond cubic germanium (Ge) by Haneman et al. who observed that most of these steps did not start at the origin but more at a distinct length at some distance from the free surface (Haneman & Pugh, 1963) where the origin was surrounded by a relatively smooth area Figure 1.3.

Figure 1.3 Fracture surface of cleaved single crystal germanium taken from Haneman et al. (1963, p. 2)

Haneman et al. explained that tear marks were generally curved and as a result, steps were non-crystallographic. However, steps are a basic feature of cleaved single crystal surfaces and occur when a crack moves on close and parallel atomic planes. Although such a mechanism has not been fully explained or understood because of the scale, it is known as being crystallographic. They hypothesized that there were two ways in which tear marks could be generated when the crack attained a critical velocity, or when the crack tip was deviating from its initial fracture plane, but no crystallographic reference orientation was given, and a clear fractographic analysis procedure was not available to help support both hypotheses. Therefore, they had potentially misinterpreted the nature as well as the onset position of the local crystallographic markings that delineated the effective mirror boundary. Nevertheless, they associated the smooth region near the origin with the mirror region as usually observed in isotropic materials. They also reported a curved region within the conchoidal fracture as previously detected by Gilman in lithium fluorite (LiF) and zinc (Zn) generated when cracks and screw dislocations are intersecting (Gilman, 1958, 1959).

Hereafter, Rice explained that twin boundaries and steps could be preferential paths of fracture surface formation as in the apparent cleavage features of sapphire (J. J. Mecholsky, Freiman, & Rice, 1976) but detailed studies were not provided. In his work, he indicated that screw dislocation could be considered as an essential source of fracture steps and pointed out that single crystals generally exhibit the same fracture features as glasses and polycrystals. Unfortunately, there were no given arguments to support this, and he pointed that there were pronounced crystallographic effects that were not yet wholly documented or understood. Nonetheless, he found that the crystallographic dependence of the shape or partial or complete absence of mist and hackle to define mirror dimensions showed that appropriate levels of stress intensity or velocity were necessary but not sufficient for the formation of mirrors or branches.

It was more evident, at this point, that single crystal fracture surfaces required a certain intensity of stress and/or a critical crack velocity to provoke such geometrical structuration of the surfaces. Accordingly, mist and hackle formation represented either a different degree of the same mechanism of the fracture surface formation or a different mechanism since such steps frequently extended entirely back across the mirror region to the crack origin of single crystals. Such steps also were observed on crystal fractures having no mist and hackle and extended back across mirrors. Quinn collated useful information about fractographic patterns (Quinn, 2007, 2016) and listed a remarkable variety of anisotropic signatures of fractured single crystals such as "cathedral mirrors," "gull-wing mirrors," "inclined cathedral mirrors," and "whisker spears". Unfortunately, no attempts were made to correlate these spectacular morphologies with the mechanical properties of the single crystals. Figure 1.4 presents some of the fractures mirrors regions that were collated by Quinn where he explicitly wrote that "mirror sizes may be extremely difficult or impractical to measure" (Quinn, 2007, 2016).

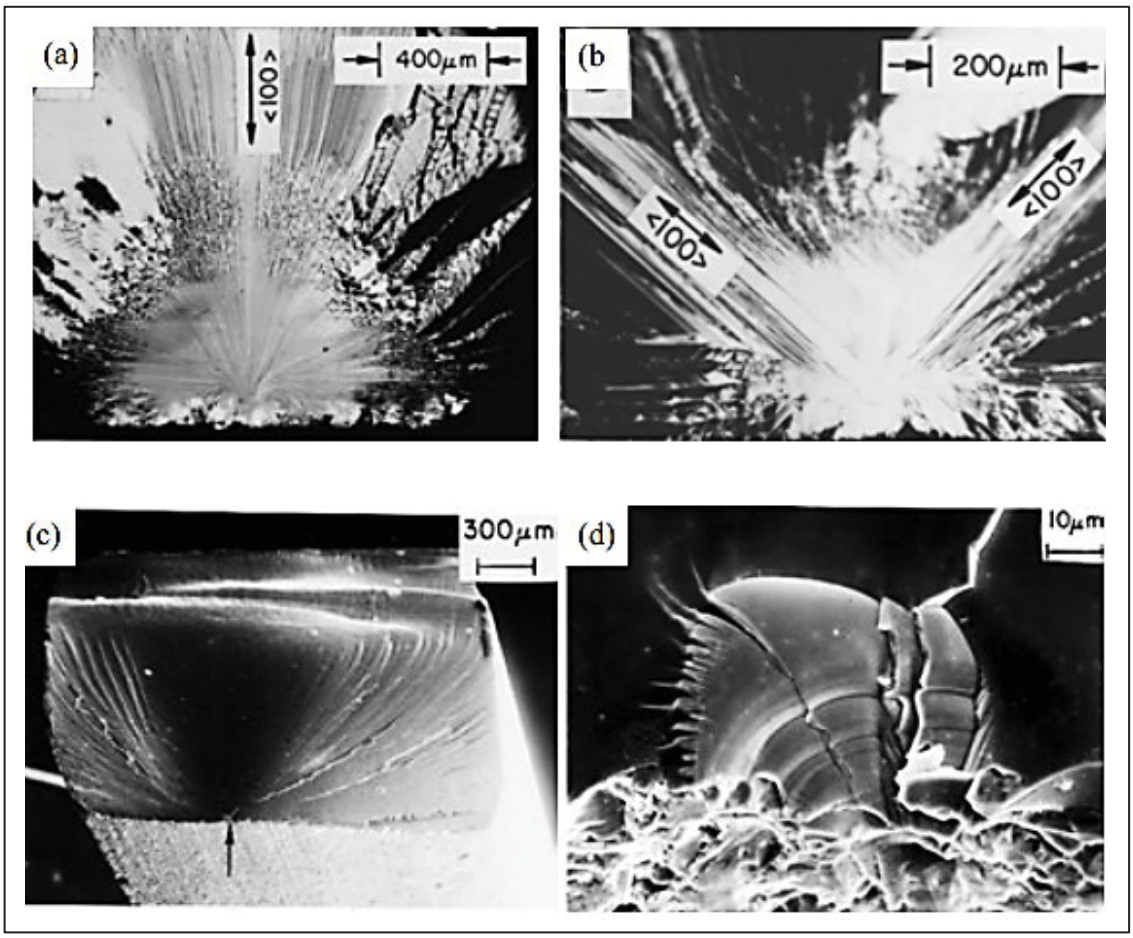

Figure 1.4 Single crystal fracture surfaces of (a) and (b) magnesium oxide (MgO) for two tensile orientations and (c) and (d) cubic zirconia for two bending orientations taken from Quinn (2016, p. 8-1)

What is interesting in Figure 1.4 is that as in Figure 1.3, it shows that single crystal fracture surfaces were not a manifestation of a genuinely brittle failure since slight deformation could be associated with mirror formation. Moreover, the mirrors did not have the same geometrical configuration according to the loading and the material structure. Unfortunately, no clear understanding was provided to investigate how the resulting slip bands in MgO were potentially affecting mist and hackle. Fracture mirrors were reported distorted when the stress normal to the fracture surface was varying or elongated due to flexural stress gradients. At this point, the alignment of principal maximum stresses with crystals was attracting the interest to

develop a solid understanding elucidating unconventional/unknown mirrors with odd shapes and markings.

The correlation of the mirror with stresses was initially applied to single crystal alumina by Abdel-Latif et al. who used an approached similarly to Mott's approach to obtaining another formulation for the mirror constant (Abdel-Latif, Tressler, & Bradt, 1978; Mott, 1938). However, Abdel-Latif mistakenly considered an isotropic media. He also used an inappropriate stress correction factor concerning the triangular stress field for flexure. In the same period, Mecholsky et al. measured fracture mirror boundaries in amorphous and small grains ceramics, single crystal, and polycrystalline ceramics (J. Mecholsky, Freiman, & Rice, 1978; J. J. Mecholsky et al., 1976). Orr's relation was used to compute the mirror constant. Regrettably, no method was introduced to explain how they measure the "mirror" radius (Figure 1.5). They reported that step features, as well as hackle markings, also appeared on the fracture surfaces of single crystals depending on the orientation of loading.

Figure 1.5 Ammonium Diphosphate single crystal fracture where the mirror (mist) boundary is located between white arrows taken from J. J. Mecholsky et al. (1976, p. 1311)

To reduce the complexity, the SIF at the mirror boundary represented by the mirror constant they measured, was defined as the “average” fracture toughness of the material because of the large size of the crack compared to the microstructure. They hypothed that the mirror constants could be used to predict flaw sizes or fracture energy in single crystals and glasses, as well as polycrystalline because the empirical mirror constants obtained were proportional to the "averaged" critical SIF. Again, neither crystallographic references were given for the fracture toughness nor crack propagation direction and they finally concluded that the case for single crystals was too complicated because of the elastic anisotropy.

Precedents works recognized that the mirror’s formation in anisotropic single crystals was associated with a critical crack-tip velocity, critical SIF, the material’s intrinsic crystal structure, and the loading orientation but Kirchner and Kirchner found the mirror constant depended also on the crack shape although he did not take into account dynamic energy losses and did not proposed a study on the evolution of the crack shape during propagation (Kirchner & Kirchner, 1979). Tanaka et al. investigated the fracture of a single crystal of manganese zinc ferrites (MnZn) and found that fracture morphology was varying following the (100) and (110) cleavage planes (K. Tanaka, Kitahara, Ichinose, & Iimura, 1984). Their work was also suggesting that cracks required a certain amount of kinetic energy to become unstable, again, consistent with the need for a critical crack-tip speed to mark fracture surface. Furthermore, Kaufman et al. (Kaufman & Forty, 1986) reported that the initial deviation from the main (111) cleavage plane of Si was producing V-shaped markings (Figure 1.6).

Figure 1.6 Detailed "V-shape" markings of cleaved Si taken from Kaufman & Forty (1986, p. 3170)

It was the first time that fractographers consistently observed clear transition features between the flat mirror and branching in a single crystal Si. Figure 1.7 shows the silicon fractographic patterns that Tsai et Mecholsky reported (Tsai & Mecholsky, 1991) concerning the definition of the mirror's region in silicon (Tsai & Mecholsky, 1991).

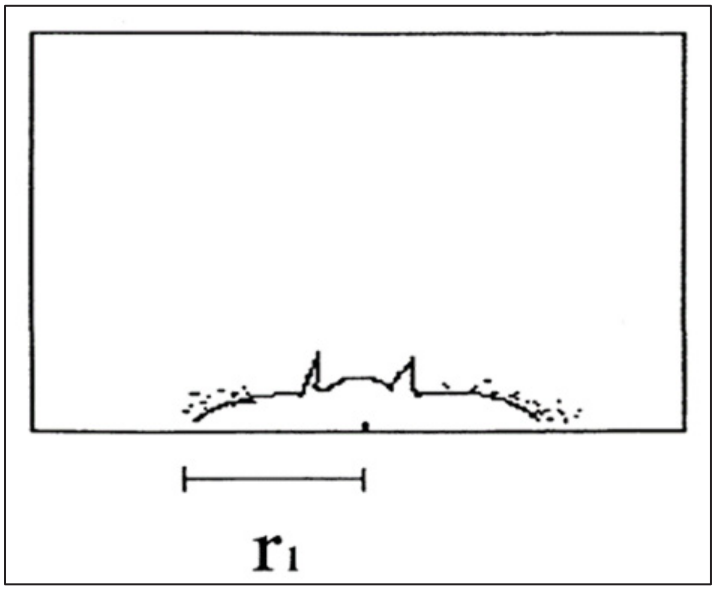

Figure 1.7 Fracture mechanics description of r_1 as the mirror-mist radius in single crystals taken from Tsai et Mecholsky (1991, p. 1255)

In Figure 1.7, the pattern was initially described by Mecholsky and al. as the apparent “Batman-like” mirror radius. At this point, it was also the first time that fractographers came up with a proposition of a mirror boundary definition for a well-known single crystal such as the Si. They proposed, later on, similar work with an updated estimation of a “fracture mirror” boundaries Figure 1.8 (Tsai & Mecholsky, 1992).

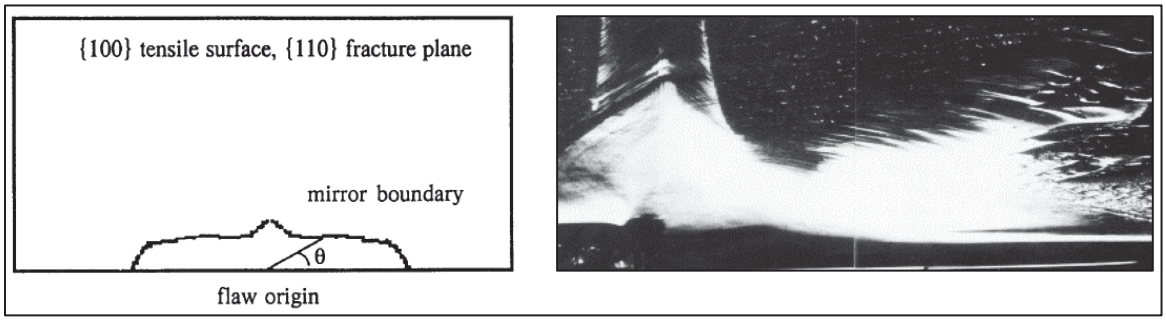

Figure 1.8 Estimation of the “mirror” region for single crystal silicon {100} tensile surface, {110} fracture plane taken from Tsai et Mecholsky (1992, p. 174-176)

Regrettably, the evaluated boundary remained poorly representative of the mirror region in Figure 1.8, as it was mostly considering the first Wallner lines boundary formed on the surface rather than the mirror/branching boundary. Furthermore, Orr’s equation initially developed for isotropic materials was used to estimate the strength of silicon single crystal without any fractographic method and the crystallographic reference directions. Regretfully, they mistakenly considered that the fracture occurred at the same energy level whereas the complex topography of the surface was composed of different families of planes and would require the evaluation of each set of fracture energy according to the branching and mirror planes composition.

In fact, in these materials the fracture is convoluted by crystal cleavage, thereby occluding the mirror-mist boundary that is essential for an analysis based on established principles. Some authors have attempted to apply Orr’s equations on various other single crystals but had difficulties dealing with the anisotropy that is inherent to single crystals (J. Mecholsky et al.,

1978; J. J. Mecholsky et al., 1976; Tsai & Mecholsky, 1991, 1992). In these cases, the mirror constant was found to depend on the crystalline plane and structure considered and on the observation technique and procedure used as well. Although some limitations existed in the models proposed by Mecholsky et al., Dugnani and Zednik, Abdel-Latif, Bansal, and Kirchner and Kirchner, all perceived that the "mirror constant" was depending on a critical crack-tip speed, SIF, loading scenario, the stress field, specimen size, and the flaw shape and distribution.

Sherman et al. intensely studied fracture of single crystal silicon stating that "fracture initiation, crack propagation, and crack path in single crystal brittle solids does require precise knowledge and understanding of the fracture events on the atomistic scale" (Sherman, 2006; Sherman & Be'ery, 2003, 2004; Sherman, Markovitz, & Barkai, 2008b). Sherman also pointed out the fact that the deflection phenomenon was providing a good way for analyzing critical velocities in brittle crystals and showed that a crack propagating in the (110) Si plane would deflect to the (111) plane at a velocity of nearly $0.65c_R$ (Sherman, 2009). Regrettably, it was only explained that c_R was so far from predicting the critical speed because of the difference between continuum mechanics versus the atomistic approach. Therefore, dynamic instabilities driven by energy dissipation in the atomic structure were left behind. Although they suggested that fracture does require precise knowledge and understanding of the fracture events on the atomistic scale, no clear understanding of the mechanisms was proposed, and they were only suspecting possible phonon radiations emissions as an extra energy consumption mechanism for the crack-tip deflection. Pons et al. supposed mixed mode was at the origin of dislocation and twinning systems so that, for instance in cubic GaAs, crack segmentation would produce stepped surfaces typically found in materials such as steels, glasses, polymers, and rocks (Pons & Karma, 2010). However, these fractographic markings have neither been observed nor reported in GaAs or Si single crystals before.

Another study carried out on silicon single crystal, involving the existence of instabilities fracture experiments. In this study, a multi-scale phenomenon was described (Kermode et al., 2008) with an atomistic simulation. Low-speed crack propagation reasonably high velocities

crack moving on the (110) plane could become unstable and deviate onto (111) planes. Although this gives a good idea concerning the crack behavior for cubic single crystals, such crack deflection has never been understood clearly or measured in single crystals. Nevertheless, the idea of a crack oscillating onto (110) and (111) planes could justify the typical hackle patterns also seen in granites and silicon (Bahat, Bankwitz, & Bankwitz, 2003; Kermode et al., 2008; Sherman, 2009; Sherman et al., 2008b).

Moreover, step hackle lines have often been reported during crack instabilities as terrace-like kinks (Lawn, 1993) that could happen because of a misaligned plane leading to an in-plane mode mixity (Sherman et al., 2008b). Regretfully, hackle markings are usually confused with radial striæ (Bahat et al., 2003) which are not running on very close parallel planes from the same plane family. Furthermore, striæ do not change their orientation following the stress distribution along with the thickness as step hackle lines. For some authors, striæ formation occurs in GaAs because failure mechanisms answer to strain first with slipping or twinning activity before cleavage and are possibly related to a lamellar substructure of the crystal (Zapffe & Worden, 1949c, 1949b). However, lamellar substructure has not yet been found in GaAs, and specific topographic features necessarily occurred when a specific combination of SIF and crack velocity happens at the crack tip. Some average critical SIF values for the (111) fracture plane orientation have been shown (Chen, 2002; Margevicius & Gumbsch, 1998) to be equivalent for the (110) planes ranging from 0.45 to 0.49 MPa$\sqrt{m}$. Although the SIF is expected to depend on the plane considered, other authors (Michot, George, Chabli-Brenac, & Molva, 1988; Yasutake et al., 1988) have also reported the same fracture toughness for the (100) plane (Chen, 2002; Margevicius & Gumbsch, 1998).

Finally, the mixed-mode is often reported to be involved in single crystal deformation. Unfortunately, the scale of the problem, the local free energy density computation, and the experimental tracking remain the main challenges even with phase-field or any other atomistic modeling. Hence the most effective and straightforward methods involve advanced fractographic techniques. A theory to predict the surface topography for an unstable anisotropic crack is lacking, and none of the existing paths allows to foresee the roughness scale in the vicinity of a crack to identify mirrors in functional crystals.

Fractographic measurements on single crystals do not pertain to any standard since no general method exists to establish a single crystal mirror constant when fracture patterns likely depend on the anisotropy of the crystal with a combination of critical crack-tip speed and SIF. Much uncertainty exists as to whether this possible understanding can be extended to GaAs and Si single crystals or even be generalized for cubic single crystals. Nonetheless, best strength estimates are important for failure analysis, where innovative and surface profilometry methods (Ma & Dugnani, 2018) are emerging, giving more accurate and concise mirror boundaries definitions. Thus, the local propagation of the crack and small-scale surface markings needs to be further explored and correlated with specific SIF conditions near the fracture origin in anisotropic single crystal-based semiconductors.

1.2 Crack Propagation

1.2.1 Framework

All time-dependent problems involving, highly brittle materials and then rapid fracturing, propagation, or arrest, resides within dynamic fracture mechanics. The main dynamic fracture mechanics problem dealing with bodies under fixed loading that contains a rapidly moving crack is emphasized in this manuscript for the case of orthotropic bodies. Problems in dynamic fracture mechanics might include five key aspects such as:

- the start of fast crack extension
- the resulting crack paths
- the crack tip velocity
- the crack’s branching
- the crack’s arrest

Dynamic fracture mechanics generally assumes the material to be continuous. This section maintains the linear elastic continuum view under small-scale yielding, consistent with most of the research and application in the domain and the volume of the material studied. Crack propagation in a brittle solid is driven by the stresses in the vicinity of the crack and by factors

that describe the local resistance in fracturing such as the SIF. For an ideal crystal with a linear elastic behavior, both analytical and numerical methods are used to obtain stresses and displacements in the presence of a crack.

1.2.2 Fracture Modes and Formalisms

Crack-tip fields are of fundamental importance because they link local events at the crack tip to macroscopic loading. The three modes of crack deformation are defined by the stresses in the vicinity of the crack. The three fracture modes possess symmetry properties as presented in Figure 1.9.

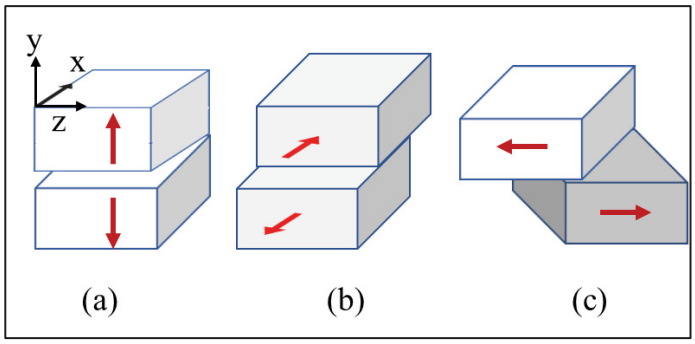

Figure 1.9 Crack opening modes:
(a) I opening, (b) II sliding, (c) III tearing

The Westergaard stress function method (Westergaard, 1939) was developed for analyzing these crack problems. The crack-tip fields for a stationary crack field can be derived either by the complex potential method (Muskhelishvili, 1954) or by the method of eigenfunction expansion (Williams, 1961). The method used to deal with plates containing cracks is usually the complex function method which suits almost perfectly for 2D plane anisotropic elasticity. The elastic fields have been obtained by Muskhelisvili, Lekhnitskii, and Sih et al. in homogeneous materials (Lekhnitskii, 1963; Muskhelishvili, 1954; Sih, Paris, & Irwin, 1965). Muskhelishvili obtained the solution for an isotropic plate containing a finite crack with a concentrated force applied normal to crack's faces. He used limiting values of the stress functions taking advantage of specific properties of the Cauchy type integrals whereas Lekhnitskii obtained expressions for stresses in anisotropic bodies with cracks. However, Sih et al. and Williams found expressions for stresses in anisotropic bodies with cracks, examining

the nature of the local stress field in a more general sense. Sih and Eftis and Liebowitz work indirectly pointed out that Westergaard stress function suffered from a restriction, and that in symmetric problems, it allowed only a hydrostatic tension. They added a corrective term to the Airy stress function (Eftis & Liebowitz, 1972; Paris & Sih, 1965). They gave more details for the general behavior of crack tip stress fields for the uniform tension and bending of an orthotropic plate. The formalism of Stroh (Stroh, 1958) was employed to investigate the stress and displacement fields near the crack tip of a dynamically extending crack in an anisotropic body. Indeed, Stroh formalism provided an optimal form to solve elastic problems allowing to build an efficient numerical procedure to solve incremental problems. Adopting the linear dislocation array viewpoint, Stroh suggested the value of the constant for crack nucleation, basing his calculations on a Griffith-type energy balance. These results were relevant to understand the process and nature of fracture mechanisms. Regretfully, the influence of the crack tip velocity on the stresses and displacements fields in the vicinity of the crack was not considered in almost all these previous works.

The theory of dynamic fracture mechanics was significantly expanded by Mott and Yoffe (Mott, 1948a, 1948b; Yoffe, 1951). Yoffe investigated a steady-state crack extending in an elastic body in uniform tensile stress. The problem of a crack symmetrically expanding at a uniform stress field was also treated by Atkinson in the anisotropic materials (Atkinson, 1965a, 1965b). The solution was derived by a complex potential method, and the steady-state propagation of a semi-infinite crack using the Cauchy integral formula was studied. For a continually growing crack, the asymptotic near-tip fields expressing the displacements regarding a shear potential and a longitudinal potential were derived by Rice later (J. R. Rice, 1968). Another work from Freund et al. showed that the fields in the vicinity of a running crack were of the same forms as those derived by Rice except that the velocity was replaced by the instantaneous crack velocity (Freund & Clifton, 1974). At this stage, although crack-tip speed was included in the analytical derivations, it remained mostly an unvarying condition in the propagation process as crack was at a steady-state regime.

Willis developed a general framework for analyzing self-similar problems in elastodynamics and gave a formal solution to the crack problem for a general anisotropic material (Willis,

1975). However, Kassir and Tse, Arcisz, and Sih worked more specifically on orthotropic materials class with cracks as well as Piva (Arcisz & Sih, 1984; Kassir & Tse, 1983; Piva, 1986). They obtained the stresses and displacements of an extending crack at a constant speed. Regretfully, the dynamic SIF was not representative in the vicinity of the crack and again a steady-state crack-tip was considered at a constant speed.

Lee et al. (K. H. Lee, Hawong, & Choi, 1996) had proposed a similar study, but their work was done under dynamic plane mode. Equations between dynamic SIF, stresses, and displacements were derived for mode I and II crack opening. The analysis presented by Wu (Wu, 2000) based on Willis's work expressed the general full-field solution regarding eigenvalues and eigenvectors. The general solution contained complex functions in the subsonic regime for dynamic crack growth in the general anisotropic material. To go through the dynamic problem, the proposed formulation was related to that for steady-state motion. Wu et al. derived a dynamically extending crack in an anisotropic body (Gao, Hou, Kang, & Wang, 2013; Wu, 1989, 2000) using the Stroh formalism (Stroh, 1957, 1958, 1962) to derive the dynamic fields and the dynamic energy release rate (ERR).

More recently, Gao et al. considered a moving crack in a more general anisotropic body (Gao, Kang, & Wang, 2009). Strain energy density theory was applied to obtain the tilting crack angle. They found that the fracture angle not only depended on the crack velocity but also the anisotropy of the material. It was the first work that paid more attention to the branching stage of dynamic propagation. However, they reported that the faster the crack velocity was, the less the dynamic crack extension angle was. Regretfully, it appears inconsistent with the previous work done in fractography of single crystals stating that a critical crack-tip velocity was required to create crack branching (i.e., crack characterized by inclinations/kinks and extension angle). Regretfully, at this point, all reported analytical works were neither combined with image analysis nor empirically validated on anisotropic single crystals specimens for critical velocity values in the branching region. The path described by a crack theoretically has been proven to comply with local symmetry principles (Gol’dstein & Salganik, 1974). Indeed, if a stationary crack is subjected to Mode II, it should extend to annihilate the sliding forming a

sharp kink. The angle of such deviation is usually perpendicular to the maximum tensile stress. Unfortunately, in anisotropic materials, no evidence has been found to confirm that a fast crack necessarily moves perpendicular to the maximum tensile stress. Yoffe addressed a criterion based on a critical velocity to explain crack branching occurrences. However, branching was empirically found occurring at velocities much less than the critical one. As a result, above the experimental “branching” velocity, a crack would be able to deviate out of its original plane.

Most of the actual knowledge on fracture criteria is based on slowly moving cracks below c_R and is not envisioning the transient stage or its boundary that could have potentially represented the branching state observed in single crystals. Disappointedly, universal principles or criteria have only been proposed considering the influence of the crack-tip speed for the branching formation without developing a physical understanding of the crack deflections itself or based on any relevant intrinsic physical properties.

CHAPTER 2

RESEARCH OBJECTIVES

2.1 Overall Purpose

Accidental fractures, either during material manufacturing or in-use operation necessarily require the causes to be understood based on mechanical history. Unfortunately, neither fractographic standard methods nor failure criteria in anisotropic brittle materials have been proposed before this work. This section introduces the general objective of the thesis by focusing on the influence of the crystal anisotropy and the SIF according to the fractographic mirror-branching boundary formation. It proposes methods to evaluate the multiscale state of stress in semiconductor crystals developing a fundamental understanding of the crack-tip deflections addressing crystal anisotropy. This is achieved by leveraging "post-mortem" fractographic traces left by cracks after the propagation with the development of a relatively simple analytical model.

Three sub-objectives are defined:

- The first is to identify, analyze and characterize the fractographic singularities of Si and GaAs anisotropic crystals.
- The second is to generalize the existing fundamental principles of fractography from empirical isotropic fracture to anisotropic facture. It consists of understanding how the experimental fracture stress can be correlated with the experimental fracture surfaces that have unknown and odd mirror shapes.
- The third is the development of a dynamic crack propagation model that predicts fracture dynamics in anisotropic functional crystals for the cubic class. An analytical approach is used, based on generalizing existing linear elastic fracture mechanics models and correlating the model with data from laboratory testing. Therefore, it includes the model validation with empirical data based on a common

and relevant failure criterion. The central assumptions and hypotheses are listed below.

2.2 General Assumptions

- Single crystals are brittle anisotropic homogeneous and continuous bodies. Our analysis is limited to crystals with cubic symmetry.
- When the crack is about the fracture process area in terms of size (2-3nm), the continuity assumption in linear elastic fracture mechanics is violated. Fracture mechanisms are at the atomistic level and an energy approach must be used. The driving force for crack propagation is the total free energy in the entire mechanically strained body
- Continuum mechanic methods account for almost all the strain energy and offer a relevant description of the crack's dynamic behavior. Dynamic fields in the vicinity of a crack can be described with complex potential representation, and continuum linear elastic fracture mechanics applies up to the branching.
- Steady-state motion exists but no slower-moving steady-state crack exists below 20% of C_R and propagating cracks radiate phonons.
- Cracks become unstable as in amorphous materials but generate anisotropic branching events.

2.3 Hypotheses

- General fractography principles in isotropic materials can be adapted to strongly oriented materials with reference directions and appropriate material's orientation
- Topographic features of anisotropic crystals are comparable to those of isotropic materials but vary following the crystal structure.
- Fracture morphologies of ideally perfect anisotropic single crystals have specific patterns which are dependent on the orientation of stresses/crystals and the intrinsic crystal primal structure.

- The Mirror region can be used to evaluate dynamic or quasi-static parameters from steady-state crack growth (crack velocity, dynamic SIF) as well as mechanical properties (fracture strengths, residual stresses).
- The Mirror-mist region could be occulted because of dynamic surface markings and instabilities but is consistently bounded by branching in a single crystal
- Mist-branching boundary is a delineated curve of “iso” energy where critical energy and velocity are reached with the steady-state cracks that become unstable, deviate/branch marking the surface, and then decelerating.

2.4 Methods

2.4.1 Experimental Flexural Tests

For this project, the surface of rupture of crystals was studied after the samples were overloaded experimentally. It included preliminary work of pre-cleavage steps and orientation identification steps with adhesives to prepare the prismatic samples for the mechanical tests on different scales of length. Rectangular samples were prepared from standard {100} wafers then loaded until fracture using a three-point bending fixture in
Figure 2.1. The experimental procedures included tests by three points bending carried out based on the standard for ceramics, adapted to the need for smaller geometries.

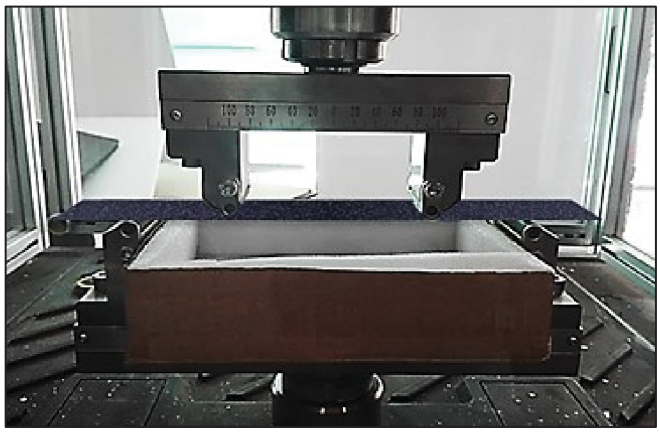

Figure 2.1 Photograph of GaAs beam sample from{100} wafer on the setup of the flexural test

The 3PBT was done on an MTS Model with a 50 and 100 N load cell (resolution 0.01N) and roller diameter 5- and 10-mm. Adhesive tape was used on the unpolished compressive side of the samples. Test specimens were loaded using displacement control at a fixed speed of 0.5 mm/min. Linear elastic response during experiments justified the use of linear elastic beam theory to compute the fracture strengths.

2.4.2 Vickers Indentation

To achieve the indentation of single crystals, the device used was a micro-indenter B-type with an automatic microhardness tester from the company Clemex (see

Figure 2.2). This micro-indenter offered the possibility of making Vickers indentations with a pyramidal diamond tip and an integrated optical microscope coupled with an automatic image analysis imprint detector for the hardness evaluation. Vickers indentation allowed relatively small deformation with symmetrical cracking. The technique was only minimally destructive, as it requires very small volumes.

Figure 2.2 Photograph of the Clemex micro-indenter

2.4.3 Microscopy Techniques and Image Analysis

The approach with existing fractographic principles applicable to the isotropic materials characterization was studied and extended to anisotropic systems. The project focused on the analysis of semiconductor crystals of different dimensions with strong orientation dependence. The fracture surfaces were characterized using a powerful industrial Olympus LEXT OLS4100 confocal optical microscope optimally designed for the inspection of semiconductors and circuits such as for micro-nano profile measurements, surface roughness measurement, volumetric reconstruction as presented in Figure 2.3.

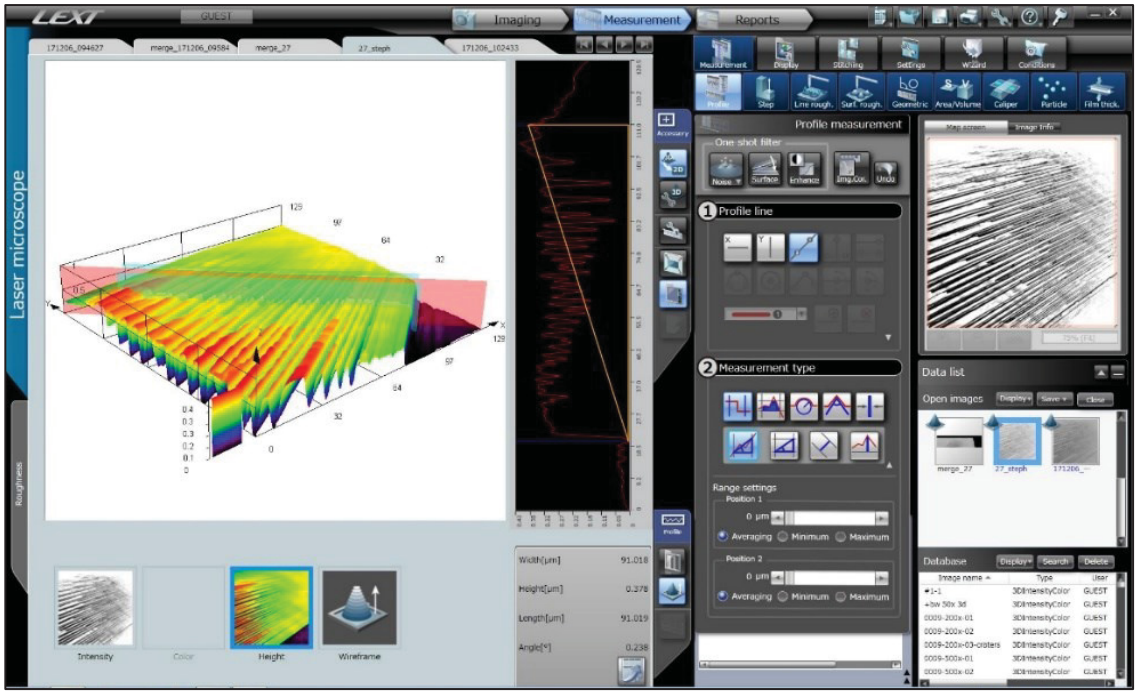

Figure 2.3 Screenshot of a Confocal 3D laser GaAs scan using OLS4100 microscope from Olympus

OLS4100 was used to measure the topographic singularities of the cleavage surfaces accurately. It was made possible due to the short wavelength radiation. The resolving power of the UV-light source was around 405 nm. It proposed a much higher resolution to distinguish two objects than conventional optical light. Finally, the laser differential interference contrast

method was used to increase the contrast between the flat mirror and the mirror's surface contours.

The post-mortem image analysis treatments were performed with MATLAB, a multi-paradigm numerical computing environment. The image analysis included:

- 3D surface reconstruction
- Sample orientation with crystallographic references
- semi-automated pattern recognition algorithm for mirrors in silicon
- 3D volumetric transformation to 2D angular mapping
- Passband for the crystallographic angles

2.4.4 Anisotropic Elasticity and Complex Variable Approach

In this section, dynamic crack growth in general anisotropic materials is emphasized. The main results concerning the elasticity and dynamic fields in the vicinity of the crack are rigorously derived for the opening mode I. Among all the existing analytical methods, the complex potential method was chosen. This choice enabled the problem to be reduced to leverage the existing analytic functions with the appropriate boundary conditions.

2.4.4.1 Elastic Stiffness

For anisotropic fractures, cracks orientation can be associated with a crystallographic direction defined by the triplet $\langle hkl \rangle$ and used to compute the elastic stiffness of the material. In the case of strongly oriented crystals, the mechanical anisotropy can be considered for any $\langle hkl \rangle$ crystallographic zone axis, and calculated using exactly:

$$1/E_{\langle hkl \rangle} = s_{11} - 2\left((s_{11} - s_{12}) - \frac{1}{2}s_{44}\right)(m^2n^2 + n^2p^2 + m^2p^2) \qquad (2.1)$$

taken from Hopcroft (2010, p. 233) where m, n and p are the direction cosines of the angle lying between the crystallographic direction $\langle hkl \rangle$ and the following crystal axis X (100), Y (010), and Z (001) according to the specimen orientation. S_{ij} are the elastic coefficients from the reduced cubic compliance matrix in Voigt form. Similarly, the ratio of strain between two orthogonal directions α and β can be computed for arbitrary directions in a cubic crystal with a Poisson's ratio $\nu_{\alpha\beta}$ relation such as:

$$\nu_{\alpha\beta} = -\frac{s_{12} + (s_{11} - s_{12} - \frac{1}{2}s_{44})(m_\alpha^2 m_\beta^2 + n_\alpha^2 n_\beta^2 + p_\alpha^2 p_\beta^2)}{s_{11} - 2(s_{11} - s_{12} - \frac{1}{2}s_{44})(m_\alpha^2 n_\alpha^2 + n_\alpha^2 p_\alpha^2 + m_\alpha^2 p_\alpha^2)} \tag{2.2}$$

taken from Hopcroft (2010, p. 234) where m_i and n_i are the direction cosines for a plate to α the directions of the plate curvature, and β the directions in the plane of the plate.

2.4.4.2 Mechanical Stresses

Analytic stress functions were used as a solid base in this work and were subjected to further adaptation for the case of cubic semiconductor crystals. The work also included a complementary failure-branching criterion such as the maximum K_I criterion. This criterion considered that the crack propagates initially on the {hkl} mirror plane as long as the normalized stress at the crack-tip orthogonal to the mirror plane, i.e. $\sigma_{\perp\{hkl\}}/K_{Ic\{hkl\}}$, becomes non-negligible compared to the normalized stress orthogonal to the {ijk}-branching plane, i.e. $\sigma_{\perp\{ijk\}}/K_{Ic\{ijk\}}$. The principle of fractography, based primarily on the correlation of the mirror region with fracture strength was used as an index to characterize the state of stress of single crystals semiconductors after a fracture.

The two crack faces move only in the displacement u_y, and in a symmetrical way compared to (xz). The general complex potential method is used to describe the elastodynamic fields at the tip of an anisotropic body and is based on Gao's solutions. Consider a crack's length of 2a

extending with a constant velocity v along the X-axis. There is no tension at the edges of the flaw but uniform biaxial and shear loads at infinity as shown in Figure 2.4.

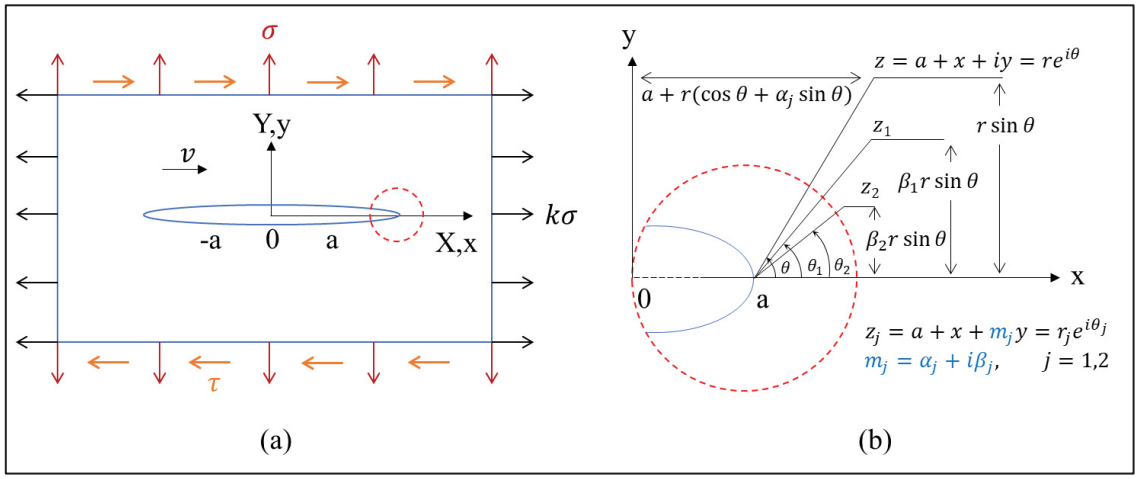

Figure 2.4 (a) loading conditions and geometry of the crack and (b) the coordinate system

The stresses equilibrium in OXY coordinate system is:

$$\begin{cases} \dfrac{\partial \sigma_x}{\partial X} + \dfrac{\partial \tau_{xy}}{\partial Y} = \rho \dfrac{\partial^2 u_x}{\partial t^2} \\ \dfrac{\partial \tau_{xy}}{\partial X} + \dfrac{\partial \sigma_y}{\partial Y} = \rho \dfrac{\partial^2 u_y}{\partial t^2} \end{cases} \tag{2.3}$$

where t is time, ρ is the density of the material, and u_x and u_y are the displacement components. The transformations $x = X - vt$ and $y = Y$ are more suitable to express the equilibrium equations introducing the moving coordinate system oxy such as:

$$\begin{cases} \dfrac{\partial \sigma_x}{\partial x} + \dfrac{\partial \tau_{xy}}{\partial y} = \rho v^2 \dfrac{\partial^2 u_x}{\partial x^2} \\ \dfrac{\partial \sigma_y}{\partial y} + \dfrac{\partial \tau_{xy}}{\partial x} = \rho v^2 \dfrac{\partial^2 u_y}{\partial x^2} \end{cases} \tag{2.4}$$

The complex variable is defined as $z = x + my$ with $m = \alpha + i\beta$. Stress-strain relation with compliance coefficients S_{ij} and analytic Airy stress function ψ are used to obtain stress components:

$$\begin{cases} \sigma_x = \zeta_x \dfrac{\partial^2 \psi}{\partial z^2} \\ \sigma_y = \zeta_y \dfrac{\partial^2 \psi}{\partial z^2} \\ \tau_{xy} = \zeta_{xy} \dfrac{\partial^2 \psi}{\partial z^2} \end{cases} \tag{2.5}$$

where $\zeta_{x,y,z}$ are expressed as:

$$\begin{cases} \zeta_x = (1/m)[m^3 - m\rho v^2(S_{22} + mS_{16} - S_{12}) + \rho^2 v^4(S_{16}S_{22} - S_{12}S_{26})] \\ \zeta_y = (1/m)[m - \rho v^2(S_{26} + mS_{11} - mS_{12}) + \rho^2 v^4(S_{11}S_{26} - S_{12}S_{16})] \\ \zeta_{xy} = (1/m)[-m^2 + \rho v^2(S_{22} + m^2 S_{11}) + \rho^2 v^4(S_{11}S_{22} - {S_{12}}^2)] \end{cases} \tag{2.6}$$

Substituting the stress-strain equations and Airy stress components into the strain-compatibility equation leads to the biharmonic equation of the holomorphic function:

$$(m^4 + \lambda_1 m^3 + \lambda_2 m^2 + \lambda_3 m + \lambda_4)\frac{\partial^4 \psi}{\partial z^4} = 0 \tag{2.7}$$

and λ_i $(i = 1,2,3,4)$ are functions of the density, the speed, and the compliance coefficients.

The solution for Eq.(2.7) has the following form:

$$\psi(z) = \psi_1(z_1) + \psi_2(z_2) + \overline{\psi_1(z_1)} + \overline{\psi_2(z_2)} = 2\mathrm{Re}[\psi_1 + \psi_2] \tag{2.8}$$

with Re which is the real part of the complex and m_1, m_2 are the roots of the characteristic equation that are always complex or purely imaginary appearing in conjugated pairs:

$$m^4 + \lambda_1 m^3 + \lambda_2 m^2 + \lambda_3 m + \lambda_4 = 0 \tag{2.9}$$

The solution of an anisotropic elasticity plane problem involves the determination of functions that satisfy the boundary conditions of the crack region. Then the following couple of equation is considered:

$$\begin{cases} \phi(z_1) = \dfrac{d\psi_1}{dz_1},\ \phi'(z_1) = \dfrac{d\phi}{dz_1} \\ \chi(z_2) = \dfrac{d\psi_2}{dz_2},\ \chi'(z_2) = \dfrac{d\chi}{dz_2} \end{cases} \tag{2.10}$$

If $k = 0$, no shear loads are found at infinity and letting $S_{11} = S_{22}, S_{16} = S_{26} = 0$, one can obtain for a cubic material and pure tension in mode I all dynamic crack tip stresses such as

$$\begin{cases} \sigma_x = 2\mathrm{Re}[\zeta_x(m_1)\,\phi' + \zeta_x(m_2)\,\chi'] \\ \sigma_y = 2\mathrm{Re}\big[\zeta_y(m_1)\,\phi' + \zeta_y(m_2)\,\chi'\big] \\ \tau_{xy} = 2\mathrm{Re}\big[\zeta_{xy}(m_1)\,\phi' + \zeta_{xy}(m_2)\,\chi'\big] \end{cases} \tag{2.11}$$

$$\begin{cases} u_x = 2\mathrm{Re}[p_1\phi(z_1) + p_2\chi(z_2)] \\ p_1 = S_{11}\zeta_x(m_1) + S_{12}\zeta_y(m_1) + S_{16}\zeta_{xy}(m_1) \\ p_2 = S_{11}\zeta_x(m_2) + S_{12}\zeta_y(m_2) + S_{16}\zeta_{xy}(m_2) \end{cases} \tag{2.12}$$

$$\begin{cases} u_y = 2\mathrm{Re}\{q_1\phi(z_1) + q_2\chi(z_2)\} \\ q_1 = \dfrac{1}{m_1}\big[S_{12}\zeta_x(m_1) + S_{22}\zeta_y(m_1) + S_{26}\zeta_{xy}(m_1)\big] \\ q_2 = \dfrac{1}{m_2}\big[S_{12}\zeta_x(m_2) + S_{22}\zeta_y(m_2) + S_{26}\zeta_{xy}(m_2)\big] \end{cases} \tag{2.13}$$

After introducing a mapping function, the section of the real axis can be mapped into a unit circle ϱ in the η plane. Once integrated all around the unit circle, η is mapped into the z plane to rewrite $\phi(z_1)$ and $\chi(z_2)$.

These analytical functions are more conveniently relocated at the crack tip using the coordinate ς_j such as:

$$\varsigma_j = z_j - a = r\left(\cos\theta + m_j \sin\theta\right), \quad z_j = x + m_j y \ \ (j = 1,2) \tag{2.14}$$

Finally, after substituting terms from Eq.(2.11) and ignoring higher-order terms, the general dynamic crack-tip field can be obtained for cubic crystals. They were adapted from Gao et al. (2009, p.76) such as:

$$\sigma_x = \frac{K_I}{\sqrt{2\pi r}} Re\left[\frac{1}{\zeta_y(m_1)\zeta_{xy}(m_2) - \zeta_y(m_2)\zeta_{xy}(m_1)}\left(\frac{\zeta_x(m_1)\zeta_{xy}(m_2)}{\sqrt{cos\,\theta + m_1\,sin\,\theta}} - \frac{\zeta_x(m_2)\zeta_{xy}(m_1)}{\sqrt{cos\,\theta + m_2\,sin\,\theta}}\right)\right] + Re\left[\frac{\zeta_x(m_2)\zeta_{xy}(m_1) - \zeta_x(m_1)\zeta_{xy}(m_2)}{\zeta_y(m_1)\zeta_{xy}(m_2) - \zeta_y(m_2)\zeta_{xy}(m_1)}\sigma\right] \tag{2.15}$$

$$\sigma_y = \frac{K_I}{\sqrt{2\pi r}} Re\left[\frac{1}{\zeta_y(m_1)\zeta_{xy}(m_2) - \zeta_y(m_2)\zeta_{xy}(m_1)}\left(\frac{\zeta_y(m_1)\zeta_{xy}(m_2)}{\sqrt{cos\,\theta + m_1\,sin\,\theta}} - \frac{\zeta_y(m_2)\zeta_{xy}(m_1)}{\sqrt{cos\,\theta + m_2\,sin\,\theta}}\right)\right] \tag{2.16}$$

$$\tau_{xy} = \frac{K_I}{\sqrt{2\pi r}} Re\left[\frac{1}{\zeta_y(m_1)\zeta_{xy}(m_2) - \zeta_y(m_2)\zeta_{xy}(m_1)}\left(\frac{\zeta_{xy}(m_1)\zeta_{xy}(m_2)}{\sqrt{cos\,\theta + m_1\,sin\,\theta}} - \frac{\zeta_{xy}(m_2)\zeta_{xy}(m_1)}{\sqrt{cos\,\theta + m_2\,sin\,\theta}}\right)\right] \tag{2.17}$$

2.5 Approach

The complex potential method was adopted for the crack-tip stress field description. In the experiments, stress was applied via externally controlled boundary conditions. The resulting behavior of the cracks was observed by analyzing fracture surfaces using confocal microscopy and combining advanced image analysis processing. The existing standard procedures were used as a base and adapted to characterize the anisotropic features of the fracture surfaces with crystallographic references. The experimental mirror-branching radii were used as a scaling factor to predict the fracture stress. The analytical stress fields from the theoretical model were combined with post-mortem image analysis results (i.e., the experimental mirror-branching constant) to confirm the behavior of the dynamic cracks and fracture surface morphologies. Analytical geometry was used with crystallographic stereograms to confirm the experimental symmetries observed follow the intrinsic cubic symmetries of the single crystals. Key physical properties of the crystals were evaluated with simplified energy concepts based on the stress field results obtained from the complex variable approach for the evaluation of fundamental material's properties such as the critical stress intensity factor and the energy release rate in functional anisotropic crystals.

CHAPTER 3

DYNAMIC CRACK MODELING AND ANALYTICAL STRESS FIELD ANALYSIS IN SINGLE CRYSTAL SILICON USING QUANTITATIVE FRACTOGRAPHY

Anthony Moulins[a], Lingyue Ma[b], Roberto Dugnani[b] and Ricardo J Zednik[a]

[a]Department of Mechanical Engineering, École de Technologie Supérieure,
1100 Notre-Dame West, Montreal, Quebec, Canada H3C 1K3
[b]UM-Shanghai Jiao Tong University – Joint Institute, Shanghai, China

Paper published in *Theoretical and Applied Fracture Mechanics (TAFM)*, October 2020

3.1 Abstract

Single crystal silicon is the fundamental building block enabling today's plethora of integrated electronic components. However, complex mechanical stresses, originating from either direct mechanical loading or thermal cycling, can result in fracture of the constituent silicon, one of the leading causes of semiconductor device failure. Although phenomenological relationships to estimate the fracture strength in silicon have been proposed in the past, no quantitative fractographic method addressing the intrinsic anisotropy of crystals exists. In this work, a fractographic approach using optical confocal microscopy and atomic force microscopy is developed to identify and analyze the cleavage planes associated with dynamic instabilities in single crystal silicon. We analytically determined the dynamic crack propagation behavior and asymptotic stress field at the crack-tip for unstable, anisotropic, circular cracks in silicon. The fractographic features predicted by the analytical model are consistent with experimental observations, and correctly predict how the {111} planes define the fractographic mirror region, as well as the {112} planes associated with fractographic Wallner lines. These findings have important consequences in reducing mechanical and thermomechanical failure in semiconductor devices, where the mechanical strength is highly dependent on crystallographic anisotropy.

Keywords: single crystal silicon, mechanical stress, semiconductor failure, fracture, fractography, anisotropy, dynamic instability, hackle constant, mirror constant.

3.2 Introduction

Single crystal silicon has been used in semiconductor devices for over half a century. Modern devices in telecommunications, aerospace, and medicine extensively utilize interconnecting silicon-based transistors, capacitors, and sensors (Blakemore, 1982; Hjort, Soderkvist, & Schweitz, 1994). Silicon crystals are manufactured into strongly oriented wafers (Hopcroft, Nix, & Kenny, 2010; Lekhnitskii, 1963), resulting in mechanical anisotropy. The presence of preferential cleavage planes is responsible for the specific patterns featured on the fracture surfaces (Ebrahimi & Kalwani, 1999; Kirchner & Kirchner, 1979; J. Mecholsky et al., 1978; Quinn, 2016; Sherman, 2009). Silicon ingots are usually cut, thinned, and used without encapsulation to reduce parasitics, packaged into confined devices for wearability and cost reduction. Unfortunately, as the silicon wafer's thickness is reduced, the effects of steep thermal gradients, expansion coefficient mismatches, and applied external loads become more and more detrimental (Uchida et al., n.d.). The increasingly important nanometer length-scale of modern devices provides additional challenges, although powerful tools to deal with the assessment of silicon can be used as long as there is no breakdown of continuum theory (Gallo, Hagiwara, Shimada, & Kitamura, 2019; Gallo, Yan, Sumigawa, & Kitamura, 2020; Sumigawa et al., 2017). The failure analysis of fractured silicon crystals is essential to understand failure modes and improve semiconductor device reliability. Unfortunately, although various relationships to estimate the fracture strength in silicon have been proposed in the past, no industry standard or quantitative fractographic method addressing the intrinsic anisotropy inherent in silicon crystals exists.

Silicon fracture's fractographic signature for (110) fractures was accurately documented and described by the work of Tsai and Mecholsky (Tsai & Mecholsky, 1991). Notably, Tsai and Mecholsky attempted to model the crack propagation behavior in silicon to establish the location of the 'mirror-mist boundary.' Although the model could accurately describe the fractographic features observed in (110) fractures, it neglected inertia effects (Tsai &

Mecholsky, 1992) and over-simplistically assumed that all fractographic features formed at the same critical value of the energy release rate. As the mirror region in silicon is bounded by different fracture planes, establishing the boundary of the mirror zone would require separating the critical fracture energy for each set of planes. Tsai and Mecholsky's accurate description of the mirror-mist boundary seemed to be mostly coincidental as cleavage energies in silicon are nearly identical (Sherman, 2006). The weakest cleavage planes in silicon are known to be the {111} planes where $K_{Ic\{111\}}$ = 0.82 MPa√m (Chen & Leipold, 1980). However, fracture toughness on the {110} and {100} planes have been reported marginally higher, i.e., $K_{Ic\{110\}}$ = 0.90 MPa√m and $K_{Ic\{100\}}$ = 0.95 MPa√m respectively.

Building upon Tsai and Mecholsky's findings, the work of Dugnani and Verghese (Dugnani & Verghese, 2014) recognized that two separate families of branching planes bounded the mirror region. Dugnani and Verghese (Dugnani & Verghese, 2014) proposed two alternative methods to measure the mirror radius at 90º (r_{90}) and 45º (r_{45}) with respect to the free surface to account for the two families of branching planes (Dugnani & Verghese, 2014). Dugnani and Verghese (Dugnani & Verghese, 2014) phenomenological study explained how to estimate the fracture strength for both families of fracture features but was unable to clarify the origin and relevance of each set of features.

In addition to silicon in the diamond-cubic crystal structure, the literature is rich with fracture surface analysis of a range of anisotropic materials, including lithium fluoride, spinel, sapphire, and other crystal symmetries (Dugnani & Verghese, 2014; J. Mecholsky et al., 1978; Quinn, 2016; Sauthoff et al., 1999; Tsai & Mecholsky, 1992). Fractographic features, including the relatively flat "mirror" region, the "mist" region (ASTM, 2010a), "hackles", and Wallner lines (Wallner, 1939) are found when the crack-front propagates and possibly interacts with reflected stress waves in single crystals (Dugnani & Verghese, 2014; Sauthoff et al., 1999; Tsai & Mecholsky, 1992). Like the work done on single crystal silicon, these other studies also relied on the phenomenological description of the fracture surface to estimate the material's fracture strength without formally accounting for the inherent anisotropy of the material.

For example, in brittle, isotropic solids, such as small grain ceramics or amorphous materials, the length between the fracture origin and the mirror-mist boundary is commonly correlated to the strength of the material expressed by an empirical equation postulated by Orr (Orr, 1972):

$$\sigma_f \sqrt{R_m} = A_m \tag{3.1}$$

where σ_f is the strength at failure, R_m is the mirror radius; A_m is the empirically obtained material-dependent mirror constant. In small grain ceramics or glasses, the fracture surface is not flat but rather the roughness increases (Dugnani & Zednik, 2013, 2016) as the crack-tip becomes "dynamically unstable". For single crystals, the crack surface is often atomically flat near the fracture origin and eventually, once a critical value of the crack-tip velocity is reached, the crack branches out of the flat mirror plane. The distance between the crack origin and the onset of branching for a given fractographic direction constitutes a recurrent characteristic length associated with dynamic instabilities (Dugnani & Verghese, 2014; Tsai & Mecholsky, 1992), analogous to the mirror radius R_m. Although the exact process of feature formation is strongly affected by the crystal orientation relative to the stress field, the crystallographic planes associated with specific crystal/stress orientations have not been formally addressed prior to this work (Abdel-Latif et al., 1978; Dugnani & Verghese, 2014; J. J. Mecholsky et al., 1976; Tsai & Mecholsky, 1991, 1992).

The aim of this work is, therefore, to develop a quantitative fractographic methodology to understand the fracture behavior of single crystal silicon wafers. This is achieved by leveraging 3D surface profilometries of fractured specimens to provide a *"surface angle mapping"* with respect to the main orientation of the crystal. An analytical solution describing the unstable motion of an anisotropic circular crack is developed to help resolve the issue of determining which family of planes is associated with initial crack branching. The relevant *"crystal hackle radius", $R_{XH\{110\}}$,* which depends on the crystal plane orientations of silicon wafers, is clearly defined and computed at branching for the loading scenario considered. The reciprocal crack lengths at branching are estimated experimentally and correlated with the strength to define the "*crystal hackle constant", $A_{XH\{110\}}$*. The following section intends to support the claim made

in this work that –due to dynamic instabilities– the crack-tip initially deflects from the (110) mirror plane to {111} planes. Furthermore, it will be shown that the features corresponding to the {112} planes were associated with Wallner lines and hence should not be considered as a relevant feature when determining the mechanical strength of a silicon-based device.

3.3 Methodology

3.3.1 Mirror-Branching Formation

Recently, Dugnani and Ma (Dugnani & Ma, 2019) extended Freund's analytical solution (Freund, 1972) describing the motion of unstable straight-cracks in homogeneous, isotropic, brittle materials, to circular-cracks. In this work, Dugnani and Ma's solution was combined with the description of dynamic fields for brittle, anisotropic materials (Gao et al., 2009) to analyze the stress field at the tip of a crack parallel to the (110) plane. The predicted stress-field was used to estimate the crack-lengths at branching and correlate them to fractographic features. The assumptions made in the model were:

(a) the fracture surface was 'atomically flat' up until crack-branching,

(b) the crack's shape remained nearly circular during the initial propagation.

As shown in Dugnani and Ma's work, the crack radius, a, for flat circular-cracks could be related to the instantaneous crack-tip's velocity through the equation:

$$\frac{a_0}{a} = \left[1 - \left(\frac{\pi}{Y^2}\right)\frac{g(V) - 1}{g(V)}\right]^{-1} \tag{3.2}$$

The term a_0 refers to the initial crack-radius and Y to the local shape factor. For isotropic material and a Poisson's ratios in the range $2 / 7 < \nu < 1 / 2$, an approximation for $g(V)$ was given by (Freund, 1972):

$$g(V) \approx 1 - \chi \text{ with } \chi \equiv V/c_R \tag{3.3}$$

In the context of crystal fracture, the term c_R was taken as the Rayleigh velocity in the crack propagation direction. For the fracture surfaces considered in this work, crack-growth initially occurred on the (110) plane and eventually branched onto the (111) plane. In the next sections, a brief description of the dynamic crack-field at the crack-tip and how the knowledge of the field was used to predict the crack-branching is given.

3.3.2 Dynamic Stress Field in Single Crystal Silicon

The dynamic stress-field at the crack-tip as a function of the crack propagation direction, β, was computed exactly using Gao et al.'s two-dimensional, dynamic crack propagation model for anisotropic continuous materials (Gao et al., 2009). The material properties in the direction of the propagating crack were obtained by considering the local compliance matrix in an orthogonal coordinate system defined by the axis of the crack and the β-direction. Similarly, the Rayleigh speed, $c_{R(\beta)}$, was computed in the direction of the crack propagation. The silicon crystal compliance matrix was evaluated based on values reported in Cho (Cho, 2009). Based on Gao et al., the dynamic stress-field in the local polar coordinates at β-direction (Figure 3.1b) was given by:

$$\begin{cases} \sigma_{rr} = \dfrac{K_I}{\sqrt{2\pi r}} Re\left[\dfrac{f_x(m_1)}{\sqrt{\cos\phi + m_1 \sin\phi}} \dfrac{D_7}{D_1 D_7 - D_3 D_5} - \dfrac{f_x(m_2)}{\sqrt{\cos\phi + m_2 \sin\phi}} \dfrac{D_5}{D_1 D_7 - D_3 D_5} \right] \\ \sigma_{zz} = \dfrac{K_I}{\sqrt{2\pi r}} Re\left[\dfrac{f_y(m_1)}{\sqrt{\cos\phi + m_1 \sin\phi}} \dfrac{D_7}{D_1 D_7 - D_3 D_5} - \dfrac{f_y(m_2)}{\sqrt{\cos\phi + m_2 \sin\phi}} \dfrac{D_5}{D_1 D_7 - D_3 D_5} \right] \\ \sigma_{rz} = \dfrac{K_I}{\sqrt{2\pi r}} Re\left[\dfrac{f_{xy}(m_1)}{\sqrt{\cos\phi + m_1 \sin\phi}} \dfrac{D_7}{D_1 D_7 - D_3 D_5} - \dfrac{f_{xy}(m_2)}{\sqrt{\cos\phi + m_2 \sin\phi}} \dfrac{D_5}{D_1 D_7 - D_3 D_5} \right] \end{cases} \quad (3.4)$$

As explained in Gao et al. (Gao et al., 2009), m_1 and m_2 are the roots of the characteristic equation (i.e., the strain compatibility equation), ϕ is the angle between the crack-tip and the branching plane considered, and D_i are constants related to both the material properties along the crack propagation direction and the roots of the characteristic equation. The angle ϕ defined as the relative angle between the plane containing the crack before branching, i.e. (110) and the branching-plane (see, Figure 3.1a). For a semi-circular crack, the angle between the crack-front expanding in the direction β and the (111) plane was computed as:

$$\tan\phi = \sin\beta \cdot \tan(35.2°) \tag{3.5}$$

Equation (3.4) and Eq.(3.5) were used to compute the stresses normal to the (111) plane, $\sigma_{\perp\{111\}}$, as a function of the crack velocity, V.

The stress $\sigma_{\perp\{111\}}$ was obtained by first rotating the local, principal stresses at the crack-tip (i.e., σ_{rr} , $\sigma_{\theta\theta}$, σ_{zz}) by an angle β about the *z-axis* (i.e., the $[\bar{1}10]$-axis), as shown in Figure 3.1b, and subsequently by rotating the stress tensor by 35.2° about the [110]-axis. The expression for $\sigma_{\perp\{111\}}$ was then obtained:

$$\begin{aligned}\sigma_{\perp\{111\}} = \sin^2(35.2°)\,[\sigma_{rr}\sin^2\beta + \sigma_{\theta\theta}\cos^2\beta] + \sigma_{zz}\cos^2(35.2°) \\ - 2\sigma_{rz}[cos(35.2°)\sin(35.2°)\sin\beta]\end{aligned} \tag{3.6}$$

The hoop-stress, $\sigma_{\theta\theta}$, in Eq.(3.6) was obtained assuming plane-strain conditions at the crack-tip. The value of the velocity, V, corresponding to the crack-branching onto the (111) plane was estimated based on the crack-branching criterion outlined in the next section. Once the branching crack-tip's velocity, V_B, had been established, the crystal hackle radius, R_{XH}, as a function of the crack direction, β, was estimated through Eq.(3.2).

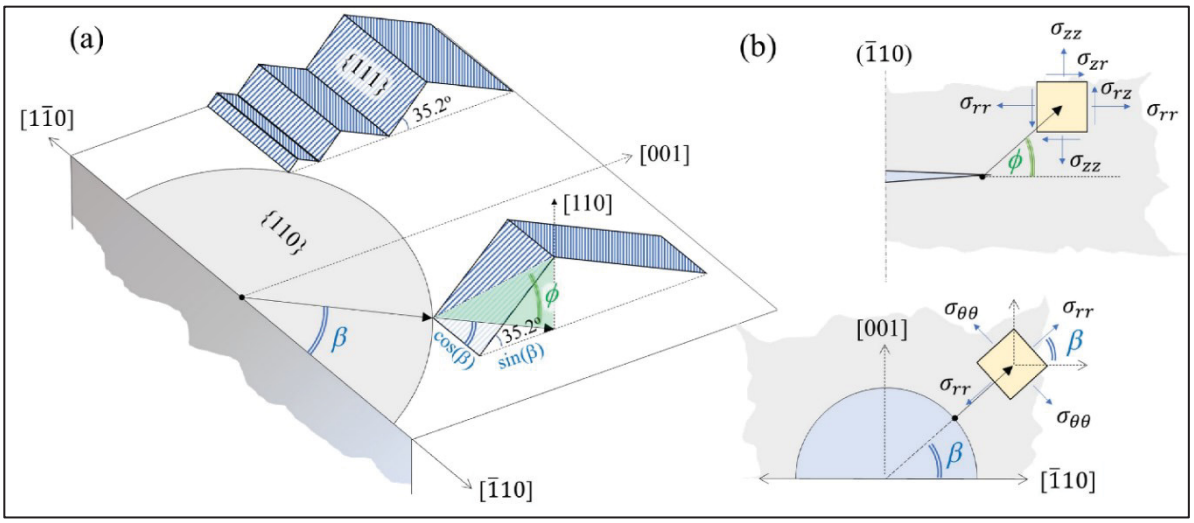

Figure 3.1 Schematic geometry of crack branching from the (110) to the (111) plane, and (b) the stress field at the crack-tip

These dynamic stress field calculations are based on the underlying assumption of a continuous material. When the crack is very close in size to the fracture process zone, the continuous material assumption is no longer valid and the continuity assumption in linear elastic fracture mechanics breaks down due to the atomistic nature of matter. In particular, this length scale has been estimated to be about 2-3nm, on the order of about 10 atoms (Shimada, Ouchi, Chihara, & Kitamura, 2015). Nevertheless, the driving force for crack propagation is the total free energy in the entire mechanically strained body. Atomistic modeling of dynamic fractures using largescale molecular dynamics simulations have shown that continuum mechanics accounts for virtually the entirety of this strain energy; therefore, although strictly speaking the continuity assumption does not apply at the crack tip, continuum mechanics methods have been shown to provide an excellent description of the dynamic behavior of fast propagating brittle cracks (Buehler & Gao, 2006).

3.3.3 Crack-Branching Criterion

In order to predict the fractographic features' formation on the fracture surface, the crack branching-criterion had to be first established. In the past, various criteria have been suggested, but no consensus existed on which best described branching in single crystals (Azhdari &

Nemat-Nasser, 1996). In this paper, the maximum K_I criterion was adopted. This criterion assumes that the crack propagates on the (110) plane as long as the normalized stress at the crack-tip orthogonal to the plane, i.e. $\sigma_{(\perp\{110\})} / K_{Ic\{110\}}$, was larger than the normalized stress orthogonal to the {111}-plane, i.e. $\sigma_{(\perp\{111\})} / K_{Ic\{111\}}$:

$$\frac{\sigma_{\perp\{110\}}(\phi, V)}{K_{Ic}\{110\}} > \frac{\sigma_{\perp\{111\}}(\phi, V)}{K_{Ic}\{111\}} \tag{3.7}$$

K_{Ic} on the (111) plane was chosen based on the value reported by Chen and Leipold (Chen & Leipold, 1980). For K_{Ic} on the (110) plane, the mean value was also based on the value reported by Chen and Leipold, but its magnitude adjusted to account for the anisotropy of the fracture toughness as modeled in Cook (Cook, 2006). Various studies had reported that K_{Ic} was highly anisotropic on the (110) plane, yet relatively uniform on the (111) plane. For instance, Perez (Pérez & Gumbsch, 2000) indicated that the fracture toughness on the (110) plane along the [110] direction was lower than along the [100] direction.

3.3.4 Uniaxial Flexural Tests

The fracture strength of 41 single crystal silicon samples cleaved along the (110) plane was obtained and the corresponding fractographic features recorded. Engineered (001) silicon wafers (boron doped) were used (resistivity below 0.001 Ω.m) to work with short, single crystal beams avoiding high shear stress and defect mobility. The silicon wafers tested in this work had a thickness of H=0.4 ± 0.1 mm with one side mirror polished. The test specimens were 6±1 mm (width) by L=67±15 mm beams, with the [110] direction oriented along the length of the beam. The flexural overloading was performed as three-point bending tests (3PBT) on the tensile side (polished side), and followed ASTM standard C1161 (ASTM, 2013). The 3PBT were conducted on an MTS Model 45 with a 100N load cell (resolution 0.01 N) and roller diameter 5 mm, as illustrated in the schematic Figure 3.2.

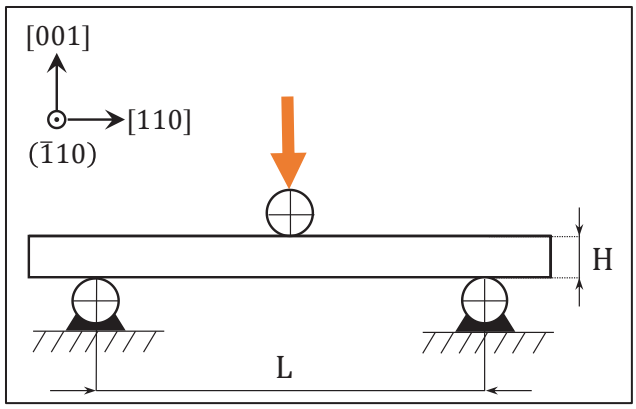

Figure 3.2 Schematic showing a silicon beam undergoing 3PBT with the crystallographic directions

Test specimens were loaded with a stress rate ranging from 2.5-25MPa/s. No notch or pre-crack was introduced to avoid strong misalignment with the (110) cleavage planes. Linear response and small deflections justified the use of linear elastic beam theory to calculate the fracture strength (ASTM, 2013).

3.3.5 3D Surface Characterization

In this section, the technique developed to produce a consistent fractographic characterization of the fracture surfaces and the objective measurements of crystal hackle radii are introduced. Fracture surface maps were obtained using an industrial Olympus Lext OLS4100 confocal microscope with a non-polarized 405 nm laser source of ultraviolet and bright field illumination with 10 nm height resolution and 120 nm lateral resolution to locate fractographic features of interest. A Veeco Enviroscope atomic force microscope with tapping mode was used to track the height variation of the crack branching regions with a resolution up to 7.6 x 10^{-2} nm in height and 1.4 nm in the lateral direction.

The following procedure was employed to characterize the 41 silicon fracture surfaces considered:

- After the fracture surfaces had been cleaned, 3D surface profilometry near the fracture origin was acquired. The fracture surface was oriented with the free surface parallel to $\langle \bar{1}10 \rangle$, the axis of tension. The image of the fracture surface near the origin was leveled by fitting a plane through 3 reference points within the mirror region and then rotated to align with [110].

- The local plane orientation was computed at each pixel using two neighboring data points along [001] and $[1\bar{1}0]$ (see Figure 3.3). Two vectors were then defined, $\overrightarrow{X_{[1\bar{1}0]}} = \begin{pmatrix} rs \\ 0 \\ \Delta z_{AB} \end{pmatrix}$ and $\overrightarrow{Y_{[001]}} = \begin{pmatrix} 0 \\ rs \\ \Delta z_{AC} \end{pmatrix}$ with rs being the lateral resolution (i.e. unit pixel size), $\Delta z_{AB} = z_B - z_A$, and $\Delta z_{AC} = z_C - z_A$. The angle δ between $\overrightarrow{n_{[110]}}$, the normal vector to (110) and the resulting normal vector $\overrightarrow{n_{[hkl]}}$ (i.e. cross product between $\overrightarrow{X_{[1\bar{1}0]}}$ and $\overrightarrow{Y_{[001]}}$) was obtained locally considering all possible crystallographic orientations. The angle δ was then calculated with respect to the first (110) plane cleaving:

$$\delta = arccos\left\{ -\frac{1}{\sqrt{2}} \frac{\Delta z_{AB} + \Delta z_{AC}}{\sqrt{rs^2 + \Delta z_{AB}{}^2 + \Delta z_{AC}{}^2}} \right\} \tag{3.8}$$

where $\overrightarrow{n_{[110]}} = \begin{pmatrix} rs \\ rs \\ 0 \end{pmatrix}$ and $\overrightarrow{n_{[hkl]}} = \begin{pmatrix} -\Delta z_{AB} \\ -\Delta z_{AC} \\ rs \end{pmatrix}$. The angle maps thus obtained were used to identify different families of crystallographic planes.

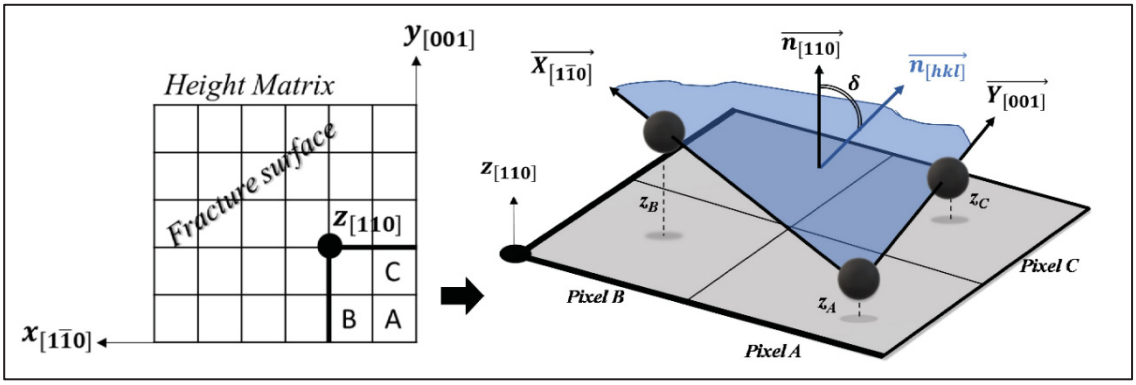

Figure 3.3 Schematic of height matrix (left) showing the blue crystal facet (right) defined by three adjacent reference points. The angle δ between $\overrightarrow{n_{[hkl]}}$ and $\overrightarrow{n_{[110]}}$ is also shown

- The full map was filtered to highlight the features bounding the mirror region, i.e. ,the {111} crystallographic facets as shown later. The crack origin was subsequently estimated at the free surface (Figure 3.4a).

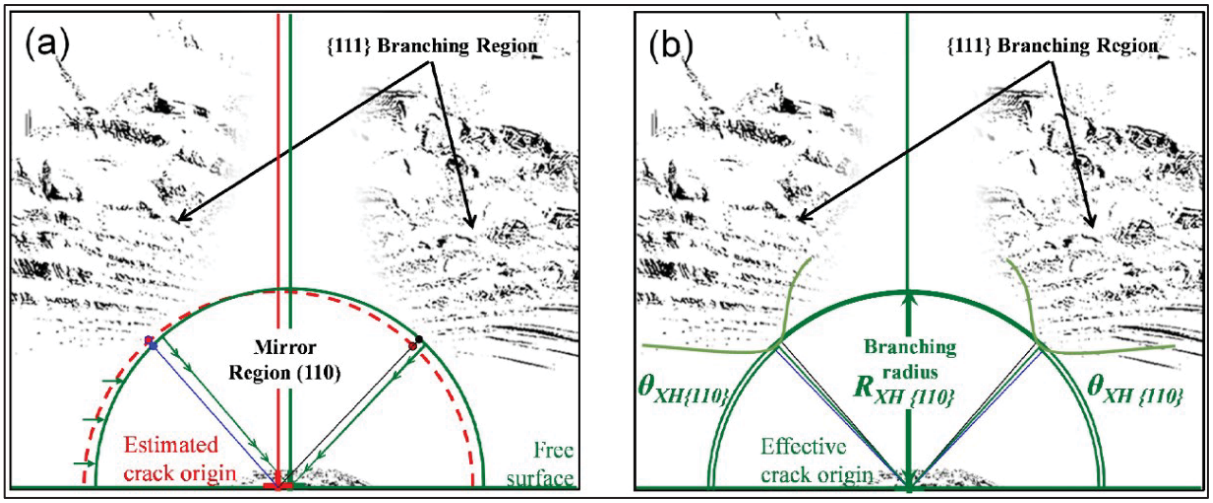

Figure 3.4 Schematic of a surface angle map using a band-pass filter showing (a) the estimated crack origin and the estimated radii at branching, and (b) the effective crack origin and the computed crystal hackle radius with the branching radius direction with the free surface

- The estimation of the radii at branching was achieved using the function “find” from MATLAB R2019a (*MATLAB version 9.6.0.1174912 (R2019a) Update 5*, 2019). The function detected the non-zero elements of the matrix and returned a vector of point indices that had been found. The detected cluster of points (i.e., the branching features) was used to establish the shortest length on each side (i.e., left, and right), and their respective orientations, as shown in Figure 3.4(a). The average of these lengths defined the crystal hackle radius $R_{XH\{110\}}$ and crystal hackle radius direction at branching (i.e., branching radius direction) $\theta_{XH\{110\}}$. For specimens that broke ‘at the edge’, $R_{XH\{110\}}$ and $\theta_{XH\{110\}}$ were obtained considering the single side available.

- The effective crack origin locus was defined using an arc of radius $R_{XH\{110\}}$ tangent to the hackle boundary region on both sides with the center along the free surface as shown in Figure 3.4(b). The analytical shape of the {111} mirror to branching boundary was fitted on the filtered surface angle map using the experimental achievements such as $R_{XH\{110\}}$ and $\theta_{XH\{110\}}$ respectively as shown in Figure 3.4(b). The shortest radius $R_{XH\{110\}}$ was subsequently correlated with the strength of the specimens and the orientations of the two sides with respect to the free surface were analyzed in detail.

3.4 Results

3.4.1 Fractography of Single Crystal Silicon

In this section, the mirror and branching regions are precisely described by AFM profilometries and 3D laser confocal scans. The planes bounding the mirror zone have been separated to objectively provide a measure of crystal hackle radii. AFM surface profilometries were used to generate fractographic surface angle maps Figure 3.5(b) from AFM heights Figure 3.5 (a). The strong surface markings in Figure 3.5(b) indicated that the crack-tip branched from the

(110) plane with facets orientated mostly around ±35° with respect to the mirror plane (i.e. (110) plane at 0°).

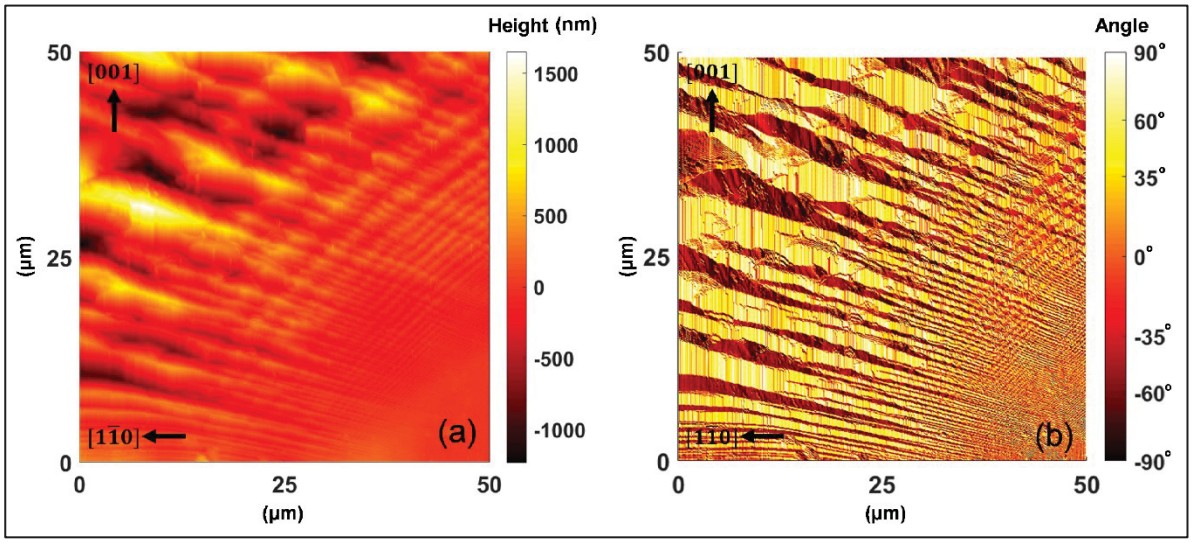

Figure 3.5 (a) AFM height surface of a silicon sample fractured at 249MPa, and (b) corresponding surface angle map showing the orientations of the crystalline facets at branching

These pronounced features were associated with the {111} family of planes (theoretically inclined at 35.2°). Additional, less perceivable surface perturbations are also visible in Figure 3.5(b) running nearly perpendicular to the principal features. The directionality and inclination of these less obvious marks suggested that they might be related to the {112} family of planes. Figure 3.6 shows experimental profilometry carried out by AFM in regions where (a) branching occurred, and (b) at the "cusp". An average planar orientation of 34º with a standard deviation of 11º has been found in concave regions of the profile (a) with an average periodicity of 484 nm. Surface profilometry in Figure 3.6(b) indicated an average angle of 20±6º computed from peaks of nearly the same magnitude which are most probably associated with the {112} family of planes. An average height undulation of 183 nm with an average periodicity of 490 nm was found in concave regions of the profile.

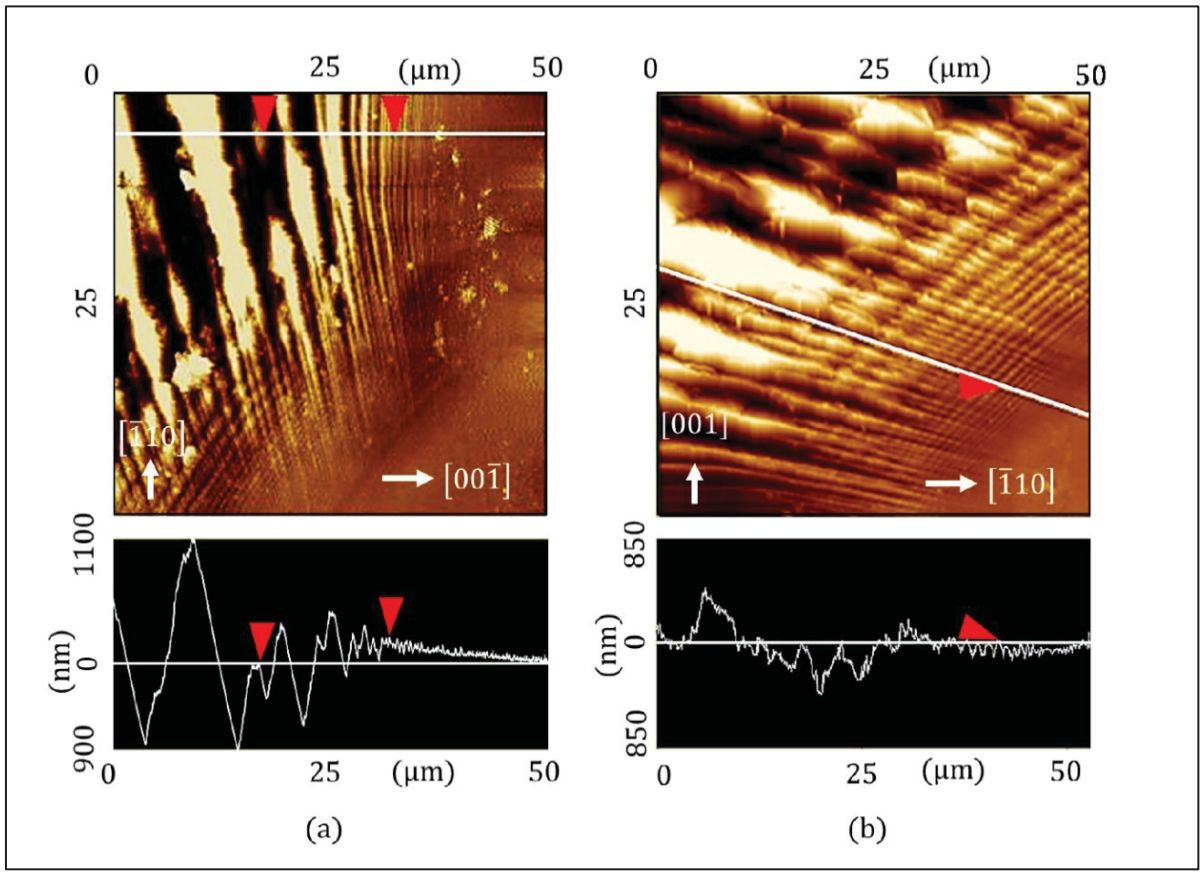

Figure 3.6 Surface profilometry of the silicon fracture surface with AFM tapping mode tracking crack-tip behavior (a) at branching, and (b) in the "cusp" region

For most of the fracture surfaces, the mirror appearance was flat with crack traces fanning out of the origin and out of the mirror plane (i.e., the (110) plane) systematically surrounding the mirror region, for instance in Figure 3.7. Most of the specimen broke with crack origins 'away from the edge'. Figure 3.7 shows examples of variations in the fracture morphologies for two samples displaying nearly the same strength. The sample in Figure 3.7(a) broke at 204 MPa and the specimen in Figure 3.7(b) broke at 212 MPa with a larger flat mirror region. The shapes of the 'flanks' were very similar for both specimens whereas the instability marks above the crack origin (i.e. the so-called "cusp") are significantly less noticeable in Figure 3.7(b).

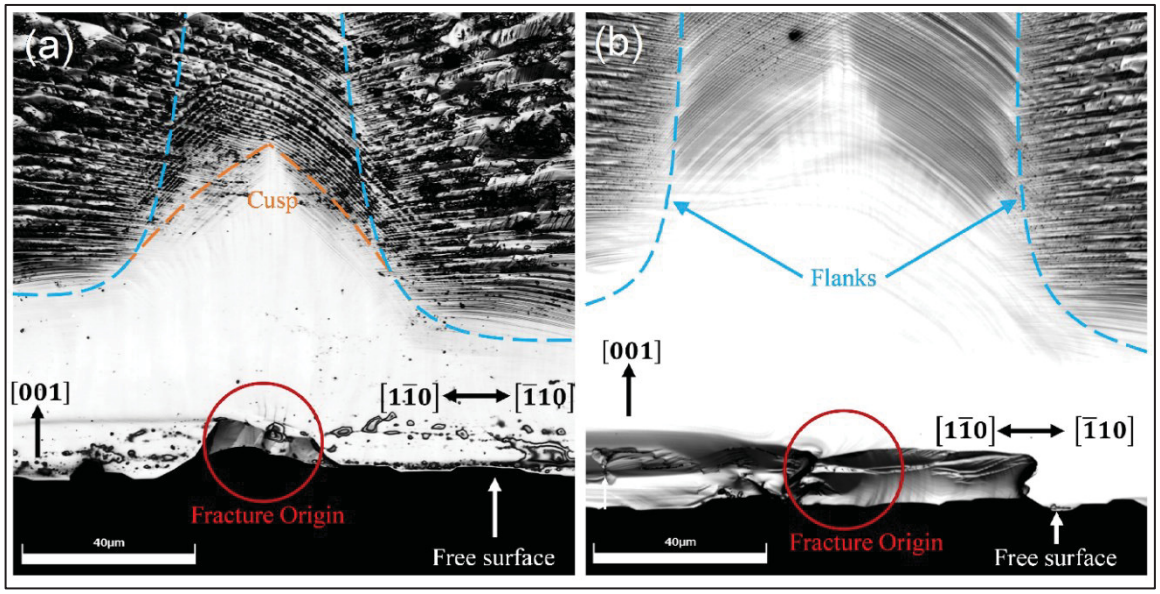

Figure 3.7 Typical cleaved surfaces of single crystal silicon under UV laser illumination near the fracture origin

As outlined previously, 3D confocal optical microscopy was mainly used to characterize the overall region surrounding the mirror region and to generate angular maps of the fracture features. A bandpass filter was applied to retain fractographic features within the $35\pm10°$ band, which were associated with the {111} family of planes. The edge of these features was detected using the methodology outlined in previous sections and compared to the predicted shape from the analytical solution as shown in Figure 3.8.

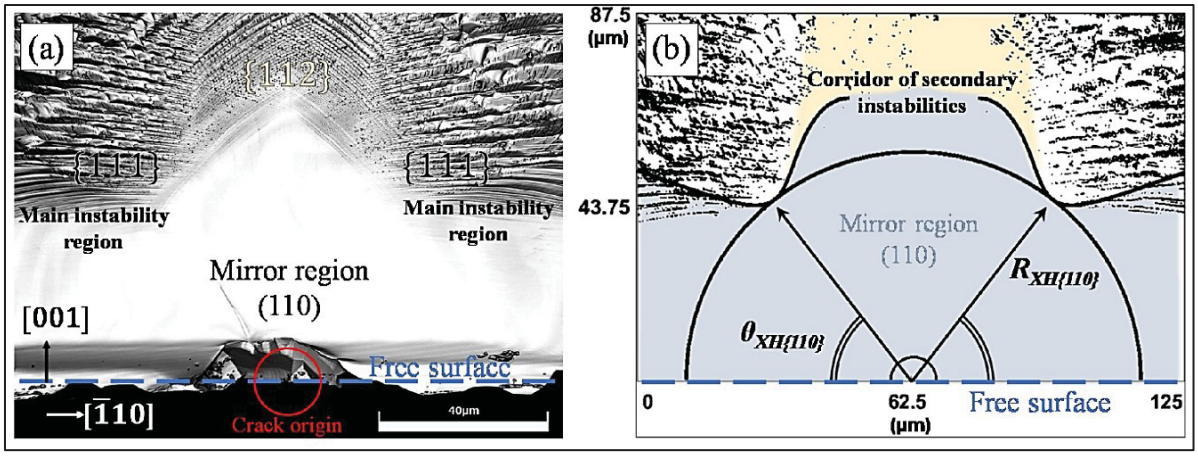

Figure 3.8 Micrography of single crystal silicon fractured at 200MPa (a), and (b)the associated branching region using a surface angles map within a 35±10° band with the predicted shape of the mirror region fitted analytically

Figure 3.8(a) shows an instance of a specimen that broke away from the edge (at 200MPa) and highlights the features formed by different families of planes. Figure 3.8(b) shows an example of how the crystal hackle radius was detected from the sample ($R_{XH\{110\}}$ =51.9μm) and the orientation of the crack-tip at branching ($\theta_{XH\{110\}}$ =52.1°) with respect to the free surface. The predicted shape of the mirror region was obtained by fitting the analytical solution with $\theta_{XH\{110\}}$.

Figure 3.9(a) shows a summary of the normalized strength vs. the inverse square root of the crystal hackle radii, defined as the shortest distance between the fracture origin and fractographic features corresponding to the {111} plane. Normalizing the crystal hackle radius with the sample's thickness allowed comparing experimental data from the present work with measurements obtained by other authors available in the literature (Dugnani & Verghese, 2014; Tsai & Mecholsky, 1992). The mirror-radii reported by Tsai and Mecholsky has been included by taking the average of the radii measured at 40° and 50° to be consistent with the data reported by Dugnani and Verghese.

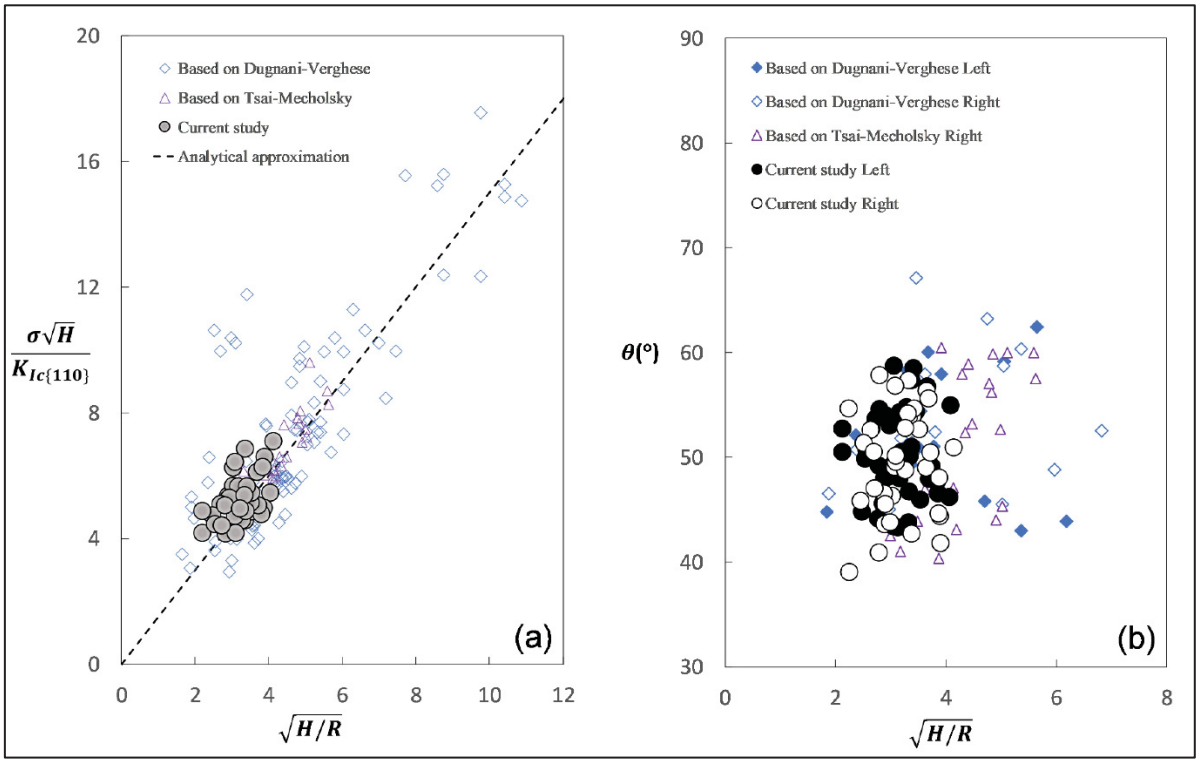

Figure 3.9 (a) Normalized silicon fracture strengths vs. inverse square root of the crystal hackle radii at branching, including the expected analytical trend and (b) branching radii normalized by the thickness vs. crystal-hackle radius orientation with the free surface $\langle\bar{1}10\rangle$

The linear regression of 41 fractured specimens allowed the determination of $A_{XH\{110\}}$=1.47 ±0.24 MPa√m as a scaling parameter for the experimental fracture strengths with an average estimation error of 12% between the experimental strengths and the strengths provided by the analytical regression. The trend obtained in this work was in good agreement with both the experimental data reported by Tsai-Mecholsky (A_m=1.40 MPa√m) and Dugnani and Verghese (A_m=1.39 MPa√m).

Figure 3.9(b) shows the comparisons of the crystal hackle radii angles measured with respect to the free surface for the left and right sides. As expected, there were no obvious differences concerning the detection for each side of the branching confirming that the specimens were correctly oriented with [110] and that the fracture symmetry was preserved. In the current study, the averaged orientation θ_{XH} =*50.3*° was located within 43°<θ_{XH}<57°. Angles based on

Dugnani and Verghese's work were estimated optically on the left and right side of the origin as well (Figure 3.9b). The asymmetry of the onset of branching from Dugnani and Verghese was more significant than found in this work since the average orientation was more dispersed, such as $43° < \theta_{average} = 53° < 67°$. The measurements presented in Tsai and Mecholsky were reported for the right side only (Figure 3.9b). In contrast with Dugnani and Verghese, results from Tsai and Mecholsky were located between $40° < \theta_{average} = 51° < 60°$ and hence were more consistent with the results from this work.

3.4.2 Analytical Model & Wallner Lines

In this work, the analytical formulation describing the crack propagation and the onset of crack-branching was simplified by assuming that the moving crack-front was semi-circular. To confirm the validity of this simplification, the crack sizes in the [110] direction, a, and c in the [001] direction, were estimated, based on Eq.(3.2) assuming steady-state crack-propagation in a uniform stress field. Using $c_R = 4.5$km/s and 5.2km/s on the (110) plane in the [110] direction and [100] direction respectively (Sherman, 2005) and substituting into Eq. (3.2), it was concluded that for a semi-circular, flat crack, $0.98 < a/c < 1.1$ for $0 < V/c_R < 0.85$.

Figure 3.10(a) shows the computed crack-branching boundary predicted based on the analytical model described in the previous sections and the failure criterion outlined by Eq. (3.7). In the same figure, it is also shown an instance of fracture surface from a silicon sample tested in flexure. Branching was predicted to occur first at $R_{XH}/a_0 \approx 2.83$, in the direction $\beta = 64°$. The predicted branching formation corresponded to a value of the crystal hackle constant, $A_{XH} = K_{Ic(110)} \cdot \sqrt{2.83/1.12} \approx 1.35\text{MPa}\sqrt{\text{m}}$. The range of β from fractographic observations ($\beta \approx 50° \pm 10°$) suggests that, in actual fracture surfaces, a/c might differ from the value assumed in this work. Figure 3.10(a) shows an instance of a fracture surface on the {110}-plane with the corresponding branching radius and Wallner lines patterns based on the analytical solution. Although the fractographic pattern was very similar, the minor discrepancies can be explained by the simplifying assumptions used in the analytical calculations. In particular, one of the known effects of crack branching is a reduction in crack velocity, which was not taken into account by the present analytical model. The breaking down

of this assumption can explain why the shape of the mirror boundary and Wallner lines suffered from systematic error when compared to experimental observations; further research into the effect of a change in crack velocity is ongoing.

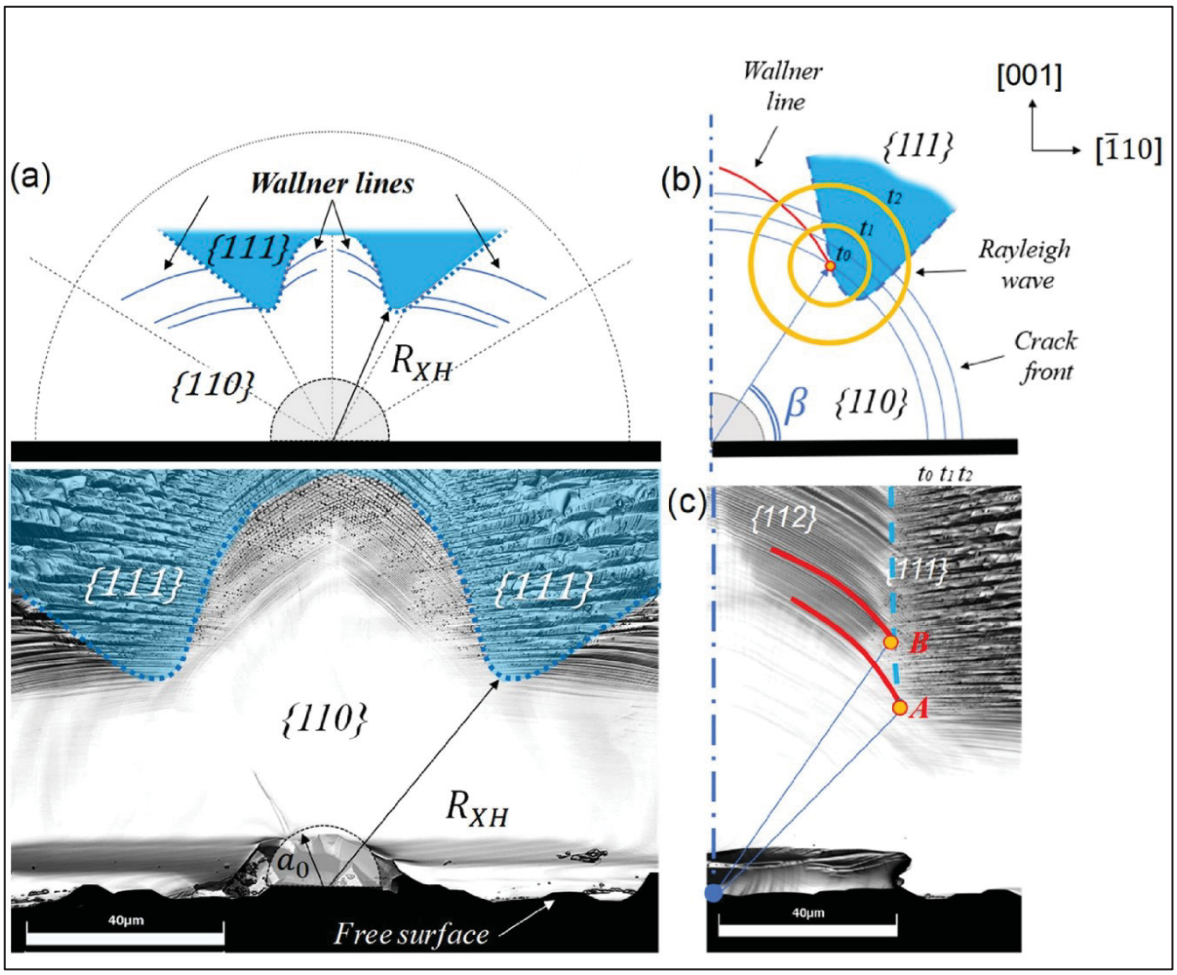

Figure 3.10 (a) Analytical crack branching contour from the {110} to the {111} with actual fracture surface with the corresponding R_{XH} and (b) representation of Wallner line formation and (c) red lines show the predicted location of the Wallner lines starting at crack-branching points A and B on a tested sample's fracture surface (lower right)

As the crack locally branched from the (110) to the {111} planes, acoustic waves were triggered at branching points. These acoustic waves interacted with the crack-front propagating on the (110) plane, with temporary excursion out-of-plane, forming rib-shaped surface markings, i.e. the Wallner lines. In this section, the location of Wallner lines on the (110) plane

was estimated based on the geometry and loading considered. For a given crack branching location (e.g. points A and B in Figure 3.10(c)), the Wallner line formation was predicted by the intersecting points for the propagating acoustic wave-front and the crack-front on the (110) plane (Figure 3.10(b)). For a given crack-direction β, the acoustic wave speed, i.e. Rayleigh speed c_R and the crack speed V were taken based on Sherman's reported values (Sherman, 2005) (V/c_R between 0.28 and 0.38 for the branching locations considered). An instance of two Wallner lines, as predicted in this analysis near the symmetry plane, is shown in Figure 3.10(c).

3.5 Discussion

3.5.1 Dynamic Crack-Tip Instabilities

Both sharp hackles or {111} "prism-like" features and features formed by cracks propagating on the {112} planes, were found to bound the mirror-region, in good agreement with the literature (Ben-Bashat Bergman & Sherman, 2019; Sherman, 2006, 2009; Sherman, Markovitz, & Barkai, 2008c). The {111} hackles formed during crack propagation (as illustrated in Figure 3.1) have not been used in the past for quantitative fractography, although, as discussed in Sherman and others (Kaufman & Forty, 1986; Kermode et al., 2008; Sherman & Be'ery, 2004; Sherman et al., 2008c), they were consistently observed and they might be useful in estimating mechanical and/or physical properties of crystals. We rectify this missed opportunity (as detailed in Figure 3.3 and Figure 3.4) by leveraging fractographic features to calculate the fracture strength. The use of surface angle maps rather than feature-heights conventionally used, helps to better discriminate between relevant fractographic regions (as illustrated in Figure 3.5). This approach is based on the fact that the fracture surface of single crystal silicon comprises features formed on different crystallographic planes (see Figure 3.6), and we show that only {111} is induced by dynamic instabilities (as described in Figure 3.7 and Figure 3.8). We confirm that the {112} features are 'secondary features', resulting from the interaction between acoustic waves and the crack-front, similar to Wallner lines in amorphous materials. Although it has been shown by Dugnani and Verghese (Dugnani & Verghese, 2014) that secondary features at the 'cusp' did correlate with the fracture strength of the sample, secondary markings are likely less reliable as they can be susceptible to

unpredictable factors including reflected acoustic waves from sample surfaces and defects. Additionally, we observe that Wallner lines at the 'cusp' are not always present, for example as shown in Figure 3.7, hence any method relying on this feature cannot be reliably implemented.

Figure 3.9(b) shows a plot of the crystal hackle radius orientation with respect to the free surface $\langle \bar{1}10 \rangle$, $\theta_{XH\{110\}}$ vs. $(H/R)^{1/2}$. No significant angular variations were noted between the left and right sides of the mirror boundaries, which suggests not only that the crack developed symmetrically regardless of the initial flaw shape, but also those dynamic instabilities were triggered at well-defined values of the stress intensity factor. This observation can also be inferred from the symmetric appearance of all fracture surfaces measured, for instance, in Figure 3.10. In this work, the crystal direction where the first crack branching occurred was measured in 41 specimens and estimated at $\theta_{XH\{110\}} = 50.3 \pm 3.58°$. Notably, the observed first branching angle was very consistent in the range $2 < (H/R)^{1/2} < 7$. This observation is important, as the critical fracture strength on the {110} planes was thought to depend on the crack propagation direction, hence significant variations in $\theta_{XH\{110\}}$ would naturally imply that variations in A_{XH} should also be expected. The effect of $(H/R)^{½} > 2$ on $\theta_{XH\{110\}}$ could not be directly observed in the sample sizes considered in this work.

3.5.2 Crack-Branching Model

We considered the behavior of fast-moving circular cracks in an anisotropic material, single crystal silicon. The crack-branching criterion used was the maximum-hoop stress. The fracture toughness on the {111} planes was assumed uniform (i.e. $K_{Ic\{111\}} = 0.82$ MPa√m), while on the {110} planes, it depended on the crack propagation direction. Assuming $K_{Ic\{110\}} =$ 0.90MPa√m, the predicted crystal hackle constant corresponding to crack-branching from the (110) to the {111} planes, was estimated as $A_{XH} = 1.35$MPa√m. The relative uncertainty on the experimental $A_{XH\{110\}}$ was calculated following the law of the propagation of variance through the corresponding quadratic sum of each of the relative uncertainties of its associated variables (i.e. the strength and $R_{XH\{110\}}$). The experimental crystal hackle radius was $A_{XH\{110\}} = 1.47 \pm 0.24$

MPa√m and provided nearly the same scaling (i.e. the same crystal hackle constant) as the value computed analytically. The marginally smaller magnitude predicted by the analytical model can be explained in part by the model simplifications, the uncertainties associated with the fracture strength of the material, and by the fact that crack-branching might be occurring at smaller crystal hackle radii than reported by the experiments but undetected due to the small feature size relative to the incident radiation wavelength (UV and visible light). Experimental support to this last explanation was provided by Cramer's description of fractures on the silicon {110}-plane (Cramer, Wanner, & Gumbsch, 2000). Cramer reported that at relatively high crack speeds, {111} features formed on the fracture surface but appeared 'mirror-like' by optical microscopy.

The experimental and analytical crystal hackle constants obtained in this work are in good agreement with the reported experimental values from Dugnani and Verghese, i.e A_m = 1.54MPa√m. Dugnani and Verghese's higher magnitude for the mirror constant, A_m, can be attributed to the fact that R_m was measured at fixed angles, hence its magnitude was always larger or equal to the values obtained through the methodology described in this work. The values reported by Tsai-Mecholsky seemed to be the most consistent with A_m = 1.39MPa√m (from 24 samples). Tsai-Mecholsky's trend consistency can be explained by the fact that the surface defects were also consistent in size and shape, as they were introduced artificially by indentation. The symmetric and nearly circular sizes of the indented flaws resulted in more consistent initial crack shapes compared to the naturally occurring defects considered in the present work.

The analytical description of the mirror region matched the experimentally observed boundaries obtained with the procedure developed in this study (Figure 3.8). The differences between the analytical and experimental shape of the mirror boundary can be attributed mostly to the simplifications in the analytical solution which, for instance, assumes the crack remains circular both before and after branching. The analytical solution can also predict the formation of secondary features, including Wallner lines. The formation of these secondary features was correctly predicted. However, one of the known effects of crack branching is a reduction in crack velocity, which was not taken into account by the present analytical model and is an avenue for future study. In particular, the "cusp" predicted by the analytical model was in a

region where the crack-tip velocity and shape were no longer uniform, and hence beyond the applicability range of the analytical solution. The breaking down of the model's assumptions can explain why the shape of the mirror boundary and Wallner lines in Figure 3.10b) and c) were reliable, yet suffered from systematic error when compared to experimental observations. In addition, our analytical model employs dynamic stress field calculations based on continuum fracture mechanics. At very small length scales (smaller than 2-3nm), the discrete, atomistic nature of matter limits the applicability of this assumption (Shimada et al., 2015). Nevertheless, molecular dynamics simulations have shown that continuum mechanics can account for the vast majority of the total free strain energy in the body (Buehler & Gao, 2006). The release of this strain energy is the driving force for crack propagation, and although the use of continuum mechanics is therefore justified, this may partially explain the minor systematic error observed. The model predictions are nonetheless extremely useful, as they correctly predict the formation of secondary features and help explain why such secondary features cannot be relied upon when estimating the strength of fractured samples.

3.6 Conclusions

In this work, a novel framework for the fractographic analysis of silicon fracture on the (110) plane was introduced. Unlike previous work, this method identifies specific cleavage planes associated with dynamic instabilities, thereby accounting for the intrinsic anisotropy of single crystal silicon. Both confocal optical microscopy and atomic force microscopy were used to characterize, using 3D surface profilometry, relevant cleavage planes associated with all important fractographic features.

Surface angle maps were computed from 3D surface profilometries, thereby identifying the crystallographic planes when first crack branching occurs. An analytical dynamic fracture model was also developed and used to establish which cleavage plane best correlates with the fracture strength. With the aid of the analytical model, it was determined that features corresponding to the {112} planes were Wallner lines, and hence they were not relevant when estimating the strength. The shortest length between crack origin and the detected {111} cluster of points at crack branching delineate the mirror-boundary; these radii were subsequently

correlated with experimental strengths to extract the experimental crystal hackle constant $A_{XH\{110\}} = 1.47 \pm 0.24 \text{MPa}\sqrt{\text{m}}$.

The scaling, branching planes, and fractographic patterns predicted by the analytical model are consistent with the experimental findings, and correctly predict that the {111} planes bound the mirror region, whereas the {112} planes are associated with Wallner lines. Furthermore, the analytically computed crystal hackle constant was found to be within 8% of the experimental observation. These important findings improve our understanding of the fracture in single crystal silicon and help elucidate mechanical and thermomechanical failure modes in semiconductor devices. In particular, the consequence is that the lithographic patterning and manufacture of semiconductor devices should take into account the mechanical anisotropy of crystallographic orientations to improve fracture toughness and thereby prolong service life and enhance reliability.

CHAPTER 4

FRACTURE SURFACE ANALYSIS AND QUANTITATIVE CHARACTERIZATION OF GALLIUM ARSENIDE III-V SEMICONDUCTORS USING FRACTOGRAPHY

Anthony Moulins[a], Roberto Dugnani[b] and Ricardo J Zednik[a]

[a]Department of Mechanical Engineering, École de Technologie Supérieure,
1100 Notre-Dame West, Montreal, Quebec, Canada H3C 1K3
[b]UM-Shanghai Jiao Tong University – Joint Institute, Shanghai, China

Paper published in *Engineering Failure Analysis (EFA)*, February 2021

4.1 Abstract

Gallium arsenide is used in the most demanding semiconductor applications, including the medical, aerospace, and communication industries, where significant mechanical stresses are experienced during operation. Mechanical stresses from thermal expansion and mechanical loading can result in the fracture of GaAs crystals, a leading cause of semiconductor device failure. Unfortunately, the underlying fracture mechanisms in GaAs III-V semiconductors are currently not well understood. In this manuscript, we present a quantitative approach to identify the main GaAs fractographic features and correlate these to a crystal's original mechanical fracture strength. In addition, detailed fractographic analysis was used to estimate the crystal hackle constant (analogous to the mirror constant in isotropic media), $A_{XH}^{\langle 221 \rangle}_{\{110\}}$= 1.58 MPa√m on the {110} cleavage plane of GaAs. Finally, crystal stereography and analytical geometry were used to confirm that the fractographic features correspond to the intrinsic symmetries of single crystal GaAs.

Keywords: fractography, failure analysis, single crystal, gallium arsenide, mirror constant, crystal hackle, stereography

4.2 Introduction

GaAs exhibits superior semiconducting properties compared to silicon and germanium, including higher charge carrier mobility, a direct band-gap transition, and improved power and high-frequency response (Blakemore, 1987; Hjort, Soderkvist, et al., 1994). GaAs is therefore particularly useful in advanced optoelectronic and photonic devices, as well as in ultra-high frequency and microwave applications. GaAs displays excellent resistance to radiation and thermal degradation, making it valuable for space applications and super-efficient photovoltaic cells (Green, Emery, Hishikawa, Warta, & Dunlop, 2015; Konagai, Sugimoto, & Takahashi, 1978). However, mechanical stresses during processing and operation can lead to catastrophic brittle fracture of GaAs crystals, a significant cause of semiconductor device failure (Dushkina, 2015). Analyzing the fracture surface of a failed device or structure is a standard approach commonly used in failure analysis in order to identify the root cause (Ma, Moulins, & Dugnani, 2021; Moulins, Dugnani, & Zednik, 2021; Quinn, 2007; Sherman, 2009). Unfortunately, the mechanisms by which single crystals fracture, or crack, including GaAs, are poorly understood.

Basic fractographic concepts for single crystals began to be developed in the 1940s (R. W. Rice, 1974; Shetty, Bansal, Rosenfield, & Duckworth, 1980; Tsai & Mecholsky, 1992; Zapffe & Worden, 1949a, 1949c, 1949b). Margevicius and Gumbsch (Margevicius & Gumbsch, 1998) studied the behavior of GaAs fractures, and observed that as GaAs cleaved on {100} and {111} planes, the crack eventually deflected onto {110} planes, but provided no explanation. Okui et al. (Okui, Hasegawa, Fukutome, & Nakashima, 2000) studied GaAs cleavage by scanning tunneling microscopy and revealed that, in contrast with [110] cleavage, cleaving toward [112] and [114] resulted in flat (110) terraces. In addition, many elongated “island-like” structures and high step densities were detected, however, they were “largely fluctuating” in the scans and the authors were not able to correlate them with any particular crystallographic directions. Sauthoff et al. (Sauthoff et al., 1999) separated the fracture surface of GaAs into six regions of interest, each with characteristic morphologies. Although each

morphology was associated with a distinct crack front velocity, the authors did not formerly correlate these findings with the intrinsic anisotropy of the crystal and the loading direction. When performing the fractographic analysis of isotropic brittle materials, such as glasses or fine-grained ceramics, the distance between the origin and the mirror-mist boundary is correlated to the strength of the material by a phenomenological expression first formalized by Orr (Orr, 1972) :

$$\sigma_f = A_m / \sqrt{R_m} \tag{4.1}$$

where σ_f is the strength, R_m is the mirror radius, and A_m is the empirically obtained, material-dependent mirror constant (ASTM, 2010b). Macroscopically, in glasses and fine ceramics, the onset of crack growth instabilities delineates the mirror-mist boundary or the mist-hackle boundary regions (Dugnani & Zednik, 2013; Quinn, 2007, 2016). For single crystals, the crack-front first propagates on a characteristic mirror-like plane i.e. weakest cleavage plane, but once the crack-tip reaches a critical, characteristic speed along a specific crystallographic direction, micro-branching occurs (Moulins, Ma, Dugnani, & Zednik, 2020; Sherman, 2009; Sherman, Markovitz, & Barkai, 2008a; Stewart & Bradt, 1980; Tsai & Mecholsky, 1992). In the past, various authors attempted to apply variations of Orr's equation to single crystals but did not formally provide any "standardized" methodology on how and where to measure the mirror radius (Griffith, 1921; J. Mecholsky et al., 1978; J. J. Mecholsky et al., 1976; Orr, 1972; Tsai & Mecholsky, 1991, 1992). Not surprisingly, A_m was found to depend on the crystalline plane considered, the loading direction, and the observation technique used, such as, for instance, in single crystal silicon (Dugnani & Verghese, 2014). Nonetheless, no study has been conducted to formally establish a relationship between fractographic features and the strength of GaAs before this work.

In this manuscript, we, therefore, develop a fractographic approach to establish the mechanical fracture strength of GaAs based on characteristic fractographic features. To remain consistent with the literature, we use the same definition of fracture strength used by Orr (Orr, 1972). This fracture strength is the stress required for a crack to propagate catastrophically through a crystal; as fracture initiates at natural flaws that are present in any crystal, we would expect a

Weibull-type relationship between strength and specimen size; to eliminate this effect, all tested samples had the same geometry and dimension.

The manuscript begins by describing the experimental setup used to fracture GaAs single crystals before proceeding to discuss, in detail, the fracture surfaces obtained. The fractographic features discussed are important to generalize Orr's relation for isotropic media to single crystal GaAs. This work accounts for the crystal orientation and uses fractographic analysis to determine the crystal hackle constant, $A_{XH}{}^{\langle 221\rangle}_{\{110\}}$ on the $\{110\}$ cleavage plane and measured along the $\langle 221\rangle$ directions, analogous to the mirror constant in isotropic media.

4.3 Methodology

This section provides details on the characterization techniques and proposes a quantitative fractographic approach to establish the relationship between the fracture surface's fractographic features and the crystal strength of GaAs.

4.3.1 Uniaxial Flexural Tests

Undoped GaAs wafers (nominal 3-inch diameter) with one side mirror-polished and a thickness h = 619 ± 19 μm were cleaved along the (110) plane. Uniaxial flexural overloading was performed on 25 specimens by three-point bending tests (3PBTs) according to the ASTM C1161 standard (ASTM, 2013) as presented in Figure 4.1.

The test specimens corresponded to the ASTM C1161 size and geometry requirements, and were rectangular bars with widths b = 8 ± 2 mm and useful test length l = 41 ± 10 mm. The 3PBTs were conducted on an MTS system with a 50N load cell (resolution 0.01 N) and roller diameter 10 mm. Test specimens were loaded using displacement control at a fixed speed of 0.5 mm/min. The cracks were initiated at natural flaws on the mirror-polished side to avoid any strong flaw misorientation. The fracture strength σ_f reported throughout the manuscript corresponds to the experimentally measured stress imposed by the 3PBT at which fracture

occurred. Small deflection and linear elastic response during experiments justify the use of linear elastic beam theory to calculate the stress at failure.

According to ASTM C1161, the flexural stress at failure is therefore given by

$$\sigma_f = 3Pl / 2bh^2, \tag{4.2}$$

where *P* is the fracture force.

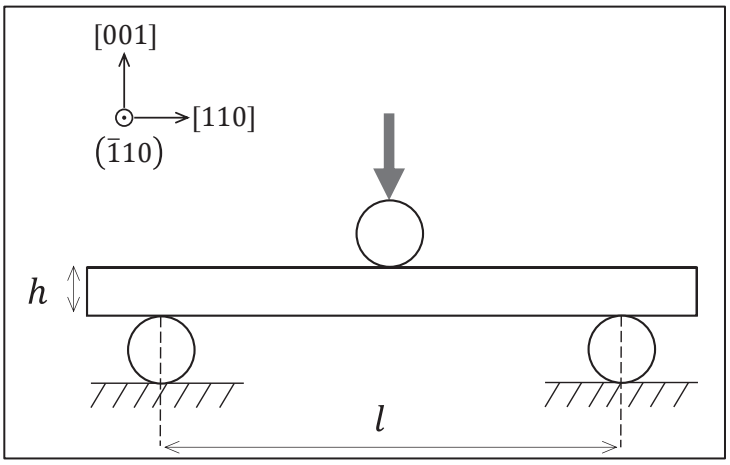

Figure 4.1 Schematic of the experimental three-point bending test (3PBT) setup showing GaAs crystal [110] orientation. The polished surface is on the bottom (tension) side

4.3.2 3D Surface Characterization

An Olympus LEXT OLS4100 confocal microscope was used to identify fractographic characteristics with the help of Matlab (*MATLAB version 9.6.0.1174912 (R2019a) Update 5*, 2019) to extract and analyze post-mortem fracture surfaces. Fracture surface 2D micrographs and 3D maps were obtained with bright field illumination and through a non-polarized, 405 nm ultraviolet laser source, resulting in a nominal 10 nm height resolution and 120 nm lateral resolution.

4.3.3 Crack Growth Analysis

As GaAs fractures in an anisotropic manner, the crystal's hackle radius could be influenced by any misalignment of the load with respect to [110]. To identify such misalignment, the sample orientation must be carefully established to ensure perpendicularity of the mirror plane with the optical/confocal microscope axis. The following standardized algorithm was used as the basis of a concise standardized failure analysis procedure when characterizing single crystal GaAs fracture surfaces:

- Confocal optical micrographs near the fracture origin are collected with each fracture surface oriented with the free surface parallel to $\langle \bar{1}10 \rangle$. As the mirror region near the origin is generally not perfectly aligned with the optical axis, i.e. aligned with [110], the region near the origin is leveled by fitting a plane to the flat mirror region and rotating the mirror to align with [110].

- The location of the crack's origin locus is visually confirmed by back-tracing the source of the "quasi-static" step-like features, as described in the next section.

- The radii at branching are measured optically using semi-circular arcs centered at the crack's origin and tangent to the first occurring branching ridges. Underestimation of the hackle radius could be introduced due to limitations in the resolution of the measuring equipment. Fractographers need to ensure that the incident radiation wavelength is sufficient to detect features with adequate resolution and should be capable of interpreting relevant fractographic markings. In this work, the crack-tip paths were tracked with 10 nm height resolution and 120 nm lateral resolution. Methodology to confirm the hackle radius based on the height of the steps or ridges is explained in later sections.

- The distance between the crack origin and first crack-branching steps or ridges are used to define the crystal hackle (or mirror) radii. For specimens that broke both 'at the edge' and 'away from the edge', $R_{XH\{110\}}$ was measured along $\langle 2\bar{2}1 \rangle$.

- The crystal hackle constant $A_{XH}{}^{\langle 221\rangle}_{\{110\}}$ is obtained correlating the strength with the reciprocal square root of the crystal hackle radii on (110) towards $\langle 2\bar{2}1\rangle$.

- The hackle directions, φ_i, are estimated optically on the sample with respect to $[1\bar{1}0]$ at the free surface, as shown in Figure 4.6(a). The local crack-tip branching deflection angles, θ_B, with respect to the (110) mirror plane normal vector can be computed from laser profilometry (LP) with a 3D UV-laser confocal microscope, as shown in Figure 4.7 and Figure 4.8. The theoretical values for φ_i and θ_B can be computed using trigonometry from the planes for any desired crystal. Crystal stereography can then be used to help confirm that the indexed planes and axes were satisfying the intrinsic crystal symmetries of GaAs.

4.4 Results

4.4.1 Misalignment of Mechanical Load

All of the GaAs specimens initially fractured on {110} planes by a cleavage-step mechanism systematically forming a "flat" mirror region. 'Step-like' features fracturing along the (110) planes were observed fanning directly from the fracture origin as, for instance, shown in Figure 4.2.

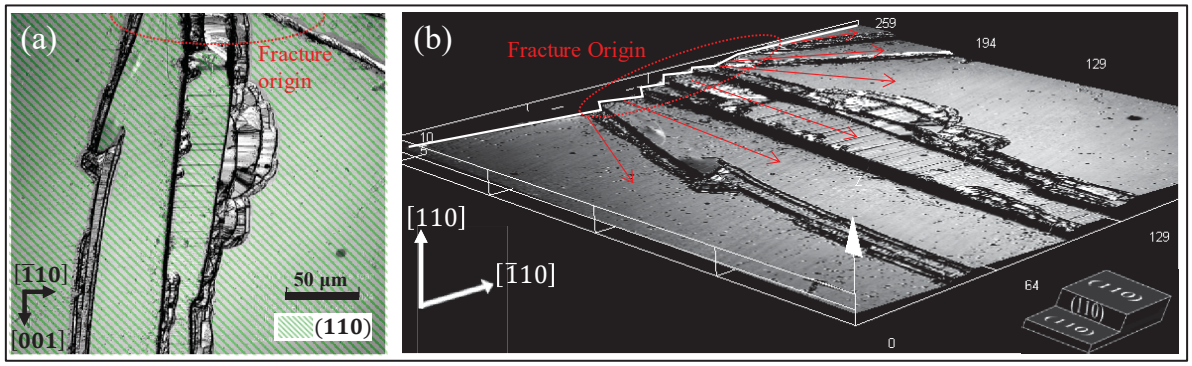

Figure 4.2 (a) 2D Confocal micrograph of a representative (110) GaAs stepped fracture surface and (b) 3D micrograph of same fracture surface showing misalignment between the main cleavage plane (110) and the fracture origin

For the case shown in Figure 4.2, the stepped fracture surface was introduced by the misalignment between the main cleavage plane (110) and the crack origin, which essentially provided multiple crack initiation seeds for the crack to propagate on parallel {110} planes. Another instance of GaAs's step-deflection mechanism on a different sample is shown in Figure 4.3, where cracks propagate with a small misalignment, α_1, with respect to the loading direction.

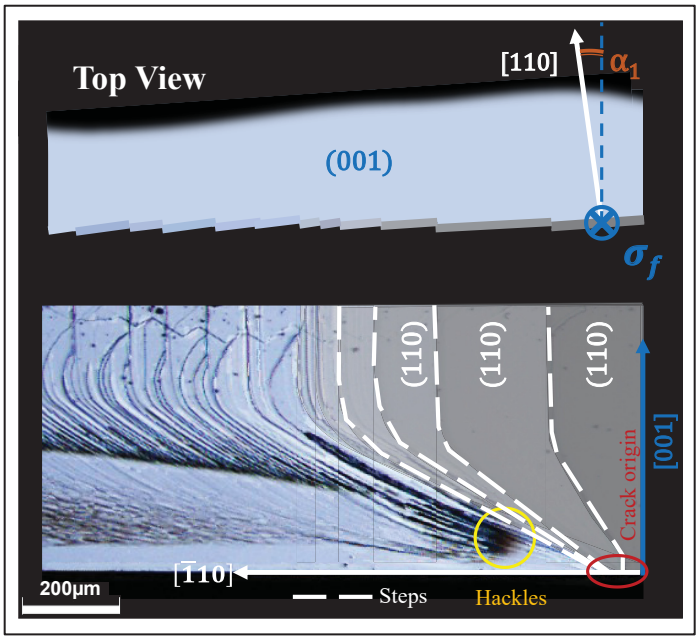

Figure 4.3 Terrace-like steps (or ridges) due to small misalignment between the loading direction and the cleavage plane

These features remained on the plane of the crack and did not seem to contribute significantly to the macroscopic change in the crack propagation direction. Terrace-like steps fan directly from the fracture origin to compensate for the α_1 misalignment between [110] and the loading direction [001].

4.4.2 Hackle Branching

In order to enable a quantitative analysis of fracture surfaces, the "hackle branching" feature was identified as an important fractographic feature. This allows us to define a "crystal hackle

radius" R_{XH} (for a given crystallographic direction) in single crystal GaAs that is analogous to the "mirror radius" R_m normally used to study the fracture of isotropic materials. Additional hackle features out of the (110) mirror plane were found fanning away from the crack origin delineating "wing-like" branching regions. Figure 4.4(a) and Figure 4.4(b) show instances of fractures with the origin "away from the edge" and with the fracture origin "at the edge"; as expected, no significant fractographic differences were noted between the two cases. Figure 4.4(a) and Figure 4.4(b) show representative fracture surfaces where a high-density of hackle lines are present away from the crack origin. Steps are running toward the upper right (compressive) side of the specimen from the crack origin, almost perpendicular to the propagating crack-front (dashed line).

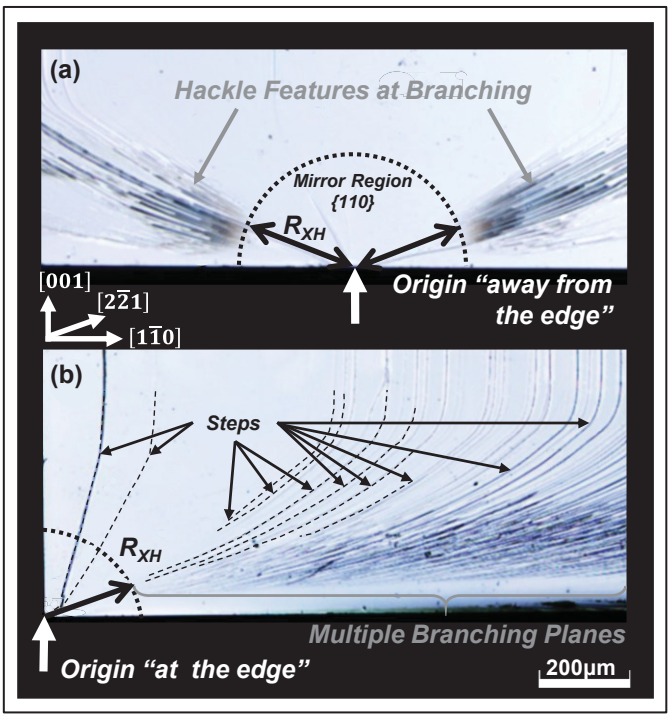

Figure 4.4 (a) Representative fracture surfaces of GaAs with origin away from the edge (σ_f=95±5MPa), and (b) at the edge (σ_f=148±8MPa)

The flat fracture surface in Figure 4.4 was associated with the principal (110) cleavage plane surrounding the crack origin and is known as the mirror region. The fracture strength σ_f corresponds to the experimentally measured stress at fracture. Various (110) 'step-like

features' were observed fanning out from the fracture origin and were associated the maximum tensile stress not being perfectly aligned with the (110) cleavage plane.

For the fracture surfaces observed across all samples, two distinct sets of hackle lines with the same fractographic pattern were systematically produced. In Figure 4.5, the 3D surface profilometry of a representative specimen obtained near the beginning of hackles (i.e. the onset of branching at the mirror-hackle boundary) is shown. Figure 4.5 shows how the crack branches away from the (110) mirror plane with hackles oriented mostly towards $\langle\bar{2}21\rangle$. For the sample shown in the Figure 4.5, $R_{XH\{110\}}$ ~151 µm and σ_f = 83 ± 6 MPa. Shorter hackles (delimited by the dashed line) alternate with the larger hackles. The beginning of the crack branching was characterized by sharp hackles visible at the microscale, thus delineating a transition between a nearly flat mirror region and the hackle features.

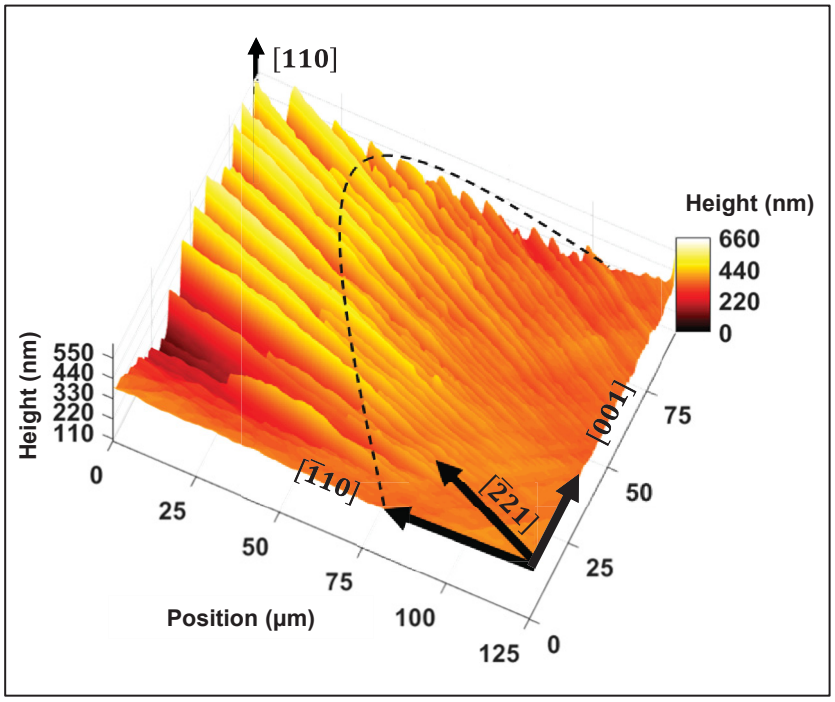

Figure 4.5 Representative fracture surface of GaAs at branching (σ_f=83±6MPa)

The hackle directions with respect to $[\bar{1}10]$ at the free surface, φ_i, were estimated optically on the sample as shown in Figure 4.6(a).

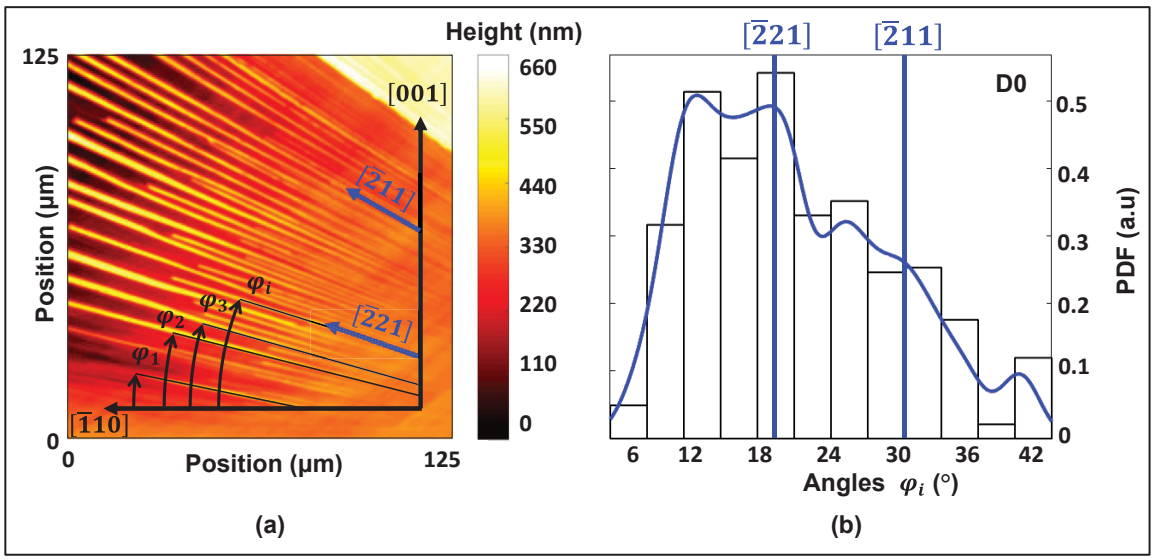

Figure 4.6 (a) Representative micrograph of GaAs fracture surface near the onset of crack branching and (b) probability density function of the GaAs feature's directions with respect to $[\bar{1}10]$ (same sample as shown in Figure 4.5)

Figure 4.6(b), shows an example of the Kernel density estimator (KDE) for the hackle directions (blue envelope). The KDE is a smoothing function that establishes the shape of the curve based on the probability density function. The bin sizes (column widths) were selected from Scott's rule i.e. asymptotically minimizing the integrated mean squared error. The distribution of hackles within branching is mostly attributed to $\langle\bar{2}21\rangle$, although hackles were found within $\varphi_{min} = 6° < \varphi_i < 42° = \varphi_{max}$.

For hackles oriented within the interval φ_{min} and φ_{max}, the crack-front shape remains perpendicular to the branching features (i.e. nearly circular with respect to the crack origin), as shown in Figure 4.7. Profile P1 was obtained at radius R1 ≈ $2R_{XH\{110\}}$ (i.e. ~ 302 μm) from the crack origin. The height (i.e. the hackle's height or amplitude) was approximately $\delta_1 \approx 472$ nm and the "contour" triangular and elongated. For profile P2 (at R2 ≈ $1.7R_{XH\{110\}}$), the hackle height was approximately $\delta_2 \approx 280$ nm and for profile P3 (at R3 ≈ $1.4R_{XH\{110\}}$), the hackle height was approximately $\delta_3 \approx 138$ nm.

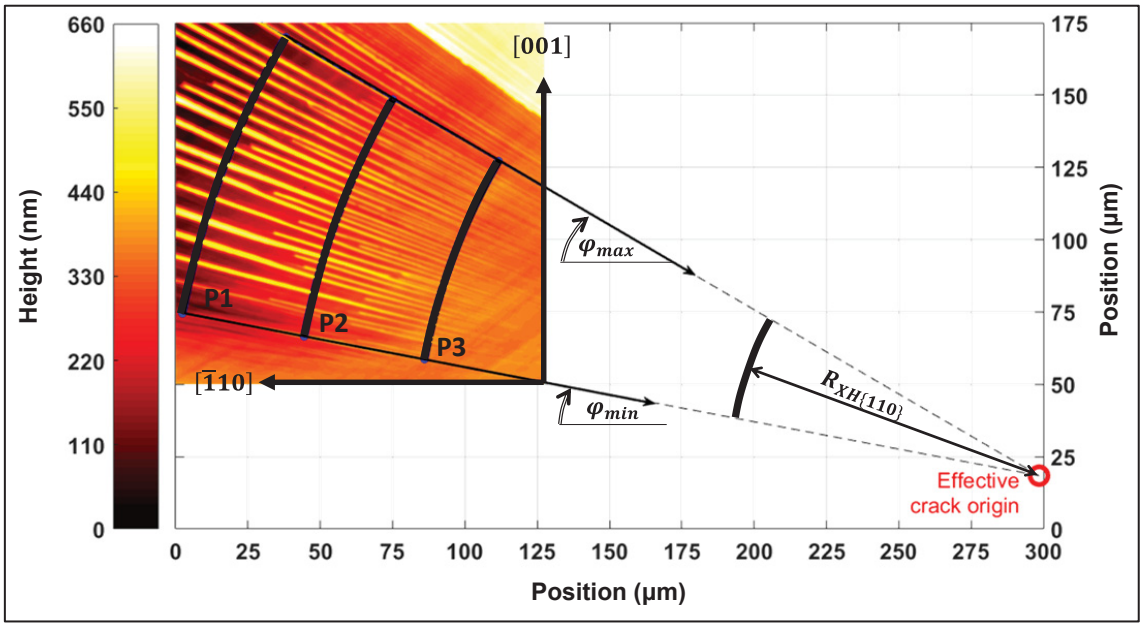

Figure 4.7 Identification of the crack front profiles P1 ≈ $2R_{XH\{110\}}$, P2 ≈ $1.7R_{XH\{110\}}$ and P3 ≈ $1.4R_{XH\{110\}}$ for $R_{XH\{110\}}$=151μm and the effective crack origin locus (same sample as shown in Figure 4.5 and Figure 4.6)

The hackle heights (Pi) from P1, P2, and P3 have been normalized by radial distances R1, R2 and R3, respectively to obtain Figure 4.8(a). Figure 4.8(b) shows the distributions D1, D2, and D3 of the angles θ_B obtained from P1, P2 and P3. The hackles' orientations were computed directly from 3D LP with respect to [110]. Figure 4.8(a) shows that the density of peaks from P1 to P3 decreases as the distance between the crack-origin and the crack-front increases, and the most prominent hackles at P1 appear to correspond to the {111} planes and {454} planes which are very close to each other ~2.7º. Large branching features with low density were apparent (P1) as the crack propagated farther from the crack origin, whereas small and narrowed branching features with higher density were present (P3) in the early crack branching process.

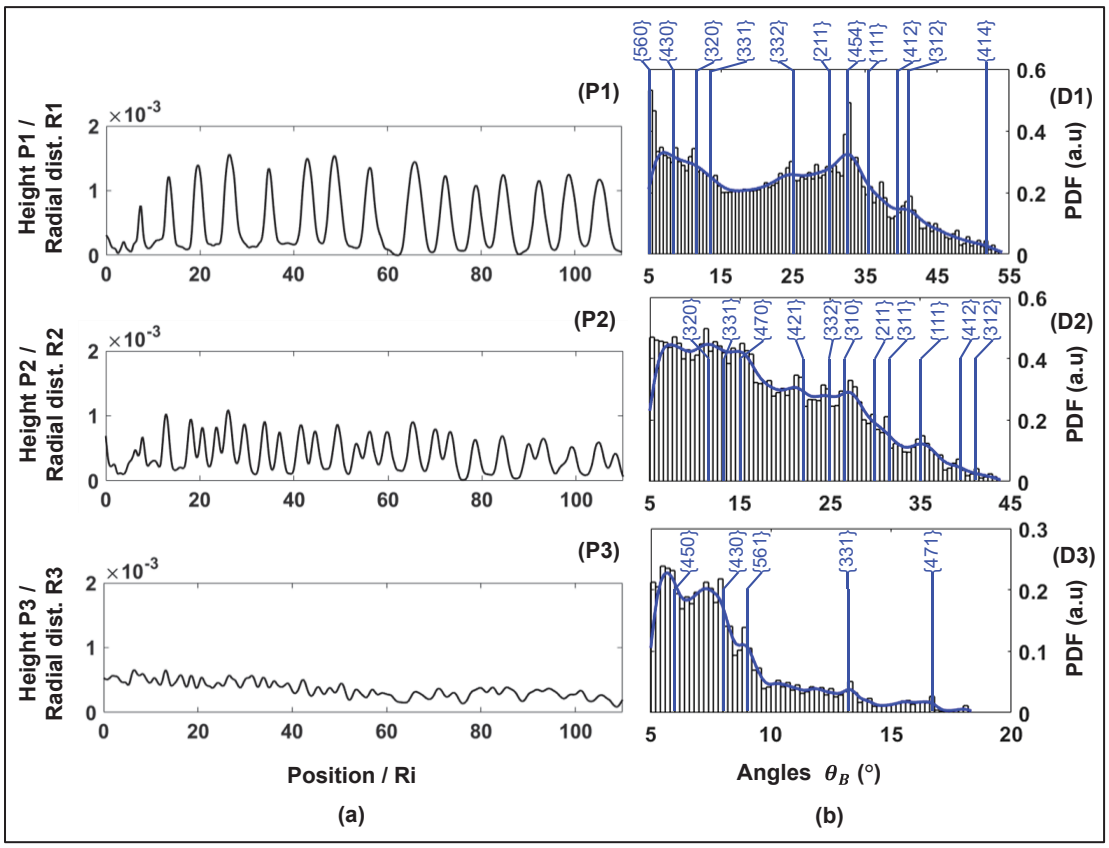

Figure 4.8 (a) Normalized height profilometry (P1, P2 and P3) with radial crack-lengths R1, R2, R3 and (b) resulting distributions (D1, D2 and D3) of GaAs surface angles

The profile P1 shows a periodicity in the ridges with an average lateral distance between peaks of $\overline{\Delta_{PEAK}}(P1)\sim$ 1644 nm with an angle between peaks of $\zeta_1 \sim 0.31^{\circ}$ with respect to the crack's origin. This angle was calculated using the law of cosines (Al-Kashi theorem):

$$\zeta_i = \cos^{-1}\left(\frac{2Ri^2 - \left(\overline{\Delta_{PEAK}}(Pi)\right)^2}{2Ri^2}\right) \tag{4.3}$$

The distribution D1 shows that the range of the facet orientations is between 5-55°. P2 shows a slightly less recurring surface profile in Figure 4.8(b). The distribution D2 shows that the range of the orientations of the facet is between 5-45°. The average lateral distance between each peak in P2 is $\overline{\Delta_{PEAK}}(P2)\sim$ 936 nm with an angle between peaks of $\zeta_2 \sim 0.21^{\circ}$. Furthermore, LP highlighted a tortuous crack path at the onset of the crack branching in the

region of P3 where locally, a high density of ridges (i.e. hackle features) were present. However, P3 does not seem to follow any regular cracking sequence and most probably the feature size could not be easily detected because of the optical limitations imposed by the incident radiation wavelength (i.e. 405nm). The corresponding distribution D3 shows that the range of the facets' orientations is between 5-19°. Although local maxima of D3 are relatively close to each other, D3 indicates that there are traces of the crack-tip deflecting out of (110) with a relatively high density of the Kernel estimator. The average lateral distance between each peak in P3 is $\overline{\Delta_{PEAK}}(P3)\sim$ 677 nm with an angle between peaks of $\zeta_3 \sim 0.18^{o}$.

4.4.3 Deflection Planes Correlate with the Crack's Zone Axis

Stereographic projections of GaAs were used to identify the crystal directions of fractographic features observed on all samples. For this analysis, the relevant cracking sequence along with P1 corresponding to angular surface distribution D1 was selected. D1, therefore, corresponds to the angular surface distribution relative to the mirror direction $[110]$ and D0 corresponds to the angular surface distribution relative to the free edge direction$[\bar{1}10]$. Figure 4.9(a) shows the crystallographic directions of experimentally observed crack deflection planes at branching that lie within 5-55° from (110), such as {331}, {231}, {221}, {241}, {130}, {131}, {121}, {111}, {142}, {132}. Great circles corresponding to these crystallographic directions are shown in Figure 4.9(b)-(c)-(d)-(e). The intersection of each of these great circle traces with the main (110) trace provides the effective crystallographic direction indices (i.e. effective zone axis) of the crystal hackle radius at branching.

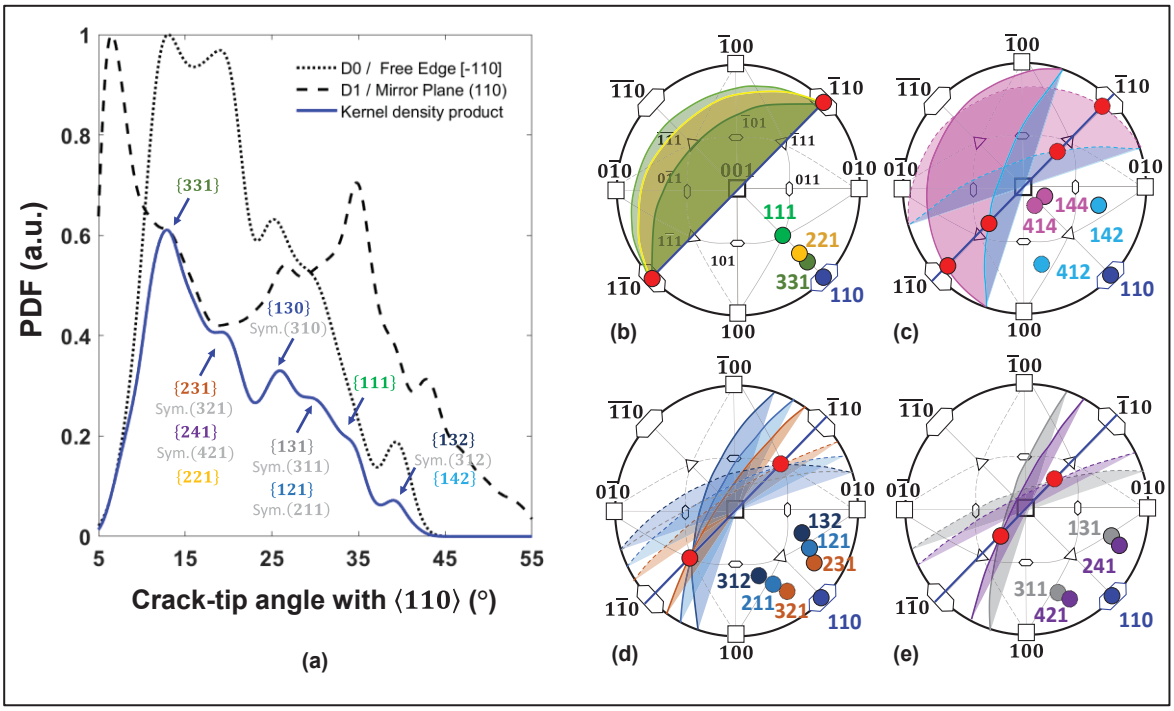

Figure 4.9 (a) Experimentally observed Probability Density Function of crack-tip branching angles relative to (110) as observed in all tested samples, and (b)-(c)-(d)-(e) stereographic projections with directions and traces of the fracture planes in GaAs single crystal

In order for the experimentally observed deflection planes at branching to be consistent with GaAs crystal symmetry and the experimental hackle radius directions, the Weiss zone law must be satisfied (Edington, 1975; Hammond, 2015; Whittaker, 1981). As shown in Figure 4.9, we indeed confirm that the deflection planes which were in the zone axis followed Weiss zone law, and by extension were also in the same family of planes containing the indices of the effective crystallographic directions of $R_{XH\{110\}}$. The crack cleavage planes were formed from five groups of zone axes (i.e. hackle directions) as shown in Figure 4.9(b)-(c)-(d)-(e), the red dots represent the intersection of the trace of (110) (straight blue line) with the traces of the deflecting planes (solid-colored arcs). The dashed arcs represent the great circles and each intersecting point indices can be obtained by superimposing a full (001) stereogram(Hammond, 2015). For example, Figure 4.9(b) shows that the {111}, {221}, and {331} traces intersect the (110) trace at $[1\bar{1}0]$ and the $(\bar{1}\bar{1}0)$ trace at $[\bar{1}10]$. This confirms that

{111}, {221} and {331} intersect {110} at a direction parallel to the free surface and rotate toward the [001] to align with the macroscopic principal stress. Figure 4.9(c) shows that {144} and {142} intersect (110) at $[4\bar{4}3]$ and $[2\bar{2}3]$, respectively, consistent with the crystal symmetry. Figure 4.9(d) shows that {132}, {121} and {231} intersect (110) at $[1\bar{1}1]$ and $[\bar{1}11]$, respectively. Figure 4.9(e) shows that {131} and {241} intersect (110) at $[1\bar{1}2]$ and $[\bar{1}1\bar{2}]$, respectively. In summary, the experimental observations are consistent with the crystal symmetry of GaAs.

4.4.4 Hackle Radius versus Mechanical Strength

Figure 4.10 shows the stress at failure σ_f as a function of the crystal hackle radius; this stress corresponds to the experimental stress imposed by the 3PBT at the point of failure. The value of the stress was determined from the mechanical load imposed by the 3PBT set-up at the time of catastrophic fracture as calculated according to the ASTM C1161 standard (ASTM, 2013). The uncertainties were estimated using a statistical propagation of uncertainty approach using the variance of individual measurements. As shown in Figure 4.4, mirror radii were estimated optically and were mostly oriented towards $\langle\bar{2}21\rangle$ (~19.5° away from the $\langle\bar{1}10\rangle$). Using Equation (4.1), the GaAs "crystal hackle constant" was therefore estimated as $A_{XH}{}^{\langle 221\rangle}_{(110)}$=1.58 MPa√m; this parameter is analogous to the "mirror constant" used in isotropic materials. No obvious differences were observed between the origins 'at the edge' vs. 'away from the edge', although the data appeared to be more consistent for cracks that originated away from the edge. The apparent absence of a correlation between the origin location and fracture strength suggests that the sample edges are smooth with relatively few defects.

We therefore find that Orr's relation (Equation (4.1)) can be generalized to single crystal GaAs, were the parameters are defined in reference to the crystallographic directions that dominate the fracture mechanism:

$$\sigma_f = A_{XH}{}^{\langle 221\rangle}_{(110)} / \sqrt{R_{XH\{110\}}} \qquad (4.4)$$

where σ_f is the fracture strength, $R_{XH\{110\}}$ is the crystal hackle radius, and $A_{XH}^{\langle 221\rangle}_{(110)}$ is the crystal hackle constant.

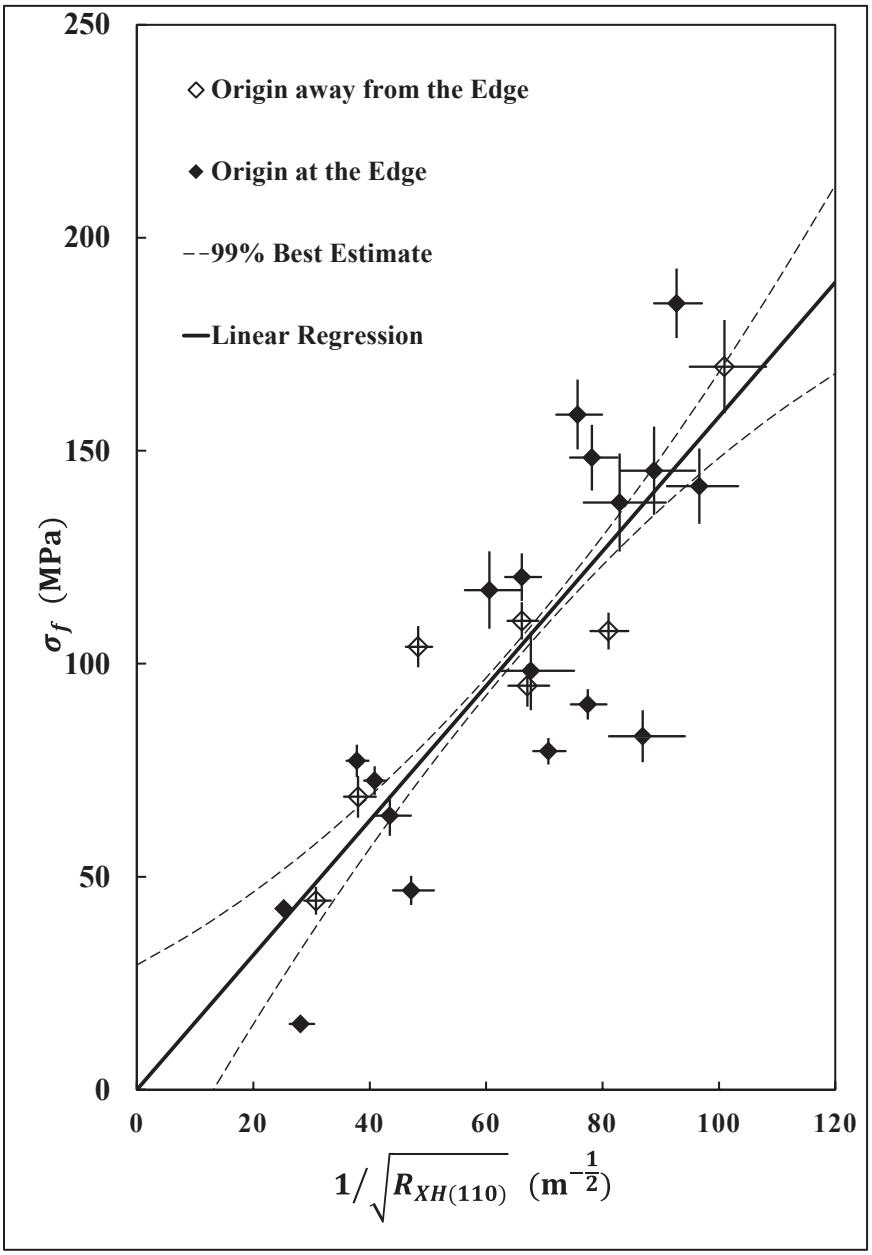

Figure 4.10 Relationship between fracture strength and the crystal hackle radius for the main (110) GaAs fracture mirror (data for all tested samples). R^2=0.71 for the linear regression

Radial lengths associated with the 'mirror-branching' boundary correctly predicted the fracture strength within 19% from the measured values. From a practical perspective, where the lateral resolution of the instruments used to detect the mirror-hackle boundary was not sufficient, the hackle height could be measured at least at 2 different radial locations and then used to extrapolate the hackle constant, as shown for a representative sample in Figure 4.11.

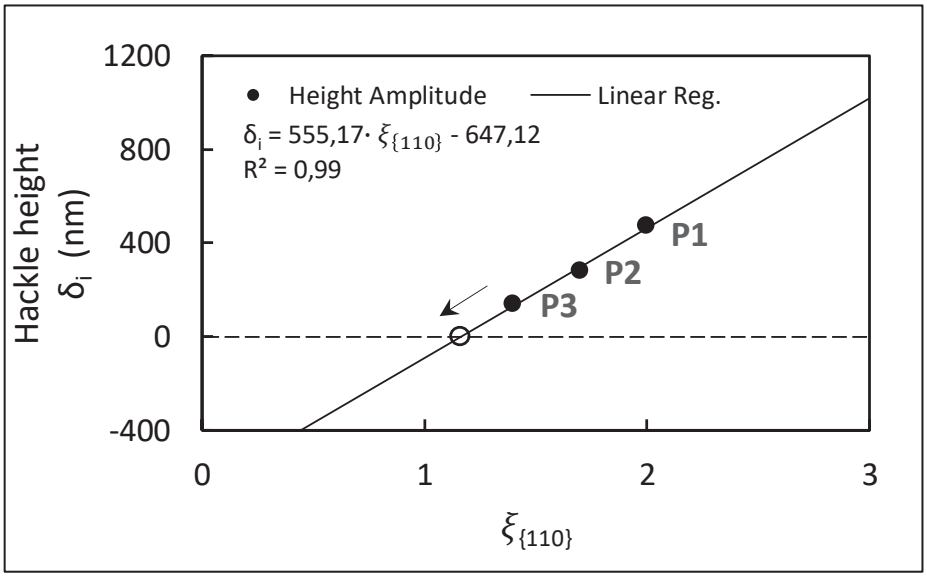

Figure 4.11 Relationship between hackle height featured at branching and normalized radial distance-to-crystal hackle radius ($\xi_{\{110\}} \equiv R_i/R_{XH\{110\}}$) for the main (110) GaAs fracture ($R_{XH\{110\}}$=151μm, σ_f=83±6MPa)

For the representative example in Figure 4.11, the normalized radial length, $\xi_{\{110\}}$, and correspondent hackle's height available at P1, P2, and P3, were used to estimate the hackle radius ($R_{XH\{110\}}$=151μm) and a discrepancy of 16% was incurred between this method and the directly measured hackle radius.

4.5 Discussion

Experimental evidence shows that it is not necessary to distinguish between 'edge crack origins' and 'origins away from the edge' when generalizing Orr's relation to single crystal GaAs. This occurs because we include crystallographic references when defining the crystal

hackle radius R_{XH} and crystal hackle constant A_{XH} that are analogous to the mirror radius and mirror constant in isotropic media.

From the experimental quantitative analysis, two sets of fractographic features were consistently recognizable, since they formed on different planes following the methodology and recommendations outlined in this study. For instance, while the first quasi-static set of GaAs terraces was due to the misalignment, the GaAs wing-like features at branching were due to dynamic crack growth effects where radial distances at critical branching scaled with the strengths.

4.5.1 GaAs Step-like Terraces

For quasi-static loading in brittle materials, the fracture surface is usually created in a direction orthogonal to the maximum tensile stress. In fact, steps initiate at the crack origin, depending on the flaw orientation or the cleavage plane alignment with the loadings. GaAs {110} steps occur when the principal stress was not perfectly aligned with the cleavage plane or when there were any other misalignments with the initial flaw. In this study, the GaAs steps occurred along the (110) planes, consistent with it being the weakest plane as reported in the literature (Hirsch, Pirouz, Roberts, & Warren, 1985; Levade & Vanderschaeve, 1999; Margevicius & Gumbsch, 1998; Ning, Perezt, & Pirouz, 1995; Pouvreau et al., 2013; Wang & Pirouz, 2007; Wasmer et al., 2013). Figure 4.2 and Figure 4.3 showed that the GaAs (110) steps fan out from the origin where the crack velocity is nearly zero, which indicates that their formation is not related to dynamic effects. A similar mechanism has been reported for silicon single crystal because of a small misalignment of the main cleavage plane (Sherman, 2003). Kermode et al. (Kermode et al., 2008) reported on a complex ‘multi-scale’ phenomenon in silicon single crystals whereby very low-speed crack propagation occurs on the (110) plane (i.e. after cracks decelerate). Cleavage steps are caused by the crack propagating on very close parallel planes and it is usually one or more single lines, parallel to the local direction of crack propagation (Quinn, 2016). They are running radially towards the surface in compression and are not

materially affected by the crack-front dynamics. Although the fractographic features associated with misalignments were not used to estimate the samples' strength, they were helpful in locating the fracture origins.

4.5.2 Dynamic Crack Branching

Once the crack-tip reaches a critical speed, the crack-tip branches on more energetically favorable cleavage planes. The crack evolves according to the crystal anisotropy and the crack-tip speed, thereby minimizing the energy involved in the fracture process. GaAs hackle marks consistently form at a distance inversely proportional to the stress squared (see Eq. (4.1) and Figure 4.10) in the direction $\langle 2\bar{2}1 \rangle$. The fractography of GaAs surfaces suggested that combinations of small prisms-like features were created as an energy dissipation mechanism and were not due to random defects or misalignment, as they systematically mark the surface for a range of $\varphi_i \in [6°; 42°]$ with respect to the free surface.

As the crack-front becomes dynamically unstable, it branches away from the {110} planes toward particular families of planes, including {331}, {231}, {221}, {241}, {130}, {131}, {121}, {111}, {142}, {132}. Large hackles consolidate on those planes that minimize the system's energy during propagation, thus explaining why the {111} crack-tip deflection family of planes is shown to dominate for the GaAs single crystal (e.g. D1 shows mostly {111} in Figure 4.7 and Figure 4.8). This observation is consistent with the understanding that the fracture toughness on the (111) plane, $K_{1c(111)}$ = 0.39 MPa√m, and on the (110) plane, $K_{1c(110)}$ = 0.46 MPa√m, have similar magnitudes (Michot et al., 1988; Yasutake et al., 1988); a crack can therefore easily switch between the (110) and {111} planes upon obtaining enough kinetic energy (Michot et al., 1988; Sherman et al., 2008a; Yasutake et al., 1988).

Moreover, surface profilometry of the features formed after branching reveal that the hackle height approximately scales with the distance from the branching location. Assuming that the crack velocity does not change considerably after first branching for a given direction, then it could be inferred that the hackle height scales linearly with the crack's energy release rate. In this work, stereography and analytical geometry helped confirm that both φ_i and θ_B were

consistent with the (001) stereograms found in the literature (Whittaker, 1981): both planes and axis zones followed the Weiss rule for a range of crack-branching radius directions (Figure 4.9). Features on planes other than (110) cannot be associated with misalignment or defects, since the fractographic features consistently start at a distance inversely proportional to the stress squared for nearly the same $\langle 2\bar{2}1 \rangle$ hackle radius directions with respect to the free surface (Figure 4.10). These are in good agreement with another reported surface instability previously reported in GaAs ("fork-shaped" sinking (Xu et al., 2019)) and analogous to "V-shape markings" in single crystal silicon (Ben-Bashat Bergman & Sherman, 2019; Sherman, 2009).

4.6 Conclusion

This manuscript provides a systematic approach to estimate the strength of fractured GaAs single crystals by generalizing Orr's relation for isotropic media to single crystals. Standard fractographic methods typically employed in homogeneous, isotropic materials were adapted to study anisotropic, single crystal GaAs fractured by uniaxial loading. "Terrace-like" step features were identified and explained as a quasi-static mechanism with which the crack-front re-aligns with the direction orthogonal to the maximum tensile stress (i.e., cleavage plane misaligned with loading). These step-like features were also used to locate the effective crack origin. A new characteristic parameter, the "crystal hackle radius" R_{XH} (analogous to the "mirror radius" in isotropic materials) was defined as the distance from the origin to the "mirror-branching" boundary which coincided with the macroscopic {111} deflection of the crack-front predominantly aligned with $\langle 2\bar{2}1 \rangle$. This framework extends Orr's empirical relation for isotropic media to GaAs single crystals and establishes the correspondent "crystal hackle constant" $A_{XH}{}^{\langle 221 \rangle}_{(110)}$= 1.58 MPa√m to estimate the strength (analogous to the "mirror constant" in isotropic materials). It was noted that hackles form at distinct values of the energy release rate. Microscopic investigation reveals that the mirror-branching corresponds to specific, well-defined planes formed as the dynamically unstable crack-front deviates from the initial {110} plane. Hackle lines were found to be explained by combinations of well-defined crystallographic planes. The hackles initially correspond to many different planes but

ultimately consolidate mostly along the {111} family of planes as the crack develops. The crystallographic families of planes along which crack growth was observed follows the Weiss zone law, as illustrated using stereographic projections.

CHAPTER 5

CHARACTERIZING THE ANISOTROPIC FRACTURE ENERGY AND TOUGHNESS OF GALLIUM ARSENIDE SINGLE CRYSTALS USING VICKERS INDENTATION

Anthony Moulins[a] , Roberto Dugnani[b] and Ricardo J Zednik[a]

[a]Department of Mechanical Engineering, École de Technologie Supérieure,
1100 Notre-Dame West, Montreal, Quebec, Canada H3C 1K3
[b]UM-Shanghai Jiao Tong University – Joint Institute, Shanghai, China

Paper submitted to *International Journal of Fracture*, June 2021

5.1 Abstract

Although gallium arsenide (GaAs) is a technologically important semiconductor material, the mechanical behavior of GaAs single crystals (e.g., wafers) is poorly understood. The present manuscript discusses how the common Vickers indentation technique can be used to characterize the anisotropic fracture energy and toughness of GaAs single crystals. This approach uses the measured lengths of surface cracks introduced in GaAs wafers by Vickers indentation to determine the fracture energy and toughness corresponding to various crystal planes. Careful fractographic inspection indicates that when the main [110] crystal zone axis was aligned with the indenter's diagonal, the fractures predominantly propagated along the {110} and {100} planes. Fractures on additional planes were only observed when the indenter was not aligned with the principal axes. The normalized fracture toughness was estimated from indentation parameters and used to evaluate the directional fracture energy on the {001} plane. The directional fracture energy experimentally obtained was consistent with the theoretical estimates based on the number of broken bonds.

Keywords: fracture energy, toughness, Vickers indentation, gallium arsenide, anisotropy, energy release rate.

5.2 Introduction

In the electronic and optoelectronic industries, III-V semiconductors such as gallium arsenide (GaAs) are often regarded as having superior semiconducting properties compared to silicon (Si)(Blakemore, 1982; Hjort, Soderkvist, et al., 1994). GaAs single crystals are therefore increasingly used as the active material in the microwave and high-speed circuits. Although the electronic properties of GaAs are well studied, the mechanical properties are poorly understood. This limited understanding of mechanical behavior results in mechanical fracture as being an important mechanism of real-world GaAs device failure. The mechanical anisotropy inherent to single crystals is a further complication to characterizing GaAs fracture energy and toughness(Gilman, 1959; Margevicius & Gumbsch, 1998; Sauthoff et al., 1999; Wasmer, Ballif, Pouvreau, Schulz, & Michler, 2008; Yasutake et al., 1988).

GaAs has a simple zincblende crystal structure ($F\bar{4}3m$) and exhibits slip systems similar to face-centered cubic (FCC) crystals(Hjort, Soderkvist, et al., 1994). However, GaAs displays a deviation from inversion symmetry resulting in fracture toughening of the $\{111\}$ cleavage planes, with the consequence that $\{110\}$ act as primary cleavage planes (Margevicius & Gumbsch, 1998; Moulins et al., 2021)

The literature is rich with linear elastic fracture mechanics (LEFM) models that describe the fracture energy and toughness of linear, elastic, isotropic materials. Although some authors have employed indentation fracture mechanics to estimate the fracture toughness of select anisotropic materials in the past, these estimates adapt LEFM approaches that homogenize the material behavior, thereby glossing over the anisotropy. Unfortunately, these models should not be readily applied to anisotropic materials, such as GaAs single crystals: no single accepted standard method currently exists to evaluate the directional fracture energy and toughness in anisotropic single crystals. Therefore, the literature reports a wide range of fracture energy and toughness values for GaAs, with particular uncertainty in the cleavage plane and crack propagation directions. Table 5.1 shows a summary of the fracture energy and toughness reported in the literature using the convention "$(plane)/\langle propagation\ direction\rangle$", whenever available.

Table 5.1 A summary of reported fracture energy Γ and toughness K_{1c} in single crystal GaAs

REFERENCE	REPORTED METHOD	Γ (Jm^{-2})	K_{1c} (MPa $m^{-0.5}$)
WASMER ET AL.(WASMER ET AL., 2005) (2005)	NS : $K_{1c} = 1.12 \cdot \sigma_c\sqrt{\pi d}$ $2\gamma_s = K_{IC}/E$	**0.69** (110)/⟨*unknown*⟩	**0.41** (110)/⟨*unknown*⟩
MARGEVICIOUS AND GUMBSCH(MARGEVICIUS & GUMBSCH, 1998) (1998)	IBF: $K_c = \sigma_f\,(M_b/Q^{1/2})\,a^{1/2}$	N/A	**0.43** (110)/⟨001⟩, ⟨112⟩ **0.46** (110)/⟨111⟩
MARGEVICIOUS AND GUMBSCH(MARGEVICIUS & GUMBSCH, 1998) (1998)	IBF: $K_c = \eta(E/HV)^{1/8}\left(\sigma_f {P_i}^{1/3}\right)^{3/4}$	N/A	**0.49** (110)/⟨001⟩, ⟨112⟩ **0.53** (110)/⟨111⟩
MICHOT ET AL.(MICHOT ET AL., 1988) (1988)	DCB: $K_I = P \cdot f(a/w)\,/\,B\sqrt{w}$ $2\gamma = ((1-\nu^2)/E){K_{IC}}^2$	**0.76** {110}/⟨*unknown*⟩	**0.4** {110}/⟨*unknown*⟩
YATSUTAKE ET AL.(YASUTAKE ET AL., 1988) (1988)	IBF: $K_c = \sigma_f M_b\left(\sqrt{a/Q}\right)^{1/2}$	N/A	**0.46** {110}/⟨*unknown*⟩
HJORT ET AL.(HJORT, ERICSON, SCHWEITZ, HALLIN, & JANZÉN, 1994) (1994)	VI: $K_{Ic}^{(0)} =$ $k_1(c - a/a)^{-1/2}(E/HV)^{2/3}\left(P/c^{3/2}\right)$	N/A	**0.44** {110}/⟨110⟩
CHEN AND MORRISSEY(CHEN & MORRISSEY, 1984) (1987)	IBF: $K_{IC} = \sigma M_B(\pi a/Q)^{1/2}$	N/A	**0.43** {100}/⟨*unknown*⟩ **0.31** {110}/⟨*unknown*⟩ **0.45** {111}/⟨*unknown*⟩
MESSMER AND BILELLO(MESSMER & BILELLO, 1981) (1981)	SD: $\sigma_f = (2E_{hkl}\cdot\gamma_c\{hkl\}/(1-\nu^2)\pi c)^{1/2}$	**0.86** {110}/⟨*unknown*⟩	N/A
CAHN ET HANNEMAN(CAHN & HANNEMAN, 1964) (1964)	$\bar{\mathrm{F}} = \Delta H_s/\left(\sqrt{3\mathrm{N}_a a^2}\right)$	**2.2** (100)/⟨*unknown*⟩ **1.5** (110)/⟨*unknown*⟩ **1.3** (111)/⟨*unknown*⟩	N/A

NS: Nano Scratching
IBF: Indentation Beam Fracture
DCB: Double Cantilever Beam
VI: Vickers Indentation
SD: Spark Discharge Machining

Of all the methods used in the literature to study mechanical properties of materials, hardness indentation methods (such as Vickers) are among the fastest, easiest, and most economical to employ.

Vickers indentation provides “controlled flaws” and implies irreversible deformation and crack nucleation along with a complex singular stress field(Evans & Charles, 1976; Lawn & Wilshaw, 1975; J. H. Lee, Gao, Johanns, & Pharr, 2012). Lawn et al.(Lawn, Evans, & Marshall, 1980) refined Evans and Charles’ correlation(Evans & Charles, 1976) and derived a critical stress intensity factor (SIF) expression based on a ‘’composite’’ elastoplastic indentation crack model. In this model, the reversible character of the elastic contribution to the SIF was neglected as significant crack propagation was observed during unloading(Lawn, 1993; Lawn et al., 1980). The elastic-plastic contribution to the SIF was included by superimposing the contact stress field to the residual stress field(J. H. Lee et al., 2012). Equilibrium arguments eventually lead to Lawn et al.’s formulation for the critical SIF (i.e., the LEM model)(Anstis, Chantikul, Lawn, & Marshall, 1981a, 1981b; Lawn et al., 1980; Lawn & Wilshaw, 1975) which is expressed as:

$$K_{1c} = \frac{P_{\max}}{b^{3/2}} \prod \left(\frac{H_V}{E}, \frac{b}{a}, \psi, \nu \right) \tag{5.1}$$

where b and a are the total median crack length and the half diagonal of the indenter impression, ν is the homogenized Poisson’s ratio, ψ is the half axis-to-face angle of the pyramidal indenter ($\psi \approx 68°$ for a Vickers indenter), H_V is the Vickers hardness of the material, and E is the homogenized elastic Young’s modulus. Figure 5.1 (a) shows the schematic view of typical half-penny median cracks *M1*, *M3*, *M5* and *M7* and the lateral, secondary cracks *L2*, *L4*, *L6* and *L8*.

The LEM model’s imprecise description of the complex elastoplastic contact stress field makes it not applicable to all indenter geometries and not suitable for anisotropic materials. The inapplicability of the formulation to anisotropic materials stems from the fact that predictions are based on Hill’s elastic/plastic internal cavity analysis(Hill, 1998). The

implication of Hill's approximation involved homogenizing E and ν hence ignoring local anisotropic effects.

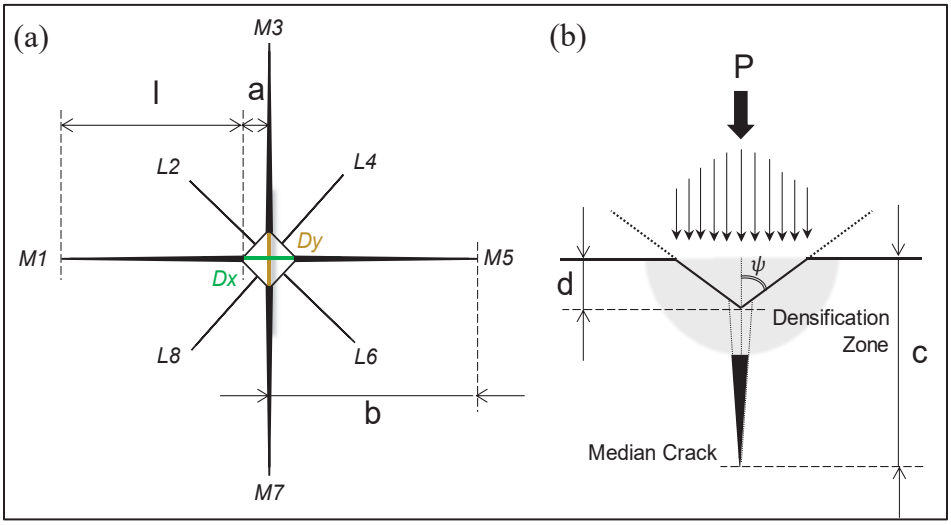

Figure 5.1 Schematic view of (a) the top of the resulting Vickers impression with radial, median cracks M1-M3-M5-M7 and short, lateral cracks L2-L4-L6-L8 for (b) an elastic sharp contact pressure distribution P~P_max.

The work of Anstis et al.(Anstis et al., 1981a) showed that $P\max/b^{3/2}$ in Eq. (5.1) was approximatively constant in both sapphire and silicon single crystals, brittle polycrystal ceramics, and ceramic glasses over a working range of load 0.1-10N. This model correctly anticipated the final median/half penny crack configuration(Lawn, 1993; Lawn et al., 1980; Niihara, 1983) but a comprehensive analysis of the evolution of the crack shape was not developed. The accuracy and significance of inconsistent methods used in the literature to estimate the fracture energy and toughness in GaAs (Table 5.1) are still subject of debate(Blakemore, 1982; Michot et al., 1988; Roberts, Warren, & Hirsch, 1986; Yasutake et al., 1988). In particular, the homogenization of material properties neglects the material's crystallographic features.

In the present study, we propose to resolve this inconsistency by combining indentation and fractography to quantify the crystalline anisotropy for single crystal GaAs. We induced controlled cracks by Vickers indentation and measured the crack lengths and directions by

confocal microscopy. The crack parameters were studied at ambient temperature with the [110] GaAs specimen zone axis oriented at $0 < \theta < 360°$ compared to the indenter axis. A specimen rotation of $0 < \theta < 50°$ helped generate cracks whose crystallographic directions were indexed with respect to [110]. The normalized (001) directional fracture toughness was related to both the experimental indentation parameters and the fracture energy. Finally, the theoretical fracture energy was evaluated considering the anisotropy of material properties using the calculation of a broken bond and compared with the experimental results.

5.3 Methodology

Currently, no accepted standard exists to evaluate the fracture energy and toughness of single crystals by indentation. This section, therefore, describes the testing equipment and analytical approach used to characterize the directional fracture energy and toughness in GaAs by Vickers indentation. Indentation parameters such as the crack length, the imprint size, and the measured hardness have been used to resolve the (001) in-plane fracture energy and toughness. The experimental fracture energy was evaluated using a modified LEM model in plane strain with an equivalent elastic Young's modulus, and the results compared to the approximate fracture energy estimated based on the number of broken bonds.

5.3.1 Materials and Testing Apparatus

Undoped (001), 625 ± 20 μm thick, GaAs wafers (resistivity below 0.001Ω.m) with one side mirror polished were used for Vickers indentation. Each wafer was pre-cleaved along [110] as shown in Figure 5.2 (a) to produce samples that could be fitted onto the Vickers indentation support. Short GaAs crystals approximately 40x30mm were indented onto the (001) mirror-polished plane to generate cracks around the imprint as shown in Figure 5.2 (b).

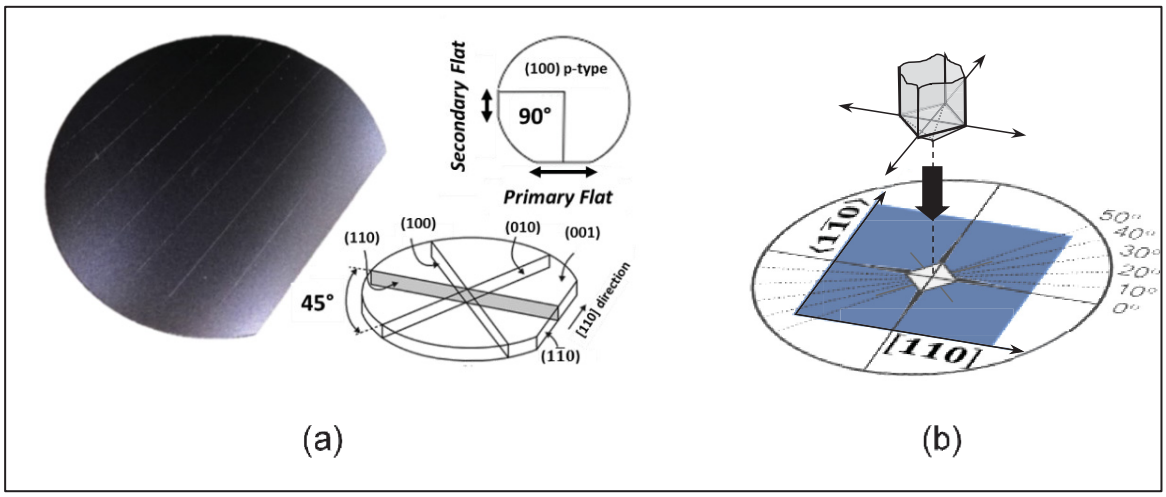

Figure 5.2 Schematic illustration of (a) (001) GaAs single crystal wafer showing the [110] crystallographic zone axis, and (b) GaAs sample (blue) with [110] parallel to the indenter diagonal.

An automated microhardness Clemex tester with a Vickers indenter and contact pressure ranging from 1 to 1000 gf was used in the experiments. The procedure used in this work was based both on the standard test methods for Vickers indentation hardness of advanced ceramics(ASTM, 2019) (ASTM C1327) and the standard test method for micro-indentation hardness of materials(ASTM, 2017) (ASTM E384). A 500-gf load with 10-seconds dwell time was used to generate "long" median, corner cracks at the indentations, as shown in Figure 5.1 and Figure 5.2 (b). The imprint parameters were analyzed using an integrated Clemex optical microscope under bright-field illumination with the automatic detection function for the hardness evaluation. Ten to fifteen indentations were generated for each orientation between $0 < \theta < 50°$, with the 0° orientation aligned with [110] and parallel to the indenter's axis (Figure 5.2 (b)). Conservatively, indentations were spaced apart by about eight times the total crack length, b, to avoid stress field disturbances or interference between indentations. Only long cracks with $b/a > 2.5$ (see Figure 5.1 M1-M3-M5-M7) located at the indentation corners were considered as corresponding to the worst loading scenario. A 3D laser confocal microscope (OLS4100, Olympus) was used to measure the crack lengths and orientations under a 405 nm incident wavelength monochromatic light. The material parameters of the fractured (hkl) planes were calculated from these measurements as outlined below.

5.3.2 Directional Young's Modulus (Elastic Stiffness)

For any $\langle hkl \rangle$ crystallographic zone axis, the GaAs effective directional Young's modulus (elastic stiffness) orthogonal to the crack propagation direction was calculated inside the $\{hkl\}$ crystallographic plane based on Wachtman(Wachtman, 1974), Kelly and Macmillan(Kelly & Macmillan, 1986):

$$1/E_{\{hkl\}}^{\langle uvw \rangle} = S_{11} - 2\,(S_{11} - S_{12} - 0.5S_{66})(m^2n^2 + n^2p^2 + m^2p^2) \tag{5.2}$$

where m, n and p are the direction cosines of the angle between the crystallographic direction $\langle uvw \rangle$ and the $\langle 001 \rangle$ cubic crystal's zone axis. S_{ij} are the elastic coefficients from the 6x6 cubic compliance matrix(Brozel & Stillman, 1996) with magnitudes $S_{11} = 11.7 \cdot 10^{-12} Pa^{-1}$, $S_{12} = -3.7 \cdot 10^{-12}\ Pa^{-1}$ and $S_{66} = 16.8 \cdot 10^{-12}\ Pa^{-1}$. For an orthotropic crystal relatively prismatic and slender whose principal axis [100], [010] and [001] are aligned with a reference axes XYZ, the reduced compliance coefficients in the Voigt(Hjort, Soderkvist, et al., 1994; Margevicius & Gumbsch, 1998) form can be expressed as a function of the product of strain ratios(Nemeth, 2011). The strain ratios between two orthogonal crystallographic directions α and β was obtained for any crystallographic $\{hkl\}$ reference family of plane and directions(Brantley, 1973; Nemeth, 2011):

$$\nu_{\{hkl\}}^{\alpha\beta} = -\frac{S_{12} + (S_{11} - S_{12} - 0.5S_{66})\,(m_\alpha^2 m_\beta^2 + n_\alpha^2 n_\beta^2 + p_\alpha^2 p_\beta^2)}{S_{11} - 2(S_{11} - S_{12} - 0.5S_{66})\,(m_\alpha^2 n_\alpha^2 + n_\alpha^2 p_\alpha^2 + m_\alpha^2 p_\alpha^2)} \tag{5.3}$$

where m_i and n_i are the direction cosines projected on $\{hkl\}$ with $i = \alpha$ the transverse $\perp$ directions, and $i = \beta$ the longitudinal $\parallel$ directions along the plane of the plate. The effective Poisson's ratio, $\nu_{\{hkl\}}^{\alpha\beta}$, was referenced at $\alpha = \langle 110 \rangle$ and $\beta = \langle 001 \rangle$ and the reduced compliance matrix was computed at the relevant angles.

5.3.3 Experimental Anisotropic Fracture Toughness

Niihara's extension(Niihara, 1983) of the LEM model is deemed more accurate in brittle materials as it accounts for the shape of the crack(Niihara, Morena, & Hasselman, 1982). For long cracks with $b/a > 2.5$, Niihara related the critical SIF to the total crack length through indentation parameters:

$$\left(K_{1c}\phi/H_{\mathrm{V}}\sqrt{a}\right)(H_{\mathrm{V}}/E\phi)^{2/5} = \zeta(b/a)^{-3/2} \tag{5.4}$$

where $\zeta \approx 0.129$ is the shape factor for median cracks(Niihara, 1983) with ϕ the hardness-to-yield stress ratio, b is the total median crack length and E is the Young's modulus. $K_{1\mathrm{c}}$ in Eq. (5.4), is induced by the residual stress field during the unloading, and it is not related to the superimposition of the elastic-plastic field at full load. In this work, Young's modulus was adapted to account for the anisotropy of GaAs, leading to a modification of Eq. (5.4):

$$K_{1\mathrm{c}\{hkl\}}^{\langle uvw\rangle}/\phi^{-\frac{3}{5}} = H_{\mathrm{V}}\sqrt{a}\left(E_{\{hkl\}}^{\langle uvw\rangle}/H_{\mathrm{V}}\right)^{\frac{2}{5}}\zeta(b/a)^{-\frac{3}{2}} \tag{5.5}$$

In the case of ceramics, nano-crystalline metal alloys, and single crystal silicon, the term ϕ is usually approximated as 3 times the yield strength(Ebrahimi & Kalwani, 1999; Li & Ebrahimi, 2003; Niihara, 1983; Niihara et al., 1982; M. Tanaka, Higashida, Nakashima, Takagi, & Fujiwara, 2003; Zhang, Li, & Zhang, 2011)·(Tabor, 1951). The hardness-to-yield strength ratio at ambient temperature for GaAs, ϕ, has not been reported by previous studies, hence in this study $\phi = \{2, 3, 4\}$ were considered.

5.3.4 Experimental Anisotropic Fracture Energy

In the past, it has been pointed out that no equivalent, homogeneous Young's modulus exists that could relate G_{1c} to K_{1c} and concurrently satisfy the condition of orthotropy(DelRio, Cook, & Boyce, 2015; Lawn, 1993; Lawn & Wilshaw, 1975; Rickhey, Marimuthu, Lee, & Lee,

2019; Wachtman, 1974). To overcome this issue, two-dimensional anisotropic elasticity was conveniently expressed in terms of analytic functions with a complex variables approach(Gao et al., 2013, 2009; Sih et al., 1965). The stress field description near the crack-tip for anisotropic cracked bodies was considered assuming that the median crack extension was relatively straight. Similarly to the recent work on single crystal silicon(Moulins et al., 2020), the mode 1 SIF was related to the energy release rate (ERR or G_1) by a crack closure model(Gao et al., 2013, 2009; Sih et al., 1965):

$$G_1 = \lim_{\delta \to 0} \frac{1}{\delta} \int_0^{\delta} \left[\sigma_1 (\delta - r_{\varphi=0}) \cdot u_1 r_{\varphi=\pi} \right] dr \tag{5.6}$$

After the relevant stress and displacement were substituted into the expression, the critical ERR was obtained as:

$$G_{1c} = -(\pi/2) {K_{1c}}^2 S_{22} \mathrm{Im}((\mu_1 + \mu_2)/\mu_1 \mu_2) \tag{5.7}$$

where μ_1 and μ_2 are the non-conjugated complex roots pair obtained from the solution of the bi-harmonic equation for anisotropic bodies, σ_1 the stress orthogonal to the propagation and u_1 the displacement with r_φ the radial crack positions. The analysis assumed that the crack-tip speed was zero once the half-penny crack reached its final dimension. To maintain the relationship between K_{1c} and G_{1c}, an equivalent Young's modulus, $\xi_{\{hkl\}}^{\langle uvw \rangle}$, was defined:

$$1/\xi_{\{hkl\}}^{\langle uvw \rangle} = -(\pi/2) S_{22} \mathrm{Im}(\mu_1 + \mu_2/\mu_1 \mu_2) \tag{5.8}$$

In Eq. (5.8), $\xi_{\{hkl\}}^{\langle uvw \rangle}$ is associated to the release of the compressive strain energy during unloading. The fracture energy was then computed for plane strain(Irwin, 1958; Nemeth, 2011) as:

$$\pi {K_{1c\{hkl\}}^{\langle uvw \rangle}}^2 / \xi_{\{hkl\}}^{\langle uvw \rangle} = G_{1c\{hkl\}}^{\langle uvw \rangle} / \left(1 - {\nu_{\{hkl\}}^{\alpha\beta}}^2\right) \tag{5.9}$$

Combining Eq. (5.9) with Eq. (5.5), the normalized ERR was then calculated:

$$\mathrm{G}_{1c\{hkl\}}^{\langle uvw\rangle}/\phi^{-6/5} = \zeta^2 H_V^{\frac{6}{5}} \frac{\pi a^4}{b^3}\left(1-\nu_{\{hkl\}}^{\alpha\beta\ 2}\right) E_{\{hkl\}}^{\langle uvw\rangle^{\frac{4}{5}}} \Big/ \xi_{\{hkl\}}^{\langle uvw\rangle} \tag{5.10}$$

Equation (5.10) provided the means to evaluate the ERR for the generalized plane strain state. Due to the lack of precise knowledge about ϕ in Eq. (5.10), the magnitude of $\mathrm{G}_{1c\{hkl\}}^{\langle uvw\rangle}$ could not be established exactly but instead it was normalized with respect to the main orientation of the plane of cleavage i.e. $\langle 001\rangle$ where $\mathrm{G}_{1c\{001\}}^{\langle uvw\rangle}\left(\theta = \frac{\pi}{4}\left[\frac{\pi}{2}\right]\right) = \mathrm{G}_{1c\{001\}}^{\langle 001\rangle}$.

5.3.5 Theoretical Fracture Energy from Broken Bonds

Based on geometrical observations, the fracture energy in GaAs was estimated from the number of broken bonds(Albe, Nordlund, Nord, & Kuronen, 2002; Brozel & Stillman, 1996; DelRio et al., 2015; Harkins, 1942; Wolff & Broder, 1959). In particular, GaAs's directional fracture energy, $\Gamma_{\{hkl\}}$, was estimated using the product of the zincblende GaAs bonding energy modulus(Albe et al., 2002) $\left|E_b^{GaAs}\right| \cong 1.68\ eV$ and the number of broken bonds per unit primitive cell area for any given fracture plane following the general form:

$$\Gamma_{\{hkl\}}^{\langle uvw\rangle} = \frac{1}{{a_0}^2} \cdot \frac{4\left|E_b^{GaAs}\right|}{\sqrt{h^2+k^2+l^2}} \cdot max(h,k,l) \tag{5.11}$$

where the GaAs lattice parameter(Brozel & Stillman, 1996) is $a_0 \cong 5.65$Å. The approximate fracture energy, $\Gamma_{\{001\}}^{\langle 010\rangle}$, was obtained with respect to the $\langle 010\rangle$ defined by the zone axis vector reference vector $\overrightarrow{\mathrm{B}_{\langle 010\rangle}}$ i.e. with $l = 0$ to work inside the (001). The approximate fracture energy was normalized such as $\Gamma_{\{001\}}^{\langle uvw\rangle}/\Gamma_{\{001\}}^{[100]}$ in order to properly compare the trend with the experimental $\mathrm{G}_{1c\{001\}}^{\langle uvw\rangle}/\mathrm{G}_{1c\{001\}}^{\langle 001\rangle}$. The analytical fracture energy of other relevant crystallographic zone axis was estimated by varying the orientation of the main zone axis vector reference $\overrightarrow{\mathrm{B}_{\langle hkl\rangle}}$ with $l \in [0; 9]$.

5.4 Results

Approximately 240 cracks were introduced and inspected (about 40 cracks per relative rotation θ). The hardness obtained from the Vickers indentation was found to remain relatively constant regardless of the relative rotation θ as presented by the averaged hardness (H_V) in Table 5.2, although in a few cases the imprint shapes appeared slightly distorted at θ = 30° and 50°, as shown in Figure 5.3 (d)-(e). For $0 < \theta < 50°$, the hardness's average for all orientations combined was 6.35 ± 0.363 GPa. For $\phi = \{2, 3, 4\}$, the expected yield stress range was $\sigma_Y = 1.5\ to\ 3.5$ GPa.

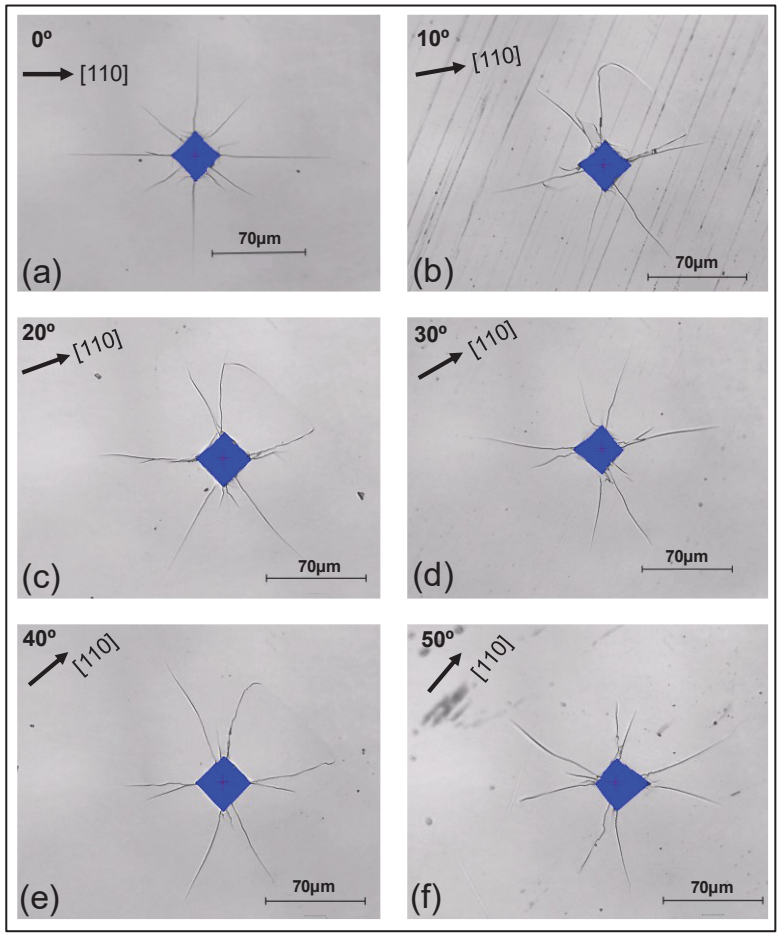

Figure 5.3 Representative micrographs of indentations in single crystal GaAs for 0<θ<50° between [110] and the indenter diagonal direction: (a) at θ= 0º, (b) at θ= 10º, (c) at θ= 20º, (d) at θ= 30º, (e) at θ= 40º, and (f) at θ= 50º.

The orientation θ does not have a significant influence on the macroscopic crack size and direction, except for $\theta = 0$. For orientations $10° < \theta < 50°$, short, lateral cracks formed during loading. The lateral cracks continued to propagate during the discharge producing loops with $\langle 100 \rangle$ crack paths connecting mostly $\langle 110 \rangle$ crack tips.

Figure 5.4 (a) shows a plot of the normalized fracture toughness $K_{1c\{001\}}^{\langle uvw \rangle}$ versus the crack length b, normalized to the diagonal lengths to mitigate the effect of distortions as seen in Figure 5.3 (d) and (f).

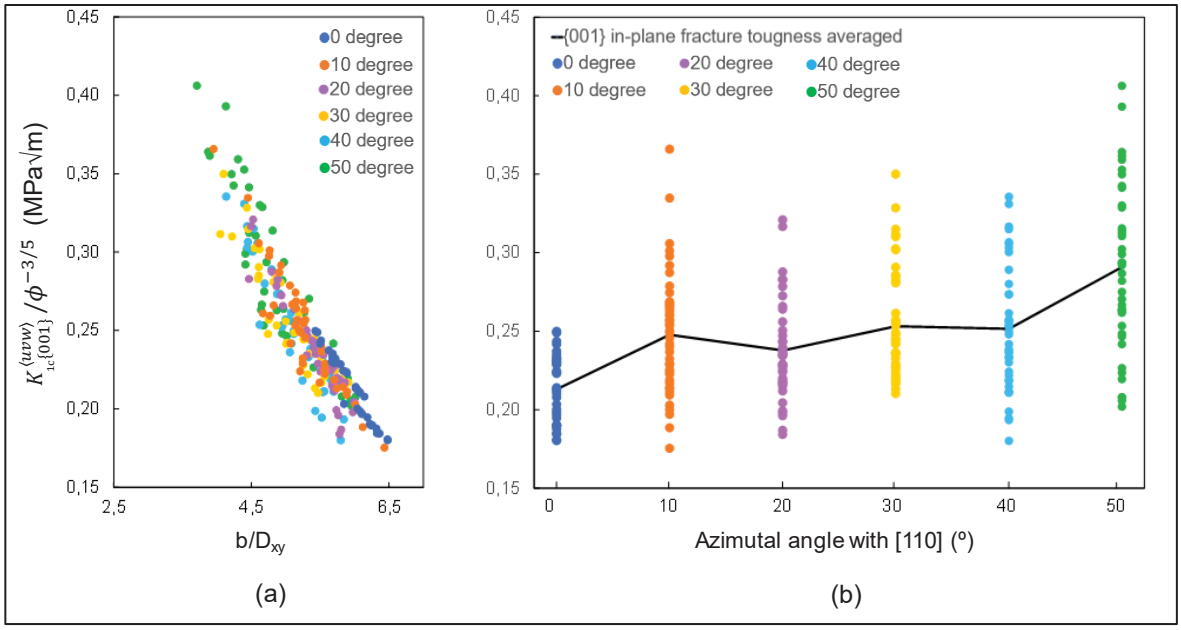

Figure 5.4 (a) normalized fracture toughness vs crack length normalized by the indenter diagonal, and (b) evolution of the critical SIF for six crystallographic orientations.

As observed in Figure 5.4 (a), the normalized toughness was found to be inversely proportional to b/D_{xy}. Moreover, the normalized crack length decreased as the misalignment with the indenter axis increased. Figure 5.4 (b) shows the normalized fracture toughness for various crystallographic specimen's orientations off the [110] (i.e. misaligned with the indenter diagonal). For each orientation $0 < \theta < 50°$, each set of crystallographic orientation consistently displayed a fracture behavior that enhanced cracks in the $\{hh0\}$ and $\{h00\}$ families with additional detected planes such as {170}, {370}, {670}, {290}, {790}, {890},

{450}, {560}, {580}, {780}, {980}, {610}, {810}, {920} and {940}. In Figure 5.4 (b), for each orientation $0 < \theta < 50°$, the averaged normalized toughness is presented in detail Table 5.2 with an amplitude of 0.18-0.41 MPa√m. It was also noted that the 50º orientation introduced the largest scatter in the toughness measurements.

Table 5.2 Summary table of GaAs hardness, expected yield stress range (ϕ={2,3,4}) and experimental fracture toughness for different orientations θ

θ	0°	10°	20°	30°	40°	50°
H_V (GPa)	6.49 ± 0.0775	6.60 ± 0.202	5.99 ± 0.0757	6.05 ± 0.0937	5.93 ± 0.0739	7.06 ± 0.816
$K_{1c\{001\}}^{\langle uvw\rangle}/\phi^{-\frac{3}{5}}$ (MPa√m)	0.21±0.019	0.25±0.029	0.24±0.024	0.25±0.027	0.25±0.032	0.29±0.045
$\sigma_Y^{\phi=2}$ (GPa)	3-3.5					
$\sigma_Y^{\phi=3}$ (GPa)	2-2.4					
$\sigma_Y^{\phi=4}$ (GPa)	1.5-1.8					

It has been shown that most of the cracks systematically propagated on the same plane, resulting in semi-elliptical cracks as identified by red arrows in Figure 5.5 (a) and (b). The crack in the figure was observed after fracturing a sample indented with the axis parallel to ⟨110⟩, as seen in Figure 5.3 (a). For the case shown, the half-elliptical axis lengths were 97x76μm. Figure 5.5 (b) also shows that the imprint is fragmented by the pyramidal compression.

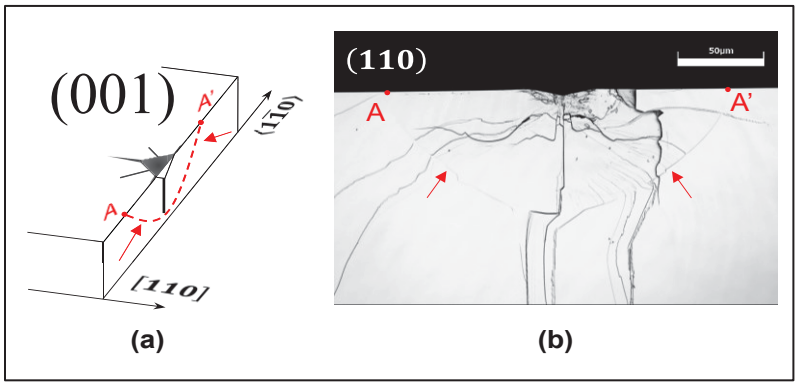

Figure 5.5 (a) Schematic representation of an opened GaAs indented surface with indenter aligned with ⟨110⟩ with (b) GaAs semi-elliptical crack shape (97x76μm) imaged by confocal microscopy

5.5 Discussion

Currently, there is no consensus in the literature about which fracture criterion applies to crack initiation and propagation in single crystals: is the maximum tensile stress (MS-Criterion) or the maximum ERR (ME-Criterion) better suited to GaAs? Therefore, both MS-Criterion (see Eq. (5.2)) and ME-Criterion (see Eq. (5.8)) were considered for the failure criteria and compared through the fracture energy evaluation.

The fracture energy can be based on $\xi_{\{hkl\}}^{\langle uvw \rangle}$ (i.e. associated with the ME-Criterion as described by Eq. (5.8)). Alternatively, the experimental fracture energy of GaAs can be computed based on the experimental fracture toughness through the directional elastic Young's modulus (i.e. associated to the MS-Criterion as described by Eq. (5.2)).

Figure 5.6 (a) shows the experimental plane strain fracture energies obtained using MS-Criterion and ME-Criterion compared to the theoretical broken bonds fracture energy model. The normalized experimental fracture energy based on the MS-Criterion $E_{\{001\}}^{\langle uvw \rangle}$ was $G_{1c\{001\}}^{\langle 110 \rangle}/G_{1c\{001\}}^{[100]}(\text{MS}) = 0.69$. The normalized experimental fracture energy based on the ME-Criterion was calculated using Eq. (5.10) where $G_{1c\{001\}}^{\langle 100 \rangle}/G_{1c\{001\}}^{[100]} = 1$ as the reference

ERR and we find $G_{1c\{001\}}^{\langle 110\rangle}/G_{1c\{001\}}^{[100]}(\mathrm{ME}) = 0.57$. In both cases, the fracture energy exhibits a four-fold symmetry, consistent with the crystal symmetry of GaAs. The results from the theoretical broken bonds model indicate $\Gamma_{\{001\}}^{\langle 110\rangle}/\Gamma_{\{001\}}^{[100]} = 0.71$, and are in good agreement with experimental observations calculated by either method.

In the MS-Criterion case involving $E_{\{001\}}^{\langle uvw\rangle}$, the computed fracture energy was more "circular" towards the $\langle 100\rangle$ zone axis compared with the directional elastic Young's moduli shapes. Both the MS-Criterion and ME-Criterion yield similarly satisfying results, so either option seems acceptable.

The good agreement of the theoretical broken bonds model with experimental observation suggests that this simple theoretical model may predict the full GaAs fracture energy envelope for experimentally unobtainable (or unavailable) fracture directions. As an illustration, the theoretical fracture energy crystallographic directions about $(1\bar{1}0)$ (experimentally unavailable) can be calculated by varying the main zone axis vector reference, as presented in Figure 5.6 (b). Changing the analytical reference zone axis vector $\overrightarrow{\mathrm{B}_{\langle hkl\rangle}}$, fracture energies of experimentally unobtainable fracture planes, such as $\{111\}$ and $\{112\}$ can be predicted, since the $\langle 111\rangle$ and $\langle 112\rangle$ zone axes, for instance, are both available in the same $\{1\bar{1}0\}$ family of planes. Table 5.3 provides a summary of the experimental and theoretical fracture energies.

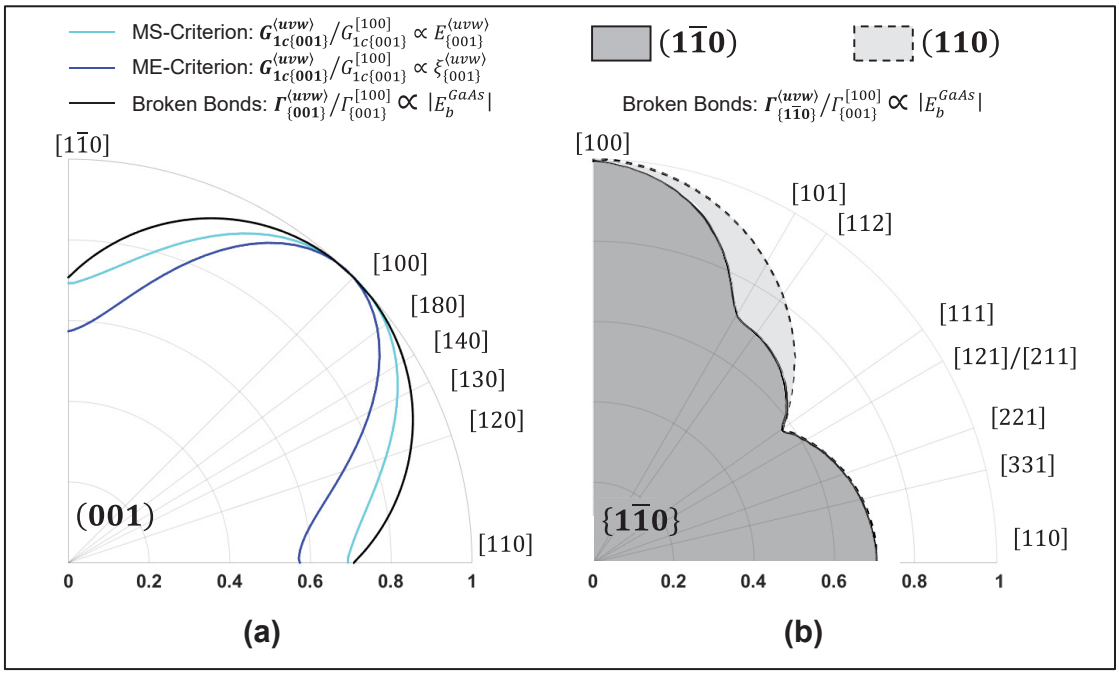

Figure 5.6(a) Experimental plane strain fracture energies obtained using MS-Criterion and ME-Criterion compared to theoretical broken bonds fracture energy model with (b) $\{11\bar{0}\}$ GaAs theoretical fracture energy from broken bonds

In all cases, the fracture energy and toughness are lowest for $\{110\}$. This is consistent with theoretical prediction, experimental observation, and the literature, with $\{110\}$ being the dominant fracture plane.

Table 5.3 Summary of the $\{001\}$ in-plane experimental fracture energy $G_{1c}\{001\}$ ratios compared to broken bonds theoretical fracture energy $\Gamma\{001\}$ and $\Gamma\{11\bar{0}\}$

Zone Axis	$G^{\langle hkl\rangle}_{1c\{001\}}/G^{\langle 001\rangle}_{1c\{001\}}$ (MS)	$G^{\langle hkl\rangle}_{1c\{001\}}/G^{\langle 001\rangle}_{1c\{001\}}$ (ME)	$\Gamma^{\langle uvw\rangle}_{\{001\}}/\Gamma^{\langle 100\rangle}_{\{001\}}$ (Broken Bonds)	$\Gamma^{\langle uvw\rangle}_{\{1\bar{1}0\}}/\Gamma^{\langle 100\rangle}_{\{001\}}$ (Broken Bonds)
⟨001⟩	1	1	1	1
⟨110⟩	0.69	0.57	0.71	0.71
⟨111⟩				0.58
⟨112⟩				0.82

The MS-Criterion slightly overestimates the fracture energy compared to the ME-Criterion but overall, we find no significant difference for GaAs. However, in the present Vickers indentation experiment cracks could in principle continue propagating during unloading due to the release of compressive stresses. This physical interpretation encourages us have a slight preference for selecting the ME Criterion of $\xi_{\{hkl\}}^{\langle uvw \rangle}$ for G_{1c}.

5.6 Conclusion

Vickers indentation was used to generate controlled cracks in single crystal GaAs. The anisotropy of GaAs fracture energy and toughness was addressed by considering a directional elastic Young's modulus based on the maximum tensile stress generated by the Vickers contact pressure (MS-Criterion). The calculation of the fracture toughness was accomplished without resorting to hardness-to-yield stress ratio or homogenization of elastic properties. The experimental fracture energy and toughness were obtained for all directions about (001), and compared to a theoretical broken bonds fracture energy model. Fractographic analysis confirmed that the {110} GaAs crack shape induced by Vickers indentations was half-elliptical. The theoretical method that has been developed in this study is a very efficient technique that can produce a full GaAs fracture energy envelope by changing the main zone axis reference vector.

GENERAL CONCLUSIONS

Fractography relies on topographic features on fracture surfaces to predict the stress state of failed components. Mirror constants of glasses and small grain ceramics are well established and have led to the creation of industry standards. As these methods were primarily developed for isotropic materials, they were not directly transferable to single crystals that are widely used in optoelectronics.

In this thesis, we studied the dynamic crack front behavior in functional single-crystalline wafers related to the fracture surface topographic singularities. The emphasis was laid initially on silicon as a pure cubic model material and the study was extended to another cubic material, GaAs, a compound sphalerite crystal. Fractography provided an invaluable opportunity to consistently investigate and understand the crystal's failure particularly for the brittle and fast-crack propagation in anisotropic materials. The work was done under bending and indentation conditions covering multiscale mechanical properties prediction using fractography combined with analytical and empirical models.

A new objective characterization technique for the fractographic analysis of silicon fracture surfaces on the (110) plane was introduced. Unlike previous works, the quantitative fractographic method developed considered the intrinsic anisotropy of the cubic single crystal. A fractographic procedure was applied to identify and analyze specific cleavage planes associated with dynamic instabilities in single crystal silicon with crystallographic orientation references. Both confocal microscopy and atomic force microscopy were used to locate and map fractographic planes associated with mirror and branching region. In this fractographic analysis, angle maps were computed from 3D surface profilometries classifying the crystallographic planes when first branching occurred. A passband angle filter with a fractographic feature detection algorithm was developed to highlight the mirror region along with an experimental protocol with crystallographic references.

An analytical dynamic fracture model was developed and used along with a crack-branching criterion to establish which cleavage plane would best correlate with the strength of samples

and the onset of the branching region. With the aid of the analytical model, it was determined that features corresponding to the {112} planes were Wallner lines and hence they were not relevant when estimating the strength. The shortest length between crack origin and the detected {111} cluster of points at branching eventually standardized the objective evaluation of crystal hackle radii where {111} planes delineated the mirror zone (analogous to the "mirror radius" in isotropic materials). Therefore (110) cleavage planes were associated with fractographic mirror's features in monocrystal silicon and branching regions were associated to (111) defection planes surrounded by (112) crystallographic Wallner lines. The experimental radii were subsequently correlated with experimental strengths to provide the Si crystal hackle constant $A_{XH\{110\}} = 1.47 \pm 0.24 MPa\sqrt{m}$ as the anisotropic silicon fractographic constant. This framework extended Orr's empirical relation for isotropic media to Si single crystals and established for the first time the correspondent anisotropic crystal hackle constant. The crack-tip dynamic stress field and local deflection were explored and validated by experiment. The branching planes and fractographic patterns predicted by the analytical model were in good agreement with the experimental findings and correctly anticipated that the planes that were bounding the mirror region. The analytically computed crystal hackle constant was consistent with the experimental one. Results allowed strength estimation in single crystal silicon by fractography and provided the intrinsic crystal hackle constant.

The later quantitative fractographic method applied to Si was generalized to anisotropic GaAs single crystals to consistently characterize another cubic crystal and strengthen the proposed method. GaAs fracture surface morphologies were studied based on the same objective procedures. GaAs has a zinc blende cubic structure, not unlike the diamond structure of Si. However, because GaAs is a compound, it behaves somewhat differently than Si.

The systematic approach to estimate the strength of fractured Si was applied to GaAs single crystals. Fractographic standards typically employed for homogeneous, isotropic materials were also adapted to study GaAs fracture. The fractographic signature of GaAs crystals was investigated with respect to the symmetries in the cubic compound and the symmetry of crystallographic features was confirmed by advanced stereography. Local crystallographic

paths were revealed and associated with a quasi-static mechanism. The crack-front re-aligned with the direction orthogonal to the maximum tensile stress when the cleavage plane was misaligned with loading. These fractographic features were used to precisely locate the crack origin even when it was not directly available. The crystal hackle radius of GaAs was defined coinciding with the macroscopic {111} deflection of the crack front, as in Si, but it was predominantly aligned with $\langle 2\bar{2}1 \rangle$. It was noted that hackles were different sets of planes in the form of crystallographic facets away from the crack origin. Cracks that generally propagated along the {110} planes were related to the mirror region. From those planes, local instability of crack occurred along 〈221〉 to form hackles features out of the mirror's plane. This framework also extended Orr's empirical relation for isotropic media to GaAs single crystals and establishes the correspondent crystal hackle constant $A_{XH}{}^{\langle 221 \rangle}_{(110)}$= 1.58 MPa√m to estimate the GaAs strength as in Si single crystals. Advanced microscopy and statistical distribution analysis of planes angles revealed that the mirror-branching boundary corresponded to specific planes as the crack-tip deviated from the {110} plane. Fractographic features observed experimentally corresponded to the intrinsic crystal symmetries of GaAs and were inferred by a multi-profilometry technique in the associated branching region. Hackles were a combination of well-defined zones of planes that consolidated mostly along with the {111} family as the crack was propagating. These facets were found delineating the mirror branching boundary in GaAs single crystals.

Such boundary that was composed of multiple crystallographic facets of different planes implied that different sets of fracture energy were required to deflect the cracks. Unfortunately, as for the case of the Si, the fracture energy and toughness evaluation of the fracturing planes in single crystals are poorly investigated in the literature. It is eventually one of the major issues in the field of brittle fracture as the crystal properties are highly anisotropic and the materials highly brittle at ambient temperature. Fracture toughness and energy are a subject of debate in the literature, especially because of the plethora of models that exist and because all are applied using isotropic assumptions with elastic properties that are systematically homogenized. Therefore, there was a need of developing new ways to obtain fracture toughness and energy

with the relevant anisotropic assumptions as they are the main properties that structured the onset of branching thus delineating the mirror region in Si and GaAs.

The modified Vickers indentation method described in this thesis considered the intrinsic anisotropy of gallium arsenide single crystals. Indents and fractographic features observed followed the intrinsic crystal symmetries of GaAs. Fracture mostly occurred with a four-fold symmetry inside the (001) although multiple fracture planes went detected. Cracks propagated along the {110} planes related to the mirror region but also on other planes when the indenter was not aligned with principal cleavage planes. Local instability of the crack occurred when misalignment was mostly above 40 degrees with surface chipping and some imprint distortion. Normalized fracture toughness and fracture energy were analytically expressed and experimentally evaluated. They were compared with a simplified theoretical model from the number of broken bonds and the maximum stress versus maximum energy release rate criteria were compared when evaluating the fracture energy of the brittle single crystals.

This work elucidates how it is possible to objectively obtain the mirror constants of Si and GaAs based on the fundamental principle of fractography and how these intrinsic fractographic parameters can be correlated with the fracture stress. It also demonstrated how the branching should be characterized and could be used to precisely identify the crack origin in cubic crystal and even when the fragment of the crack origin is missing. These outcomes allowed developing an analytical model that predicted the fracture dynamics in a cubic semiconductor crystal in Si. The model explained how non-relevant the Wallner lines were in the evaluation of the onset of the branching. It explicitly gave credit and validate for the first time the applicability of the maximum SIF as an invaluable crack-branching criterion for the evaluation or the mirror-branching boundary in anisotropic brittle crystals. The equivalent energy-based model obtained from the complex variable approach developed along with Vickers indentation allowed to compare the two main failure criteria when evaluating the fracture energy of anisotropic single crystals thus offering comparative understanding between energy concepts and linear elastic fracture mechanics alternative.

Therefore, this thesis work addresses the local anisotropy of Si and GaAs single crystals with innovative fractographic methods that could be generalized to any class of single crystals. It proposes strength estimates with a better understanding of the material properties than what was available in the literature. It has demonstrated his relevance to transform the ability of researchers to better study the multiscale state of stress in anisotropic functional crystals using quantitative fractography with fracture mechanics. Besides the fundamental understanding and original methods developed, this work could be used as a valuable asset for the mechanical design of microsystems. This will eventually lead to an increase in the mechanical reliability of MEMS and could significantly reduce systematic waste, replacements, and real-world device failures.

RECOMMENDATIONS

Post-mortem fracture surfaces analysis proposes new insights on the dynamic crack front as well as topographic singularities formation understanding outside main cleavage planes. Hackles, mirrors, particle-like collision fractographic features outline possible individual material asperities, defects, and probable particles interaction with dynamic crack-front waves. Fundamentally, it has been shown that dynamic instabilities involved crack-tip deflections. Nevertheless, it is still needed to understand precisely what the crack front wave deflection mechanisms and the sources of energy consumption that guide the brittle fracture are at the branching point and beyond. This would allow the development of a clear understanding of the mechanisms by which the crack's kinks influence the terminal propagation.

Therefore, it is suggested here to further extend this work at the branching stage and beyond to further extend the work in Si presented in chapter 3. The future goals would include strengthening the analytical model presented to predict accurately the anisotropic crack-tip behavior beyond the branching defined as the main dynamic instability occurring for the (110) cleavage in single crystal silicon (i.e., predict the so-called cusp). Indeed, this thesis scope was particularly emphasizing the mechanical property's predictions at the early stage of the propagation thus mostly focused on the mirror's standard shape evaluation, its understanding, and its boundary evaluation that was delineated by the branching region.

The next work could eventually include generalizing the analytical model developed for the Si to predict GaAs fracture dynamics thus further extending the study presented in chapter 4. As the GaAs fracture surfaces developed much complex fractographic features than Si, it is also recommended to further developing the fractographic analysis of GaAs single crystals by jointly developing high-speed imaging techniques and improve the profilometric technique.

Moreover, it is recommended to investigate the fracture surface markings in correlation with the aspects of the dynamic crack propagation in Germanium by generalizing the present fractographic methods and analytical model to a third cubic crystal.

Furthermore, the investigation on the influence of the bending contact line of 3PBTs on the dynamic crack-front shape could rise more understanding of the way the crack front deforms along with dynamic instabilities. It could generate further understanding of the branching formation mechanisms. It is also recommended to analyze the influence of the pre-crack size and location in various conditions of temperature, pressure, and relative humidity for Si, GaAs, and Ge. Finally, it is strongly recommended to keep investigating the physical anisotropic properties of single crystals such as the yield stress, fracture, toughness, and energy as most of them are missing in the literature at the operating temperature or are not addressing satisfactorily the intrinsic anisotropy of crystals.

Although there still pertains central questions that remain challenging such as the difficulty to explain the small-scale discrete behavior and the continuous macroscopic behavior of brittle single crystals experimentally, this thesis offers a deep understanding of the fracture morphologies of highly anisotropic single crystals at small scales and most certainly fills the gap by bringing new ways to study anisotropic fracture surfaces and the associated state of stresses.

BIBLIOGRAPHY

Abdel-Latif, A. I. A., Tressler, R. E., & Bradt, R. C. (1978). Fracture mirror formation in single crystal alumina. *Applications and Non-Metals*, 933–939. Retrieved from http://www.gruppofrattura.it/ocs/index.php/ICF/ICF4/paper/view/2580

Albe, K., Nordlund, K., Nord, J., & Kuronen, A. (2002). Modeling of compound semiconductors: Analytical bond-order potential for Ga, As, and GaAs. *Physical Review B - Condensed Matter and Materials Physics*, *66*(3), 352051–3520514. https://doi.org/10.1103/PhysRevB.66.035205

Anstis, G. R., Chantikul, P., Lawn, B. R., & Marshall, D. B. (1981a). A Critical Evaluation of Indentation Techniques for Measuring Fracture Toughness: I, Direct Crack Measurements. *Journal of the American Ceramic Society*, *64*(9), 533–538. https://doi.org/10.1111/j.1151-2916.1981.tb10320.x

Anstis, G. R., Chantikul, P., Lawn, B. R., & Marshall, D. B. (1981b). A Critical Evaluation of Indentation Techniques for Measuring Fracture Toughness: II, Strength Method. *Journal of the American Ceramic Society*, *64*(9), 533–538. https://doi.org/10.1111/j.1151-2916.1981.tb10320.x

Arcisz, M., & Sih, G. C. (1984). Effect of orthotropy on crack propagation. *Theoretical and Applied Fracture Mechanics*. Retrieved from https://www.sciencedirect.com/science/article/pii/016784428490003X

ASTM. (2010a). Standard practice for fractographic analysis of fracture mirror sizes in ceramics and glasses. *ASTM International*, (C), 1–15. https://doi.org/10.1520/C1678-10

ASTM. (2010b). Standard practice for fractography and characterization of fracture origins in advanced ceramics. *ASTM International*, (Reapproved 2010), 1–51. https://doi.org/10.1520/C1322-05BR10.2

ASTM. (2013). Standard Test Method for Flexural Strength of Advanced Ceramics at Ambient Temperature. *ASTM International*, 1–19. https://doi.org/10.1520/C1161-13

ASTM. (2017). Standard Test Method for Microindentation Hardness of Materials. *ASTM International*, 1–40. https://doi.org/10.1520/E0384-17

ASTM. (2019). Standard Test Method for Vickers Indentation Hardness of Advanced Ceramics. *ASTM International*, (March), 1–10. https://doi.org/10.1520/C1327-08.2

Atkinson, C. (1965a). The propagation of a brittle crack in anisotropic material. *International Journal of Engineering Science*, *3*(1), 77–91. https://doi.org/10.1016/0020-7225(65)90021-2

Atkinson, C. (1965b). The propagation of fracture in aeolotropic materials. *International Journal of Fracture Mechanics*, *1*(1), 47–55. https://doi.org/10.1007/BF00184152

Azhdari, A., & Nemat-Nasser, S. (1996). Energy-release rate and crack kinking in anisotropic brittle solids. *Journal of the Mechanics and Physics of Solids*, *44*(6), 929–951. https://doi.org/10.1016/0022-5096(96)00012-9

Bahat, D., Bankwitz, P., & Bankwitz, E. (2003). Preuplift joints in granites: Evidence for subcritical and post-critical fracture growth. *Bulletin of the Geological Society of America*, *115*(2), 148–165. https://doi.org/10.1130/0016-7606(2003)115<0148:PJIGEF>2.0.CO;2

Ben-Bashat Bergman, L., & Sherman, D. (2019). On dynamic surface instabilities of cracks in brittle crystals. *International Journal of Engineering Science*, *136*, 78–91. https://doi.org/10.1016/j.ijengsci.2019.01.005

Blakemore, J. S. (1982). Semiconducting and other major properties of GaAs. *Journal of Applied Physics*, *53*(10), R123.

Blakemore, J. S. (1987). Gallium arsenide. *Key Papers in Physics ; No. 1*, *44*(0), 401 p. Retrieved from https://books.google.ca/books?id=6gCLvzDk4VgC&pg=PA64&lpg=PA64&dq=space+group+of+gallium+arsenide&source=bl&ots=Y7U4v0Sh4a&sig=Ng12qVgUA0DsA6TBkHP8fOnoipY&hl=fr&sa=X&ved=0ahUKEwjn76q8ssLbAhWQrFkKHb0EAb4Q6AEIejAH#v=onepage&q=space group of gallium arsenide

Brantley, W. A. (1973). Calculated elastic constants for stress problems associated with semiconductor devices. *Journal of Applied Physics*, *44*(1), 534–535. https://doi.org/10.1063/1.1661935

Brozel, M. R., & Stillman, G. E. (1996). *Properties of gallium arsenide*. IET.

Buehler, M. J., & Gao, H. (2006). Dynamical fracture instabilities due to local hyperelasticity at crack tips. *Nature*, *439*(7074), 307–310. https://doi.org/10.1038/nature04408

Cahn, J. W., & Hanneman, R. E. (1964). (111) Surface tensions of III-V compounds and their relationship to spontaneous bending of thin crystals. *Surface Science*, *1*(4), 387–398. https://doi.org/10.1016/0039-6028(64)90006-8

Chen, C. P. (2002). Fracture mechanics evaluation of optical fibers. *Materials Chemistry and Physics*, *77*(September 2001), 110–116. https://doi.org/10.1016/S0254-0584(01)00578-8

Chen, C. P., & Leipold, M. H. (1980). Fracture toughness of silicon. In *ntrs.nasa.gov*. Retrieved from https://ntrs.nasa.gov/search.jsp?R=19800047921

Chen, C. P., & Morrissey, C. J. (1984). Fracture mechanics evaluation of GaAs. In *Nasa Tech Brief* (Vol. 11). Retrieved from https://ntrs.nasa.gov/search.jsp?R=19850014790

Cho, C. H. (2009). Characterization of Young's modulus of silicon versus temperature using a "beam deflection" method with a four-point bending fixture. *Current Applied Physics*, *9*(2), 538–545. https://doi.org/10.1016/J.CAP.2008.03.024

Cook, R. F. (2006). Strength and sharp contact fracture of silicon. *Journal of Materials Science*, *41*(3), 841–872. https://doi.org/10.1007/s10853-006-6567-y

Cramer, T., Wanner, A., & Gumbsch, P. (2000). Energy Dissipation and Path Instabilities in Dynamic Fracture of Silicon Single Crystals. *Physical Review Letters*, *85*(4), 788–791. https://doi.org/10.1103/PhysRevLett.85.788

DelRio, F. W., Cook, R. F., & Boyce, B. L. (2015). Fracture strength of micro- and nano-scale silicon components. *Applied Physics Reviews*, *2*(2), 021303. https://doi.org/10.1063/1.4919540

Dugnani, R., & Ma, L. (2019). Energy release rate of moving circular-cracks. *Engineering Fracture Mechanics*, *213*, 118–130. https://doi.org/10.1016/J.ENGFRACMECH.2019.03.044

Dugnani, R., & Verghese, P. (2014). Failure analysis of modern silicon dice. *International Journal of Applied Ceramic Technology*, *11*(4), 783–792. https://doi.org/10.1111/ijac.12101

Dugnani, R., & Zednik, R. J. (2013). Flexural strength by fractography in modern brittle materials. *Journal of the American Ceramic Society*, *96*(12), 3908–3914. https://doi.org/10.1111/jace.12627

Dugnani, R., & Zednik, R. J. (2016). Geometric description of fracture surface features in isotropic brittle solids. *Engineering Fracture Mechanics*, *165*, 87–97.

Dushkina, N. M. (2015). Dicing of Gallium Arsenide (GaAs) Wafers with the Laser MicroJet ® Challenges , Improvements and Safety Issues. *Engineering*, (November).

Ebrahimi, F., & Kalwani, L. (1999). Fracture anisotropy in silicon single crystal. *Materials Science and Engineering: A*, *268*(1–2), 116–126. https://doi.org/10.1016/S0921-5093(99)00077-5

Edington, J. W. (1975). Electron Diffraction in the Electron Microscope. In *Electron Diffraction in the Electron Microscope* (pp. 1–77). https://doi.org/10.1007/978-1-349-02595-4_1

Eftis, J., & Liebowitz, H. (1972). On the Modified Westergaard Equations for Certain Plane Crack Problems. *International Journal of Fracture Mechanics*, *8*(4), 383–392. https://doi.org/10.1007/BF00191100

Evans, A. G., & Charles, E. A. (1976). Fracture Toughness Determinations by Indentation. *Journal of the American Ceramic Society*, *59*(7–8), 371–372. https://doi.org/10.1111/j.1151-2916.1976.tb10991.x

Freund, L. B. (1972). Crack propagation in an elastic solid subjected to general loading—I. Constant rate of extension. *Journal of the Mechanics and Physics of Solids*, *20*(3), 129–140. https://doi.org/10.1016/0022-5096(72)90006-3

Freund, L. B., & Clifton, R. J. (1974). On the uniqueness of plane elastodynamic solutions for running cracks. *Journal of Elasticity*, *4*(4), 293–299. https://doi.org/10.1007/BF00048612

Gallo, P., Hagiwara, Y., Shimada, T., & Kitamura, T. (2019). Strain energy density approach for brittle fracture from nano to macroscale and breakdown of continuum theory. *Theoretical and Applied Fracture Mechanics*, *103*, 102300. https://doi.org/10.1016/j.tafmec.2019.102300

Gallo, P., Yan, Y., Sumigawa, T., & Kitamura, T. (2020). Fracture behavior of nanoscale notched silicon beams investigated by the theory of critical distances. *Advanced Theory and Simulations*, *1*(1), 1700006. https://doi.org/10.1002/adts.201700006

Gao, X., Hou, L. A., Kang, X. W., & Wang, H. G. (2013). Characteristic of crack tip fields for dynamic fracture in anisotropic materials. *European Journal of Mechanics, A/Solids*, *37*, 122–131. https://doi.org/10.1016/j.euromechsol.2012.05.004

Gao, X., Kang, X. W., & Wang, H. G. (2009). Dynamic crack tip fields and dynamic crack propagation characteristics of anisotropic material. *Theoretical and Applied Fracture Mechanics*, *51*(1), 73–85. https://doi.org/10.1016/J.TAFMEC.2009.01.006

Gilman, J. J. (1958). Creation of cleavage strips by dislocations. *Trans. Metall. Soc. AIME*, *212*, 310–315. Retrieved from https://scholar.google.fr/scholar?hl=en&as_sdt=0%2C5&q=J.+J.+Gilman%2C+Trans.+AIME+212%2C+310+%281958%29&btnG=

Gilman, J. J. (1959). *Fracture* (Wiley; G. T. B. L. Averback, D. K. Felback & and D. A. T. Hahn, Eds.). Wiley, New York.

Gol'dstein, R. V., & Salganik, R. L. (1974). Brittle fracture of solids with arbitrary cracks. *International Journal of Fracture*, *10*(4), 507–523. https://doi.org/10.1007/BF00155254

Green, M. A., Emery, K., Hishikawa, Y., Warta, W., & Dunlop, E. D. (2015). Solar cell efficiency tables. *Progress in Photovoltaics: Research and Applications*, *23*(1), 1–9. https://doi.org/10.1002/pip.2573

Griffith, A. A. (1921). The Phenomena of Rupture and Flow in Solids. *Philosophical Transactions of the Royal Society A: Mathematical, Physical and Engineering Sciences*, Vol. 221, pp. 163–198. https://doi.org/10.1098/rsta.1921.0006

Hammond, C. (2015). *The Basics of Crystallography and Diffraction* (Vol. 21). Oxford University Press.

Haneman, D., & Pugh, E. N. (1963). Tear Marks on Cleaved Germanium Surfaces. *Journal of Applied Physics*, *34*(8), 2269–2272. https://doi.org/10.1063/1.1702727

Harkins, W. D. (1942). Energy relations of the surface of solids: I. Surface energy of the diamond. *The Journal of Chemical Physics*, *10*(5), 268–272. https://doi.org/10.1063/1.1723719

Hill, R. (1998). *The mathematical theory of plasticity* (Vol. 11). Oxford university press.

Hirsch, P. B., Pirouz, P., Roberts, S. G., & Warren, P. D. (1985). Indentation plasticity and polarity of hardness on (111) faces of GaAs. *Philosophical Magazine B: Physics of Condensed Matter; Statistical Mechanics, Electronic, Optical and Magnetic Properties*, *52*(3), 759–784. https://doi.org/10.1080/13642818508240635

Hjort, K., Ericson, F., Schweitz, J. Å., Hallin, C., & Janzén, E. (1994). Hardness, internal stress and fracture toughness of epitaxial AlxGa1-xAs films. *Thin Solid Films*, *250*(1–2), 157–163. https://doi.org/10.1016/0040-6090(94)90180-5

Hjort, K., Soderkvist, J., & Schweitz, J. A. (1994). Gallium arsenide as a mechanical material. *Journal of Micromechanics and Microengineering*, *4*(1), 1–13. https://doi.org/10.1088/0960-1317/4/1/001

Hopcroft, M., Nix, W. D., & Kenny, T. W. (2010). What is the Young ' s Modulus of Silicon ? *Journal of Microelectromechanical Systems*, *19*(2), 229–238. https://doi.org/10.1109/JMEMS.2009.2039697

Irwin, G. R. (1958). Fracture I - Elasticity and Plasticity. In S. Flügge (Ed.), *Encyclopedia of Physics* (pp. 551–590). https://doi.org/10.1007/978-3-642-45887-3_5

Kassir, M. K., & Tse, S. (1983). Moving Griffith crack in an orthotropic material. *International Journal of Engineering Science*. https://doi.org/10.1016/0020-7225(83)90116-7

Kaufman, M. J., & Forty, A. J. (1986). A detailed fractographic analysis of cleavage steps in silicon. *Journal of Materials Science*, *21*(9), 3167–3172. https://doi.org/10.1007/BF00553353

Kelly, A., & Macmillan, N. H. (1986). Strong Solids. In *Monographs on the physics and chemistry of materials.* (3rd ed.). Walton Street, Oxford: Oxford Clarendon Press.

Kermode, J. R., Albaret, T., Sherman, D., Bernstein, N., Gumbsch, P., Payne, M. C., … De Vita, A. (2008). Low-speed fracture instabilities in a brittle crystal. *Nature*, *455*(7217), 1224–1227. https://doi.org/10.1038/nature07297

Kirchner, H. P., & Kirchner, J. W. (1979). Fracture Mechanics of Fracture Mirrors. *Journal of the American Ceramic Society*, *62*(3–4), 198–202. https://doi.org/10.1111/j.1151-2916.1979.tb19053.x

Konagai, M., Sugimoto, M., & Takahashi, K. (1978). High-efficiency GaAs thin film solar cells by peeled film technology. *Journal of Crystal Growth*, *45*(Supplement C), 277–280. https://doi.org/https://doi.org/10.1016/0022-0248(78)90449-9

Lawn, B. R. (1993). Fracture of brittle solids. In *Cambridge solid state science series,*. https://doi.org/10.1017/CBO9780511623127

Lawn, B. R., Evans, A. G., & Marshall, D. B. (1980). Elastic/Plastic Indentation Damage in Ceramics: The Median/Radial Crack System. *Journal of the American Ceramic Society*, *63*(9–10), 574–581. https://doi.org/10.1111/j.1151-2916.1980.tb10768.x

Lawn, B. R., & Wilshaw, R. (1975, June). Indentation fracture: principles and applications. *Journal of Materials Science*, Vol. 10, pp. 1049–1081. https://doi.org/10.1007/BF00823224

Lee, J. H., Gao, Y. F., Johanns, K. E., & Pharr, G. M. (2012). Cohesive interface simulations of indentation cracking as a fracture toughness measurement method for brittle materials. *Acta Materialia*, *60*(15), 5448–5467. https://doi.org/10.1016/j.actamat.2012.07.011

Lee, K. H., Hawong, J. S., & Choi, S. H. (1996). Dynamic stress intensity factors KI, KII and dynamic crack propagation characteristics of orthotropic material. *Engineering Fracture Mechanics*, *53*(1), 119–140. https://doi.org/10.1016/0013-7944(95)00077-9

Lekhnitskii, S. (1963). *Theory of elasticity of an anisotropic elastic body*. Retrieved from http://www.worldcat.org/title/theory-of-elasticity-of-an-anisotropic-elastic-body/oclc/803145982

Levade, C., & Vanderschaeve, G. (1999). Rosette microstructure in indented (001) GaAs single crystals and the α/β asymmetry. *Physica Status Solidi (A) Applied Research*, *171*(1), 83–88. https://doi.org/10.1002/(SICI)1521-396X(199901)171:1<83::AID-PSSA83>3.0.CO;2-C

Li, H., & Ebrahimi, F. (2003). Synthesis and characterization of electrodeposited nanocrystalline nickel-iron alloys. *Materials Science and Engineering A.*, *347*(1–2), 93–101. https://doi.org/10.1016/S0921-5093(02)00586-5

Ma, L., & Dugnani, R. (2018). Improved fractographic strength estimates based on surface profilometry. *ICMAA*.

Ma, L., Dugnani, R., & Moulins, A. (2018). Non-Linearity of the Mirror Constant for Glasses Fractured in Flexure. *Journal of Shanghai Jiaotong University (Science)*, *23*(1), 182–189. https://doi.org/10.1007/s12204-018-1924-y

Ma, L., Moulins, A., & Dugnani, R. (2021). Analytical description of fracture features in single crystal silicon. *European Journal of Mechanics - A/Solids*, *87*, 104203. https://doi.org/10.1016/j.euromechsol.2020.104203

Margevicius, R. W., & Gumbsch, R. (1998). Influence of crack propagation direction on (110) fracture toughness of gallium arsenide. *Philosophical Magazine A: Physics of Condensed Matter, Structure, Defects and Mechanical Properties*, *78*(3), 567–581. https://doi.org/10.1080/01418619808241923

MATLAB version 9.6.0.1174912 (R2019a) Update 5. (2019). Natick, Massachusetts.

Mecholsky, J., Freiman, S. W., & Rice, R. W. (1978). Fractographic Analysis of Ceramics. In *Fractography in Failure Analysis* (pp. 363-363–17). https://doi.org/10.1520/STP38101S

Mecholsky, J. J., Freiman, S. W., & Rice, R. W. (1976). Fracture surface analysis of ceramics. *Journal of Materials Science*, *11*(7), 1310–1319. https://doi.org/10.1007/BF00545152

Messmer, C., & Bilello, J. C. (1981). The surface energy of Si, GaAs, and GaP. *Journal of Applied Physics*, *52*(7), 4623–4629. https://doi.org/10.1063/1.329342

Michot, G., George, A., Chabli-Brenac, A., & Molva, E. (1988). Fracture toughness of pure and In-doped GaAs. *Scripta Metallurgica*, *22*(7), 1043–1048. https://doi.org/10.1016/S0036-9748(88)80100-5

Mott, N. F. (1938). Energy Levels in Real and Ideal Crystals. *Trans. Faraday Soc.*, *34*(0), 822–827. https://doi.org/10.1039/TF9383400822

Mott, N. F. (1948a). Brittle fracture in mild steel plates. *Engineering*, Vol. 165, pp. 16–18.

Mott, N. F. (1948b). Fracture of metals: Theoretical considerations. *Engineering*, *165*(165), 16–18.

Moulins, A., Dugnani, R., & Zednik, R. J. (2021). Fracture Surface Analysis and Quantitative Characterization of Gallium Arsenide III-V Semiconductors using Fractography. *Engineering Failure Analysis*, *123*, 105313. https://doi.org/10.1016/j.engfailanal.2021.105313

Moulins, A., Ma, L., Dugnani, R., & Zednik, R. J. (2020). Dynamic crack modeling and analytical stress field analysis in single-crystal silicon using quantitative fractography. *Theoretical and Applied Fracture Mechanics*, *109*, 102693. https://doi.org/10.1016/j.tafmec.2020.102693

Muskhelishvili, N. I. (1954). Some basic problems of the mathematical theory of elasticity. In *ZAMM - Zeitschrift für Angewandte Mathematik und Mechanik* (Vol. 34). https://doi.org/10.1002/zamm.19540341224

Nemeth, M. P. (2011). *An In-Depth Tutorial on Constitutive Equations for Elastic Anisotropic Materials (NTRS - NASA)*. https://doi.org/Document ID 20110023650

Niihara, K. (1983). A fracture mechanics analysis of indentation-induced Palmqvist crack in ceramics. *Journal of Materials Science Letters*, *2*(5), 221–223. https://doi.org/10.1007/BF00725625

Niihara, K., Morena, R., & Hasselman, D. P. H. (1982). Evaluation of KIc of brittle solids by the indentation method with low crack-to-indent ratios. *Journal of Materials Science Letters*, *1*(1), 13–16. https://doi.org/10.1007/BF00724706

Ning, X. J., Perezt, T., & Pirouz, P. (1995). Indentation-induced dislocations and microtwins in GaSb and GaAs. *Philosophical Magazine A: Physics of Condensed Matter, Structure, Defects and Mechanical Properties*, *72*(4), 837–859. https://doi.org/10.1080/01418619508239938

Okui, T., Hasegawa, S., Fukutome, H., & Nakashima, H. (2000). Shearing orientation dependence of cleavage step structures on GaAs(110). *Surface Science*, *448*(2), 219–224. https://doi.org/10.1016/S0039-6028(99)01215-7

Orr, L. (1972). Practical Analysis of Fractures in Glass Windows. *Materials Research and Standards*, *12*(1), 21–23.

Paris, P. C., & Sih, G. C. (1965). Stress Analysis of Cracks. In *Fracture Toughness Testing and its Applications* (pp. 30-30–52). https://doi.org/10.1520/STP26584S

Pérez, R., & Gumbsch, P. (2000). Directional Anisotropy in the Cleavage Fracture of Silicon. *Physical Review Letters*, *84*(23), 5347–5350. https://doi.org/10.1103/PhysRevLett.84.5347

Piva, A. (1986). Elastodynamic crack problems in an anisotropic medium through a complex variable approach. *Quarterly of Applied Mathematics*, *44*(3), 441–445. https://doi.org/10.1090/qam/860897

Pons, A. J., & Karma, A. (2010). Helical crack-front instability in mixed-mode fracture. *Nature*, *464*(7285), 85–89. https://doi.org/10.1038/nature08862

Pouvreau, C., Wasmer, K., Hessler-Wyser, H., Ganière, J. D., Breguet, J. M., Michler, J., … Giovanola, J. H. (2013). Nanoindentation cracking in gallium arsenide: Part II. TEM investigation. *Journal of Materials Research*, *28*(20), 2799–2809. https://doi.org/10.1557/jmr.2013.275

Quinn, G. D. (2007). Guidelines for measuring fracture mirrors. *Ceramic Transactions*, *199*, 163–187. https://doi.org/10.1002/9781118144152.ch14

Quinn, G. D. (2016). NIST Recommended Practice Guide: Fractography of Ceramics and Glasses. In *National Institute of Standards and Technology; NIST Recommended* (Vol. 191). https://doi.org/10.6028/NIST.SP.960-16e2

Rice, J. R. (1968). Mathematical Analysis in the Mechanics of Fracture. *Mathematical Fundamentals*, *2*(B2), 191–311. https://doi.org/10.1029/2000JB000138

Rice, R. W. (1974). Fracture Topography of Ceramics. In *Surfaces and Interfaces of Glass and Ceramics* (pp. 439–472). https://doi.org/10.1007/978-1-4684-3144-5_24

Rickhey, F., Marimuthu, K. P., Lee, K., & Lee, H. (2019). Indentation cracking of monocrystalline silicon considering fracture anisotropy. *Theoretical and Applied Fracture Mechanics*, *100*, 128–138. https://doi.org/10.1016/j.tafmec.2019.01.002

Roberts, S. G., Warren, P. D., & Hirsch, P. B. (1986). Knoop hardness anisotropy on {001} faces of germanium and gallium arsenide. *Journal of Materials Research*, *1*(1), 162–176. https://doi.org/10.1557/JMR.1986.0162

Sauthoff, K., Wenderoth, M., Heinrich, A. J., Rosentreter, M. A., Engel, K. J., Reusch, T. C. G., & Ulbrich, R. G. (1999). Nonlinear dynamic instability in brittle fracture of GaAs. *Physical Review B*, *60*(7), 4789–4795. https://doi.org/10.1103/PhysRevB.60.4789

Sherman, D. (2003). Hackle or textured mirror? Analysis of surface perturbation in single crystal silicon. *Journal of Materials Science*, *38*(4), 783–788. https://doi.org/10.1023/A:1021809014702

Sherman, D. (2005). Macroscopic and microscopic examination of the relationship between crack velocity and path and Rayleigh surface wave speed in single crystal silicon. *Journal of the Mechanics and Physics of Solids*, *53*(12), 2742–2757. https://doi.org/10.1016/J.JMPS.2005.07.001

Sherman, D. (2006). Energy considerations in crack deflection phenomenon in single crystal silicon. *International Journal of Fracture*, *140*(1–4), 125–140. https://doi.org/10.1007/s10704-006-0048-9

Sherman, D. (2009). Fractography of Dynamic Crack Propagation in Silicon Crystal. *Key Engineering Materials*, *409*(November), 55–64. https://doi.org/10.4028/www.scientific.net/KEM.409.55

Sherman, D., & Be'ery, I. (2003). Shape and energies of a dynamically propagating crack under bending. *Journal of Materials Research*, *18*(10), 2379–2386. https://doi.org/10.1557/JMR.2003.0333

Sherman, D., & Be'ery, I. (2004). From crack deflection to lattice vibrations - Macro to atomistic examination of dynamic cleavage fracture. *Journal of the Mechanics and Physics of Solids*, *52*(8), 1743–1761. https://doi.org/10.1016/j.jmps.2004.02.004

Sherman, D., Markovitz, M., & Barkai, O. (2008a). Dynamic instabilities in (111) silicon. *J. Mech. Phys. Solids*, *56*(2), 376–387. https://doi.org/10.1016.j.jmps.2007.05.010

Sherman, D., Markovitz, M., & Barkai, O. (2008b). Dynamic instabilities in {1 1 1} silicon. *Journal of the Mechanics and Physics of Solids*, *56*(2), 376–387. https://doi.org/10.1016/j.jmps.2007.05.010

Sherman, D., Markovitz, M., & Barkai, O. (2008c). Dynamic instabilities in {111} silicon. *Journal of the Mechanics and Physics of Solids*, *56*(2), 376–387. https://doi.org/10.1016/j.jmps.2007.05.010

Shetty, D. K., Bansal, G. K., Rosenfield, A. R., & Duckworth, W. H. (1980). Criterion for Fracture-Mirror Boundary Formation in Ceramics. *Journal of the American Ceramic Society*, *63*(1–2), 106–108. https://doi.org/10.1111/j.1151-2916.1980.tb10661.x

Shimada, T., Ouchi, K., Chihara, Y., & Kitamura, T. (2015). Breakdown of continuum fracture mechanics at the nanoscale. *Scientific Reports*, *5*(1), 1–6. https://doi.org/10.1038/srep08596

Sih, G. C., Paris, P. C., & Irwin, G. R. (1965). *On Cracks in Rectilinearly Anisotropic Bodies*. (6).

Stewart, R. L., & Bradt, R. C. (1980). Fracture of single crystal MgAl204. *Journal of Materials Science*, *15*(1), 67–72. https://doi.org/10.1007/BF00552428

Stroh, A. N. (1957). *Advances in Physics A theory of the fracture of metals*. Taylor, Publisher.

Stroh, A. N. (1958). Dislocations and cracks in anisotropic elasticity. *Philosophical Magazine*, *3*(30), 625–646. https://doi.org/10.1080/14786435808565804

Stroh, A. N. (1962). Steady state oscillation problems in anisotropic elasticity. *Journal of Mathematics and Physics*, *41*, 77–103.

Sumigawa, T., Shimada, T., Tanaka, S., Unno, H., Ozaki, N., Ashida, S., & Kitamura, T. (2017). Griffith Criterion for Nanoscale Stress Singularity in Brittle Silicon. *ACS Nano*, *11*(6), 6271–6276. https://doi.org/10.1021/acsnano.7b02493

Tabor, D. (1951). *The hardness of metals* (Clarendon). Oxford: Oxford university press.

Tanaka, K., Kitahara, Y., Ichinose, Y., & Iimura, T. (1984). Fracture analysis of single crystal manganese zinc ferrites using indentation flaws. *Acta Metallurgica*, *32*(10), 1719–1729. https://doi.org/10.1016/0001-6160(84)90228-1

Tanaka, M., Higashida, K., Nakashima, H., Takagi, H., & Fujiwara, M. (2003). Fracture toughness evaluated by indentation methods and its relation to surface energy in silicon single crystals. *Materials Transactions*, *44*(4), 681–684. https://doi.org/10.2320/matertrans.44.681

Tsai, Y. L., & Mecholsky, J. (1991). Fractal fracture of single crystal silicon. *Journal of Materials Research*, *6*(06), 1248–1263. https://doi.org/10.1557/JMR.1991.1248

Tsai, Y. L., & Mecholsky, J. (1992). Fracture mechanics description of fracture mirror formation in single crystals. *International Journal of Fracture*, *57*(2), 167–182. https://doi.org/10.1007/BF00035717

Uchida, K., Zednik, R. J., Ching-Huang, L., Jagannathan, H., McVittie, J., McIntyre, P. C., & Nishi, Y. (n.d.). Experimental study of biaxial and uniaxial strain effects on carrier mobility in bulk and ultrathin-body SOI MOSFETs. *IEDM Technical Digest. IEEE International Electron Devices Meeting, 2004.*, 229–232. https://doi.org/10.1109/IEDM.2004.1419116

Wachtman, J. B. (1974). Determination of Elastic Constants Required for Application of Fracture Mechanics to Ceramics. In *Concepts, Flaws, and Fractography* (pp. 49–68). https://doi.org/10.1007/978-1-4684-2991-6_3

Wallner, H. (1939). Linienstrukturen an Bruchflächen. *Zeitschrift Für Physik*, *114*(5–6), 368–378. https://doi.org/10.1007/BF01337002

Wang, S., & Pirouz, P. (2007). Mechanical properties of undoped GaAs. III: Indentation experiments. *Acta Materialia*, *55*(16), 5526–5537. https://doi.org/10.1016/j.actamat.2007.06.029

Wasmer, K., Ballif, C., Gassilloud, R., Pouvreau, C., Rabe, R., Michler, J., … Schulz, D. (2005). Cleavage fracture of brittle semiconductors from the nanometer to the centimeter scale. *Advanced Engineering Materials*, *7*(5), 309–317. https://doi.org/10.1002/adem.200500044

Wasmer, K., Ballif, C., Pouvreau, C., Schulz, D., & Michler, J. (2008). Dicing of gallium-arsenide high performance laser diodes for industrial applications. Part II. Cleavage operation. *Journal of Materials Processing Technology*, *198*(1–3), 105–113. https://doi.org/10.1016/j.jmatprotec.2007.06.054

Wasmer, K., Pouvreau, C., Breguet, J. M., Michler, J., Schulz, D., & Giovanola, J. H. (2013). Nanoindentation cracking in gallium arsenide: Part I. in situ SEM nanoindentation. *Journal of Materials Research*, *28*(20), 2785–2798. https://doi.org/10.1557/jmr.2013.252

Westergaard, H. M. (1939). Bearing pressures and cracks. *Journal of Applied Mechanics*, Vol. 61, pp. A49–A53. https://doi.org//publication/216756690

Whittaker, E. J. W. (1981). Electron Diffraction in the Electron Microscope. In J. W. Edington (Ed.), *Crystallography* (pp. 217–224). https://doi.org/10.1016/b978-0-08-023804-3.50022-5

Williams, M. L. (1961). On the Stress Distribution at the Base of a Stationary Crack. *Journal of Applied Mechanics*, *28*(1), 78. https://doi.org/10.1115/1.3640470

Willis, J. R. (1975). Equations of motion for propagating cracks. *The Mechanics and Physics of Fracture*, 57–67.

Wolff, G. A., & Broder, J. D. (1959). Microcleavage, bonding character and surface structure in materials with tetrahedral coordination. *Acta Crystallographica*, *12*(4), 313–323. https://doi.org/10.1107/s0365110x59000949

Wu, K. (1989). On the crack-tip fields of a dynamically propagating crack in an anisotropic elastic solid. *International Journal of Fracture*, *41*(4), 253–266. https://doi.org/10.1007/BF00018857

Wu, K. (2000). *Dynamic crack growth in anisotropic material*. 1–12. https://doi.org/10.1023/A:1007621500585

Xu, L., Kong, L., Zhao, H., Wang, S., Liu, S., & Qian, L. (2019). Mechanical behavior of undoped n-type GaAs under the indentation of berkovich and flat-tip indenters. *Materials*, *12*(7), 1192. https://doi.org/10.3390/ma12071192

Yasutake, K., Konishi, Y., Adachi, K., Yoshii, K., Umeno, M., & Kawabe, H. (1988). Fracture of GaAs Wafers. *Japanese Journal of Applied Physics*, *27*(12R), 2238–2246.

Yoffe, E. H. (1951). The moving griffith crack. *The London, Edinburgh, and Dublin Philosophical Magazine and Journal of Science*, *42*(330), 739–750. https://doi.org/10.1080/14786445108561302

Zapffe, C. A., & Worden, C. O. (1949a). Fractographic study of an ammonium dihydrogen phosphate single crystal. *Acta Crystallographica*, *2*(6), 383–385. https://doi.org/10.1107/S0365110X49000990

Zapffe, C. A., & Worden, C. O. (1949b). Fractography as a technique in crystal chemistry. *Acta Crystallographica*, *2*(6), 377–382. https://doi.org/10.1107/S0365110X49000989

Zapffe, C. A., & Worden, C. O. (1949c). Further fractographic studies of synthetic single crystals. *Acta Crystallographica*, *2*(6), 386–388. https://doi.org/10.1107/S0365110X49001004

Zhang, P., Li, S. X., & Zhang, Z. F. (2011). General relationship between strength and hardness. *Materials Science and Engineering A*, *529*(1), 62–73. https://doi.org/10.1016/j.msea.2011.08.061